

Laser Treatment of Silicon Thin-Films for Photovoltaic Applications

Claudia Maurer

Energie & Umwelt / Energy & Environment

Band / Volume 432

ISBN 978-3-95806-347-1

Forschungszentrum Jülich GmbH
Institut für Energie- und Klimaforschung
IEK-5 Photovoltaik

Laser Treatment of Silicon Thin-Films for Photovoltaic Applications

Claudia Maurer

Schriften des Forschungszentrums Jülich
Reihe Energie & Umwelt / Energy & Environment

Band / Volume 432

ISSN 1866-1793

ISBN 978-3-95806-347-1

Bibliografische Information der Deutschen Nationalbibliothek.
Die Deutsche Nationalbibliothek verzeichnet diese Publikation in der
Deutschen Nationalbibliografie; detaillierte Bibliografische Daten
sind im Internet über <http://dnb.d-nb.de> abrufbar.

Herausgeber
und Vertrieb: Forschungszentrum Jülich GmbH
 Zentralbibliothek, Verlag
 52425 Jülich
 Tel.: +49 2461 61-5368
 Fax: +49 2461 61-6103
 zb-publikation@fz-juelich.de
 www.fz-juelich.de/zb

Umschlaggestaltung: Grafische Medien, Forschungszentrum Jülich GmbH

Druck: Grafische Medien, Forschungszentrum Jülich GmbH

Copyright: Forschungszentrum Jülich 2018

Schriften des Forschungszentrums Jülich
Reihe Energie & Umwelt / Energy & Environment, Band / Volume 432

D 82 (Diss., RWTH Aachen University, 2018)

ISSN 1866-1793
ISBN 978-3-95806-347-1

Vollständig frei verfügbar über das Publikationsportal des Forschungszentrums Jülich (JuSER)
unter www.fz-juelich.de/zb/openaccess.



This is an Open Access publication distributed under the terms of the [Creative Commons Attribution License 4.0](https://creativecommons.org/licenses/by/4.0/), which permits unrestricted use, distribution, and reproduction in any medium, provided the original work is properly cited.

Abstract

Thin-film silicon is an important material in the fields of photovoltaics. As well as microcrystalline ($\mu\text{-Si:H}$), amorphous (a-Si:H) silicon has been used for a long as an absorber in thin-film solar cells. Moreover, the surface passivation of c-Si wafers for heterojunction solar cells is achieved with a-Si:H . In addition, a-Si:H is used as precursor for tunnel oxide passivated contacts. Here, a post-deposition thermal treatment of the a-Si:H layer is mandatory. In doing so, the amorphous silicon develops crystalline phases. This annealing step is conducted at high temperatures, risking damage to the tunnel oxide. As a consequence, there is the idea of replacing amorphous silicon with microcrystalline silicon.

In this work, the influence of a laser treatment on the structural, electrical and optical properties of a-Si:H and $\mu\text{-Si:H}$ was investigated. The diffusion of hydrogen for a-Si:H on glass substrates is thus of special interest. Firstly, the eligibility of Raman spectroscopy to evaluate the influence of a laser treatment on the hydrogen concentration and the microstructure was studied. Therefore, a-Si:H was deposited on infrared transparent substrates. After deposition, the samples were annealed at different temperatures in a furnace. These samples were also analyzed with Fourier Transform Infrared Spectroscopy, a well-established method, in addition to Raman spectroscopy. The comparison of both analysis methods proved that Raman spectroscopy can be used to determine the relative change of the hydrogen concentration of amorphous silicon. In addition, the qualitative evolution of the microstructure parameter is competitive. As a result, Raman spectroscopy can be used to evaluate the influence of a Laser treatment on the hydrogen concentration and the microstructure parameter of amorphous silicon.

For the laser treatment of a-Si:H a short-pulse laser with a wavelength of 532 nm and a rectangular beam profile was used. For these experiments, both the treatment time and the Laser power were varied. In order to compare the results obtained with different treatment parameters, the temperature evolution during the laser treatment was recorded. As the impact of the temperature has more impact on the diffusion than the time, the maximum process temperature was used to compare the results. Due to the Laser treatment, a decrease of the hydrogen concentration was already observed for process times as short as 3 s and a maximum process temperature as low as 214 °C. Within the experiments of this study, the hydrogen concentration was reduced below the detection threshold of

Raman spectroscopy. In addition, Finite Element simulations were conducted to determine the hydrogen concentration. The simulation results show that the intense irradiation of the laser treatment promotes the hydrogen diffusion, while the hydrogen concentration can be reduced at low temperatures and short treatment times. The analysis of the photo- and dark conductivity revealed that the hydrogen concentration can be reduced over a large parameter range without negative impact on the electrical properties. However, the absorption edge is shifted to lower energies due to the reduced hydrogen concentration. An increase of the sub-bandgap absorption at 1.2 eV and with it an increase of deep defects was not observed for temperatures smaller than $T \geq 603$ °C.

The influence of a laser treatment on p-type $\mu\text{-Si:H}$ was investigated in further experiments. Here, the same laser source as for the previous experiments was used. However, the treatment was different than before, as the treated surface was scanned with a line shaped laser beam. First the influence on the resistivity, the hall mobility and the carrier concentration for p-type $\mu\text{-Si:H}$ on glass substrates were studied. Due to the laser treatment, the resistivity was decreased by a factor of 20, while the hall mobility was increased by a factor of 6.1 and the carrier density by a factor of 3.2. A high doping concentration is of importance for selective field-effect passivated contacts. The higher the doping concentration the higher is the resulting electrical field, while the selectivity of the contacts is improved. In addition, a high conductivity is favorable in order to reduce parasitic resistance. The laser process that was established for p-type $\mu\text{-Si:H}$ on glass substrates was transferred to tunnel oxide passivated c-Si wafers. For the latter, the focus of the laser treatment is on the passivation quality and the sheet resistance. The minority carrier lifetime was doubled due to the laser treatment, while, at the same time, the sheet resistance could be decreased. As a result of the experiments of glass substrates, the reduction of the sheet resistance implies the de-passivation of dopands and with it, an improved field-effect passivation. These Laser processes were compared to a furnace treatment. The comparison revealed that the highest lifetime was obtained for both methods at a similar process temperature. However, the lifetime was increased by 34 % for furnace annealing while the lifetime of the laser treated samples showed an increase greater than 100 %.

Kurzfassung

Dünnschicht Silizium ist ein bedeutendes Material in der Photovoltaik. Sowohl amorphes (a-Si:H) als auch mikrokristallines ($\mu\text{c-Si:H}$) Silizium werden seit langem als Absorber in Dünnschicht Solarzellen verwendet. Darüber hinaus wird die Oberflächenpassivierung von Heteroübergangs Solarzellen mit a-Si:H erzielt. Des Weiteren findet a-Si:H Anwendung für Tunneloxid passivierte Kontakte. Dafür ist eine thermische Nachbehandlung des a-Si:H notwendig, wodurch kristalline Anteile im Material entstehen. Dieser Tempersschritt wird bei hohen Temperaturen durchgeführt, wodurch Schäden im Tunneloxid entstehen können. Folglich gibt es Überlegungen, amorphes Silizium durch mikrokristallines zu ersetzen.

In der vorliegenden Arbeit wurden die Auswirkungen von Laser Behandlungen auf strukturelle, elektrische und optische Eigenschaften von a-Si:H und $\mu\text{c-Si:H}$ untersucht. Ein besonderer Fokus liegt dabei auf der Wasserstoffdiffusion in a-Si:H auf Glassubstraten. Um den Einfluss der Laserbehandlung auf den Wasserstoffgehalt und die Mikrostruktur bewerten zu können, wurde zunächst Raman Spektroskopie in Hinblick auf die Eignung als Analysemethode evaluiert. Dafür wurden a-Si:H Schichten auf infrarot transparenten Substraten deponiert und bei unterschiedlichen Temperaturen im Ofen getempert. Diese Proben wurden sowohl mit Fourier Transformierter Infrarot Spektroskopie, einer etablierten Methode, als auch mit Raman Spektroskopie analysiert. Der Vergleich der Messergebnisse zeigt, dass Raman Spektroskopie geeignet ist, um die relative Änderung des Wasserstoffgehalts in a-Si:H zu bestimmen. Darüber hinaus ist der qualitative Verlauf des Mikrostrukturparameters beider Methoden vergleichbar. Folglich kann der Einfluss einer Laserbehandlung auf den Wasserstoffgehalt und den Mikrostrukturparameter mittels Raman Spektroskopie substratunabhängig analysiert werden.

Zur Laserbehandlung von a-Si:H wurde ein Kurzpuls laser mit einem rechteckigen Strahlprofil und einer Wellenlänge von 532 nm verwendet. Sowohl die Behandlungsdauer als auch die Laserleistung wurden bei diesen Experimenten variiert. Zur Vergleichbarkeit der Behandlung mit verschiedenen Parametern wurde die Temperaturentwicklung während der Laserbehandlung aufgezeichnet. Da der Einfluss der Temperatur auf die Diffusion größer ist als der Einfluss der Zeit, wurde die maximale Temperatur verwendet, um die Ergebnisse zu vergleichen. Durch die Laserbehandlung wurde der Wasserstoffgehalt bereits bei einer Behandlungs-

dauer von 3 s und einer maximalen Prozesstemperatur von 214 °C reduziert. Im Rahmen der Experimente wurde der Wasserstoffgehalt unter die Nachweisgrenze des Raman Spektrometers reduziert. Zusätzlich wurden Finite Element Simulationen zur Bestimmung des Wasserstoffgehalts durchgeführt. Die Simulationsergebnisse zeigen, dass die intensive Bestrahlung durch den Laser die Diffusion verstärkt, wodurch der Wasserstoffgehalt bei niedrigen Temperaturen und kurzen Behandlungszeiten reduziert wird. Die Untersuchung der elektrischen Eigenschaften ergibt, dass der Wasserstoffgehalt mit dieser Laserbehandlung über einen weiten Bereich reduziert werden kann, ohne die Hell- und Dunkelleitfähigkeit zu beeinflussen. Aufgrund des reduzierten Wasserstoffgehalts verschiebt sich die Absorptionskante für maximale Prozesstemperaturen $T \geq 522$ °C zur niedrigeren Energie hin. Ein Anstieg der Absorption bei 1.2 eV und damit ein Anstieg der Defekte tief in der Mobilitätsücke wird erst ab $T \geq 603$ °C beobachtet.

In weiteren Experimenten wurde der Einfluss einer Laserbehandlung auf p-Typ $\mu\text{c-Si:H}$ untersucht. Hierfür wurde die gleiche Laserquelle verwendet wie für die Behandlung von a-Si:H. Die Behandlung unterscheidet sich insofern, dass die behandelte $\mu\text{c-Si:H}$ Fläche mit einem linienförmigen Strahlprofil gescannt wurde. Zunächst wurde der Einfluss auf den spezifischen Widerstand, die Hall Mobilität und die Ladungsträgerdichte auf Glassubstraten untersucht. Der spezifische Widerstand wurde dabei um den Faktor 20 reduziert, während die Hall Mobilität und den Faktor 6.1 und die Ladungsträgerdichte um den Faktor 3.2 erhöht wurden.

Eine hohe Dotierstoffkonzentration ist bei selektiven passivierten Feld-Effekt Kontakten besonders wichtig. Je höher die Dotierstoffkonzentration ist, desto größer wird das elektrische Feld, wodurch sich die Selektivität der Kontakte verbessert. Zudem ist eine hohe Leitfähigkeit wünschenswert, um parasitäre Widerstände zu reduzieren. Der für p-Typ $\mu\text{c-Si:H}$ auf Glassubstraten erarbeitete Laserprozess wurde auf Siliziumwafer mit Tunneloxid Passivierung übertragen. An dieser Stelle liegt der Fokus auf dem Einfluss der Laserbehandlung auf die Qualität der Passivierung und den Schichtwiderstand. Die Ladungsträgerlebensdauer wurde durch die Laserbehandlung verdoppelt, während gleichzeitig der Schichtwiderstand reduziert wurde. Die Reduktion des Schichtwiderstandes lässt als Folge der Versuche auf Glassubstraten auf eine Depassivierung der Dotierstoffe und somit eine bessere Feldeffekt Passivierung schließen. Die Laserprozesse wurden mit Temperprozessen im Ofen verglichen. Dabei zeigt sich, dass die höchste Lebensdauer für beide Methoden bei einer vergleichbaren Prozesstemperatur liegt. Hierbei ist zu beachten, dass die Lebensdauer bei den Ofenprozessen nur um 34 % erhöht wurde, während der Laserprozess zu einer Verbesserung von mehr als 100 % erreicht.

Contents

| | | |
|----------|---|-----------|
| 1 | Introduction | 1 |
| 1 | Fundamentals and Basics | 5 |
| 2 | Fundamentals | 7 |
| 2.1 | Thin-Film Silicon | 7 |
| 2.1.1 | Amorphous Silicon | 7 |
| 2.1.2 | Microcrystalline Silicon | 14 |
| 2.2 | Solar Cells | 18 |
| 2.2.1 | Laser Processes in Solar Cell Fabrication | 22 |
| 2.3 | Finite Element Method Simulations | 23 |
| 2.3.1 | Heat Transfer Model | 25 |
| 2.3.2 | Diffusion Model | 27 |
| 3 | Characterization Methods | 29 |
| 3.1 | Thin-Film Layer Thickness | 29 |
| 3.2 | Electrical Characterization | 30 |
| 3.2.1 | Photo- and Dark Conductivity Measurements | 30 |
| 3.2.2 | Sheet Resistance Measurements | 31 |
| 3.2.3 | Determination of Hall Mobility and Carrier Density | 32 |
| 3.3 | Spectroscopy | 38 |
| 3.3.1 | Raman Spectroscopy | 38 |
| 3.3.2 | Fourier Transform Infrared (FTIR) Spectroscopy | 40 |
| 3.3.3 | Reflectance, Transmittance and Absorptance | 41 |
| 3.3.4 | Photothermal Deflection Spectroscopy (PDS) | 42 |
| 3.4 | Photoluminescence (PL) | 42 |
| 3.5 | Secondary Ion Mass Spectrometry (SIMS) | 46 |
| 4 | Laser Sources | 49 |
| 4.1 | 532 nm (vis) Short Pulse Laser Source | 49 |
| 4.1.1 | Setup for the Laser Treatment of a-Si:H | 50 |
| 4.1.2 | Setup for the Laser Treatment of $\mu\text{c-Si:H}$ | 53 |
| 4.2 | 355 nm (uv) Short Pulse Laser Source | 55 |

| | | |
|-----------|--|------------|
| II | Results and Discussions | 57 |
| 5 | Temperature Measurements | 59 |
| 5.1 | Pyrometers | 59 |
| 5.1.1 | Calibration Setup | 59 |
| 5.2 | Pyrometer Temperature Correction for a-Si:H | 61 |
| 5.3 | Pyrometer Temperature Correction for $\mu\text{c-Si:H}$ | 63 |
| 6 | Development of a Method for the Structural Characterization of a-Si:H | 65 |
| 6.1 | Analysis of a-Si:H using Raman Spectroscopy | 65 |
| 6.2 | Raman Spectra and Fitting | 67 |
| 6.3 | Sample Fabrication and Measurement | 72 |
| 6.3.1 | Sample Fabrication | 72 |
| 6.3.2 | FTIR Reference Measurements | 72 |
| 6.3.3 | Raman Signal Analysis | 72 |
| 6.3.4 | Depth-Dependent Hydrogen Concentration | 75 |
| 6.3.5 | Depth-Dependent Microstructure Parameter | 79 |
| 6.4 | Conclusion | 80 |
| 7 | Laser Treatment of Amorphous Silicon on Glass Substrates | 83 |
| 7.1 | Experiments | 83 |
| 7.1.1 | Sample Fabrication | 83 |
| 7.1.2 | Laser Treatment | 84 |
| 7.2 | Experimental Results and 2D Heat Transfer Simulation | 85 |
| 7.2.1 | Time Dependent Process Temperature | 85 |
| 7.2.2 | Hydrogen Concentration | 86 |
| 7.2.3 | Electrical and Optical Properties | 87 |
| 7.2.4 | 2D FEM Heat Transfer Simulation | 89 |
| 7.3 | Simulations | 92 |
| 7.3.1 | 1D Laser Pulse Dependent Temperature Evolution | 93 |
| 7.3.2 | 1D FEM Hydrogen Diffusion Simulations | 95 |
| 7.4 | Discussion | 98 |
| 8 | Laser Treatment of Microcrystalline Silicon | 103 |
| 8.1 | p-type $\mu\text{c-Si:H}$ on Glass Substrates | 103 |
| 8.1.1 | Sample Fabrication | 103 |
| 8.1.2 | Laser Treatment of p-type $\mu\text{c-Si:H}$ at 532 nm with a Line Shaped Laser Beam | 107 |
| 8.1.3 | Laser Treatment of p-type $\mu\text{c-Si:H}$ with 355 nm with a Gaussian Beam Shape | 114 |

| | | |
|----------|--|------------|
| 8.1.4 | Discussion | 119 |
| 8.2 | p-type $\mu\text{-Si:H}$ on c-Si Substrates | 121 |
| 8.2.1 | Experiments | 121 |
| 8.2.2 | Laser Treatment of Symmetrical p-type $\mu\text{-Si:H}$ on c-Si Substrates | 126 |
| 8.2.3 | Discussion | 136 |
| 9 | Conclusion and Outlook | 139 |
| A | Appendix | 143 |
| | Bibliography | 145 |
| | List of Symbols | 160 |
| | List of Abbreviations | 163 |
| | Acknowledgment | 164 |

1 Introduction

The strategy of modernization of the energy supply in Germany is known as "Energiewende" [1]. It is the result of the revision of the law for the promotion of electricity generation from renewable energy sources [2] and the withdrawal from the nuclear energy program which was decided in 2011 as a result of the nuclear accident in Fukushima. Within the "Energiewende" the quota of renewable energy is to be increased to a minimum of 80 % by 2050 [2].

Indeed, ForschungsVerbund Erneuerbare Energien (FVEE) found that an overall power supply of 100 % sustainable energy is feasible by 2050 [3]. Here, a study of Deutsches Luft und Raumfahrtzentrum (DLR) demonstrated that the technical potential of solar energy is extremely high [4]. Within the study of FVEE it was stated that Si wafer-based solar cells and thin-film solar cells, as well as concentrating solar cells are necessary to cover the energy demand [3].

Solar power has numerous advantages, cost efficiency amongst others. The cost of solar power decreased in Germany from 2005 to 2014 from 40 ct/kWh to 9 ct/kWh for large scale photovoltaic installations [5]. Lower prices are possible in sunnier regions. For example, a winning bid below 1.8 ct/kWh has been reported in Saudi Arabia [6].

The costs for photovoltaic modules and power inverters has decreased by a factor of 10 within the year 1980 to 2010, a trend that is believed will continue [3]. Indeed, the International Energy Agency expects the cost of solar power to decrease by another 40 % to 70 % until 2040 [1].

Recently, Bundesministerium für Wirtschaft und Energie (BMWi) published a study concerning the German "Energiewende", the status and the needs [1]. In this study it was stated that solar cells have a high technical potential in Central Europe. However, it is not yet clear which solar cell technology is the most promising in the long term. Both wafer based and thin-film solar cells as well as new concepts, for example organic solar cells and nanotechnology, are of interest [3]. In this work experiments were performed that are of interest for both thin-film solar cells and wafer based solar cells.

One type of thin-film solar cells is based on silicon thin-films. These silicon thin-films can either be amorphous (a-Si) or microcrystalline (μ c-Si). Due to the high defect density of these silicon thin-films, hydrogen is added for the passivation of these defects. Without this hydrogen passivation, thin-film silicon cannot be

used for solar cells. For device grade a-Si:H, for example 10 to 20 at.% hydrogen is incorporated. Moreover, a-Si:H is used as passivation in heterojunction solar cells and as precursor for selective contacts [7, 8]. The use of carrier selective contacts is assumed to be the only choice for achieving the theoretical efficiency limit of 29.4 % for crystalline silicon solar cells [9, 10].

Post deposition thermal treatment is often of importance for these applications. This thermal treatment is in general performed in a furnace. Silicon heterojunction solar cells benefit most from a thermal treatment at low temperatures, such as $T = 200$ °C, for a long time up to 24h [7,8]. High temperature annealing at temperatures up to 900 °C of amorphous silicon is used for solid phase crystallization of a-Si:H layers [10–14] for solar cells with carrier selective contacts.

In this work, a short-time post deposition thermal treatment is investigated. Here, the temperature increase is realized by the absorption of short-pulse laser sources. Short-time annealing is not feasible on the same time scale with a furnace as it is for laser treatment. By using short-term processes, production costs can be reduced. In addition it is investigated, whether the material properties can be improved compared to furnace processes. The extent to which a short-term thermal treatment affects the material compared to annealing processes in a furnace is analyzed.

Part of the work was financed by BMU (project no. 0325446B). The present work is organized as follows. Chapters 2-4 summarize the current foundation of knowledge and introduces and explain the methods of measurement as well as the laser sources used in the work. Chapters 5-7 present both, the analytical method developed in this thesis and the experimental results.

Chapter 2 comprises the fundamentals of thin-film silicon. In particular, the structural, electrical, and optical properties of amorphous and microcrystalline silicon are presented. In addition, solar cell concepts that use amorphous or microcrystalline silicon are shown. Furthermore, laser concepts that are already used for solar cell fabrication are introduced. Lastly, a short introduction into finite element simulations and the application for heat transfer and diffusion simulations is given.

Chapter 3 provides information about the characterization methods used for this thesis. The methods for determining the temperature and the layer thickness, as well as the different methods for electrical, optical and structural characterization are presented in this chapter.

Chapter 4 describes the laser sources used for the laser treatment in this work. The characteristics of the laser source as well as the setup for the individual ap-

plication are illustrated.

Chapter 5 outlines the temperature measurement with the pyrometers used in this work. In addition, the material-dependent calibration of the pyrometers is presented.

Chapter 6 presents a method to determine the hydrogen concentration and the microstructure of a-Si:H on glass. Raman spectroscopy is evaluated as alternative to Fourier Transform Infrared Spectroscopy (FTIR). Samples on infrared transparent substrates are characterized with both FTIR and Raman spectroscopy. In addition secondary mass ion spectroscopy (SIMS) is performed on the same samples to gain insight into the depth-dependent hydrogen distribution. The results of both optical methods are compared and related to the SIMS results.

Chapter 7 examines the possibility of using a short-term laser treatment instead of an furnace-based post deposition thermal treatment. The effect of a laser treatment on a-Si:H is investigated. Thereby, the influence on structural, electrical and optical properties is studied. A special focus is here on the influence of the laser treatment on the hydrogen concentration. For a better understanding of the experimental results, FEM heat transfer and diffusion simulations are performed. In addition, the influence of high irradiation during the laser treatment is taken into account.

Chapter 8 contains the analysis of the impact of laser treatment on p-type $\mu\text{-Si:H}$. This chapter is build up of two distinct sections. In Section 8.1, experiments were performed on glass substrates, to choose a suitable laser source based on the influence on electrical properties. In doing so, a detailed analysis of the influence of laser treatment on the the resistivity, the Hall mobility and the carrier density of p-type $\mu\text{-Si:H}$ is presented. Based on these results, the process was transferred to c-Si wafers with the prospect of generating a system apt for passivated contacts (Section 8.2). The influence on the sheet resistance and the passivation quality of the laser process is investigated in this section.

Chapter 9 summarizes the conclusions drawn in the individual experimental chapters.

Part I

Fundamentals and Basics

2 Fundamentals

In this work laser treatments were applied to silicon thin-films. Materials that are of interest for this thesis are introduced in this chapter. In Section 2.1, the structural, electrical and optical properties of amorphous and microcrystalline silicon will be described.

Section 2.2 introduces solar cell types that are of interest for this work. In addition, laser processes that are already used in solar cell production are presented.

The last section of this chapter (Sec. 2.3) is dedicated to simulations. Here, finite element simulations, in addition to the simulation models used in this work, are described.

2.1 Thin-Film Silicon

Thin-film silicon, as used in this work, is deposited from the gas phase of plasma enhanced chemical vapor deposition (PECVD). Detailed information about the deposition techniques can be found in [15,16]. Both, amorphous and microcrystalline silicon are used for thin-film solar cells as absorber. In addition, a-Si:H is used for wafer passivation of silicon heterojunction (SHJ) solar cells as well as contact layer for field effect passivated solar cells.

In this section, structural, electrical and optical properties of hydrogenated amorphous silicon (a-Si:H) as well as microcrystalline silicon ($\mu\text{c-Si:H}$) are presented. In addition, the influence of annealing on the material properties is described. A complete description about the structural, electrical and optical properties is presented in [17–21].

2.1.1 Amorphous Silicon

Applications of a-Si Amorphous silicon (a-Si:H) has a long tradition in solar cell and thin film transistor fabrication [19, 22, 23]. The efficiency of solar cells based on amorphous silicon had been steadily improving until the end of the 1990's. Amorphous silicon is widely used in thin-film solar cells as absorber material [16, 17, 21, 24–26]. Furthermore, a-Si:H is used as passivation for heterojunction solar cells [7, 27–31, 31–33] and for passivated contacts [10–13, 34]. Apart from solar cells, a-Si:H is also used for thin-film transistors [23, 35–38].

Due to the possibility of low-temperature deposition, PECVD a-Si:H is well suited for low temperature processes [39]. In addition to classical thin-film solar cells, amorphous silicon is used as absorber layer in tandem solar cells for photoelectrochemical water-splitting [40–42]. Moreover, a-Si:H can be used as precursor for crystalline thin-film solar cells on glass [43–48].

Structural Properties Figure 2.1 a) shows a simplified 2D illustration of the crystalline silicon network. All bonding angles and distances are uniform. The bandgap of crystalline semiconductor materials is the result of this periodicity, the long range order (LRO).

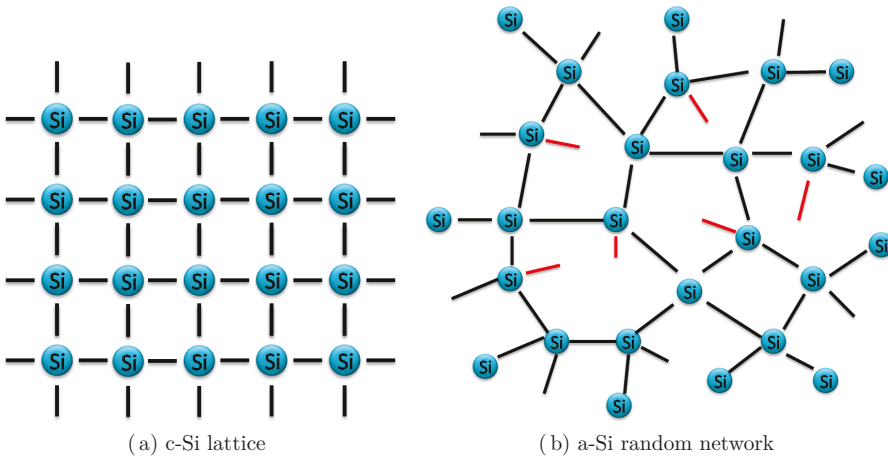


Figure 2.1: (a) shows a simplified 2D sketch of c-Si, while (b) holds the random network of a-Si. Blue circles refer to silicon (Si) atoms and the red lines indicate broken bonds (dangling bonds), respectively.

In contrast to crystalline solids, amorphous materials exhibit no LRO. This lack of any periodical structure or statistical definition of order characterizes amorphous material. Figure 2.1 b) presents a simplified 2D sketch of the random network of amorphous silicon. The complete loss of structure over few atomic distances leads to a continuous random network. As a result of the lack of any periodical order, amorphous materials have no bandgap in the classical sense. Even though the bonding angles as well as the bonding lengths deviate from crystalline material, neighboring atoms do have an order to each other, similar to crystalline solids. This is referred to as short range order (SRO). Consequently,

amorphous Silicon (a-Si) possesses similarities to crystalline silicon (c-Si) in the atomic configuration on an atomic scale. On this atomic scale, most Si atoms have four covalent bondings with four neighboring atoms. Based on the SRO, the band concepts of crystalline semiconductors can be applied to a-Si using an approximate demarcation line between the localized and extended states to define the mobility gap [49]. This will be explained in detail in the paragraph electrical properties.

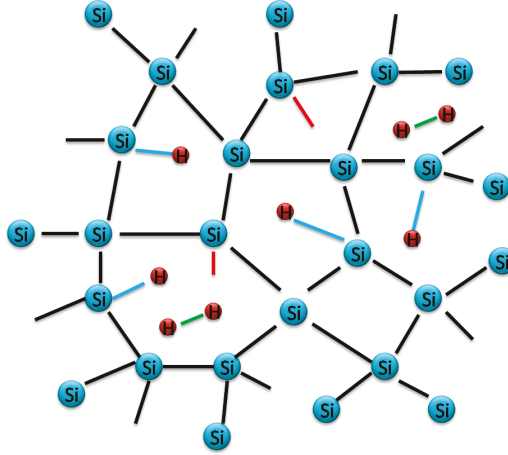


Figure 2.2: Simplified 2D sketch of the structure of intrinsic a-Si:H. Blue circles refer to silicon (Si) atoms and red circles to hydrogen (H), respectively. The red lines indicate broken bonds (dangling bonds), blue lines indicate the covalent bonds of passivated dangling bonds and green lines highlight the bondings of H₂ molecules.

Large bonding distances and strong deviations from the bonding angles of c-Si result in weak bonds. These weak bonds are easily broken with sufficient energy (e.g. heat, light), forming dangling bonds (db). The db are highlighted in red in Figure 2.1 b). As a consequence of the db, silicon atoms do no longer necessarily exhibit a fourfold bonding, leading to defects. Pure a-Si contains 10^{19} cm^{-3} up to 10^{21} cm^{-3} defects. Considering a total density of Si atoms of $5 \times 10^{22} \text{ cm}^{-3}$, the density of db is too high for a functional device [20,50]. In order to passivate these dangling bonds, hydrogen is incorporated during the deposition process. Figure 2.2 shows a simplified 2D sketch of a-Si:H with dangling bonds (red lines), H₂ molecules (red) and passivated db (blue lines). Hydrogen forms covalent bonds with former silicon db. These passivated db are indicated with

blue covalent bonds in Figure 2.2. In doing so, the density of defects can be reduced to 10^{16} cm^{-3} to 10^{15} cm^{-3} . Passivated db do not act as recombination centers of carriers [17, 20].

Considering an average of 10^{20} cm^{-3} defects, 0.2 at.% hydrogen would be sufficient to passivate all dangling bonds. However, 10 % to 20 % of hydrogen incorporated in a-Si:H are needed to produce device grade material. Even though the amount of hydrogen is orders of magnitude higher than quantitatively necessary, in practice it is impossible to passivate all dangling bonds. The excess hydrogen can form H_2 molecules inside the random network (green indicated covalent bonding), or break up additional bonds. The structural properties of a-Si:H are analyzed with Fourier Transform InfraRed spectroscopy (FTIR). A detailed description of the structural properties determined with FTIR is found in Chapter 3, Section 3.3.2.

The density of defects is not constant in a-Si:H throughout the layer of the thin-film. The first few atomic layers that are grown on a substrate, as well as the surface where the atomic matrix comes to an end, have a higher density of defects. In addition, micro-voids act as internal surface and are assumed to have a larger amount of broken bonds. The density of micro-voids has a high influence on the light-induced degradation [17]. This light-induced degradation is referred to as Staebler-Wronski effect (SWE), the breaking of bonds due to irradiation. However, this effect is reversible by annealing [51].

Electrical Properties Amorphous silicon does not feature a bandgap like crystalline semiconductors. Nevertheless, the SRO leads to an effect similar to a bandgap as the valence requirements are satisfied for most atoms. Due to lack of the LRO, the crystalline directions for indirect minima in the band structure are undefined, leading to an effective direct mobility gap (bandgap) E_g for amorphous semiconductors and a higher absorption coefficient compared to the crystalline phase [17, 52]. The electronic structure of amorphous silicon is described by the density of states (DoS) as illustrated in Figure 2.3. In contrast to c-Si, the distribution of the DoS is continuous in a-Si:H due to the bandtails and the midgap states (=defect states) [15].

In general, the electronic states of amorphous semiconductors can be divided into three types (Fig. 2.3):

- conduction and valence band, extended states (red, highlighted blue)
- band tails (=localized states) (red)
- localized defect states in the center of the gap (light blue)

As mentioned above, the bands are similar to those of crystalline silicon. In a-Si:H the mobility edge E_V is situated in the valence band, while the same is

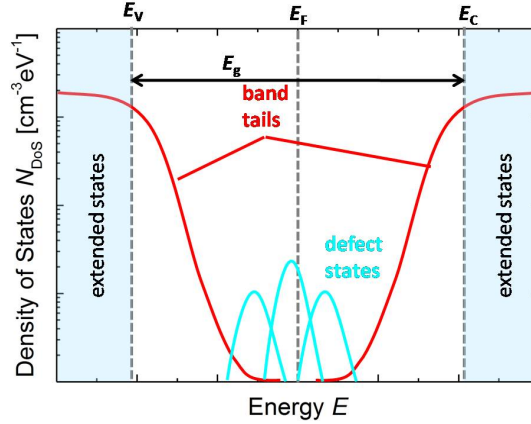


Figure 2.3: Schematic standard model of the electronic states of amorphous silicon as a result of the amorphous nature of the semiconductor on a logarithmic scale.

true for the mobility edge E_C of the conductivity band. The mobility edges are indicated with the vertical dashed lines in Figure 2.3. The extended states below E_V and above E_C are highlighted in blue. Figure 2.3 shows localized states between E_V and E_C in light blue [17, 21, 53]. These localized states have zero mobility associated with them. They are located in the middle of the bandgap and are referred to as midgap states. These midgap states are the result of deep defects, energy states that are caused by dangling bonds. Dangling bonds act as recombination center and limit the electronic quality of a-Si:H.

Typical values for the mobility gap of a-Si:H lie between $E_g(\text{aSi}) = 1.7$ eV and $E_g(\text{aSi}) = 1.8$ eV, while $E_g(\text{cSi}) = 1.1$ eV for c-Si. In addition, the mobility gap of a-Si:H can be influenced by the hydrogen concentration. Indeed, a low c_H leads to a high E_g , while a high c_H results in a low E_g , respectively.

The photoresponse is used to determine whether an a-Si:H (or $\mu\text{c-Si:H}$) thin-film is potentially good solar cell material. However, it is not sufficient as a qualifier on its own [17]; optical and structural properties have to be considered as well. The figure of merit of the photoresponse for potentially good solar cell absorber material is:

$$\frac{\sigma_{\text{photo}}}{\sigma_{\text{dark}}} > 10^5 \quad (2.1)$$

for a-Si:H, while σ_{photo} is the photoconductivity and σ_{dark} is the dark conductivity.

The dark conductivity is a measure for impurities. Even if the material inhibits only few impurities, or voluntary doping, the room temperature dark conductivity increases. The room temperature dark conductivity increases over one order of magnitude for each 50 meV that the Fermi level is shifted towards the conductivity band. Consequently, the higher the dark conductivity is, the more impurities (e.g. oxygen in a-Si:H) are present.

In short, material with $\sigma_{\text{photo}} = 10^{-5} \Omega\text{cm}$ and $\sigma_{\text{dark}} = 10^{-10} \Omega\text{cm}$, respectively is considered as device grade a-Si:H for absorbers in thin-film solar cells [17, 21].

Optical Properties Optical properties of a solid are in general characterized by the absorption coefficient α , the refractive index n and the optical gap E_g (onset of the absorption [49]). The efficiency of a solar cell is dependent on the fraction of absorbed sunlight. Consequently, the absorption edge and therewith E_g is of importance. Light with a photon energy E_{ph} below E_g is not absorbed.

Figure 2.4 shows the absorption coefficient of a-Si:H (black solid line). For comparison, the absorption coefficients of $\mu\text{c-Si:H}$ (blue dashed line) and c-Si (red dashed line) are added in the graph [54]. The spectrum is divided into three regions by dashed vertical lines. Region I refers to the sub-bandgap absorption with $E_g < 1.5 \text{ eV}$. Here, only transitions between extended states and defect states can occur. As α is dominated by defect absorption, the absorption coefficient in this region is linked to the defect density. Consequently, the sub-bandgap absorption can be used for the determination of the quantity of deep defects. For example, this is used for photothermal deflection spectroscopy as described in Chapter 3, Section 3.3.4. Region II refers to $\alpha \approx 1$ to 10^3 cm^{-1} and ranges from $1.5 \text{ eV} \leq E_{\text{ph}} \leq 1.9 \text{ eV}$. The exponential dependence of the absorption coefficient on the photon energy is characteristic for region II. This region, the Urbach edge, is strongly influenced by transitions between the valence band or the conduction band, respectively and tail states. Last, for photons with $E_{\text{ph}} > 1.9 \text{ eV}$, the transition takes place from the (extended) states of the valence and conduction bands (region III). In general, α is higher than 10^3 to 10^4 cm^{-1} in region III [24]. The absorption of a-Si:H is considerably smaller than for $\mu\text{c-Si:H}$ or c-Si in low photon energy regions. As a result, the long-wavelength region of the sunlight will not be absorbed by amorphous silicon, leading to a reduced efficiency.

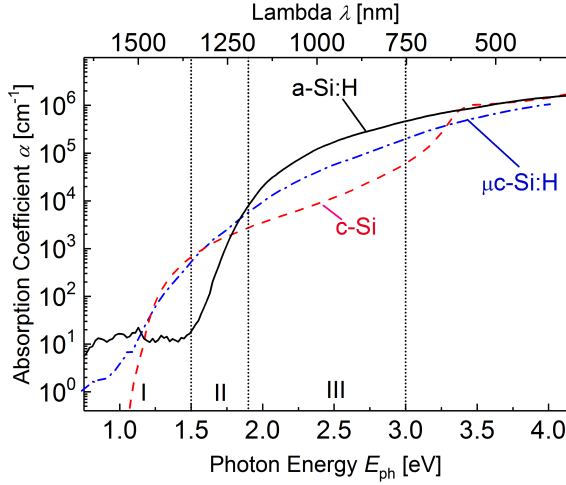


Figure 2.4: Absorption coefficient of a-Si:H (black solid line). For comparison, the absorption coefficients of μ c-Si:H (blue dashed line) and c-Si (red dashed line) are added to the graph (from [54]).

Staebler-Wronski Effect The Staebler-Wronski effect is the metastability of amorphous silicon, the light induced degradation. It was first analyzed in 1977 by Staebler and Wronski [51]. The exposure of a-Si:H to light results in an increase of the density of dangling bonds [55]. However, the metastability is reversible by thermal annealing. Weak strained and distorted bonds can be broken upon the influence of irradiation. Photon energies as low as $E_{ph} = 1.5$ eV can break weak Si-Si bonds. Please note, that the photon energy of sunlight is too low to break Si-H bonds which have a bonding energy of $E_{bond} = 3.5$ eV [56].

The type of hydrogen incorporation is related strongly to the metastability of a-Si:H. Hydrogen that is bonded at surfaces, including inner surfaces of voids, is related to an increased light-induced degradation [17]. The type of hydrogen incorporation can be detected with FTIR, for example. Hydrogen bonded at surfaces features a stretching mode at 2100 cm⁻¹, while hydrogen bonded in bulk exhibits a stretching mode at 2000 cm⁻¹, respectively. The relation of these modes, which form the microstructure parameter is therefore used as measure for the potentially light induced degradation of a-Si:H [57].

Annealing Thermal treatment, annealing, has a huge impact on the electrical, optical and structural properties of a-Si:H. First, the heat treatment decreases mechanical strain within the layer, resulting in a reordering process of the amor-

phous tissue. This reordering process results in the reduction of growth faults (e.g. voids), whereby the density of localized states within the mobility edge are reduced [58].

Annealing at temperatures up to $T = 400$ °C can lead to an improvement of the amorphous material. In contrast, annealing at more elevated temperatures between $T = 400$ °C and $T = 600$ °C has no positive impact on amorphous silicon considering the application as absorber layer in solar cells. In contrast, annealing at temperatures above $T > 600$ °C results in an increased conductivity and a shift of the mobility gap as a phase change process launches [58–60]. It has to be noted, that the crystallization of amorphous silicon underlies a time component [60].

Annealing can also lead to an outdiffusion of hydrogen, especially for annealing temperatures well above the deposition temperature and for long time annealing processes [61]. Voids of the size of divacancies or larger can form as a result of this outdiffusion. As mentioned before, void-rich or porous material tends to have a pronounced degradation behaviour [17]. In addition, Si-H bonds can be broken leading to additional dangling bonds. Therefore, the defect density can increase upon annealing [53, 62, 63]. It has been shown that for intrinsic a-Si:H, grown at device grade conditions, the number of voids increases considerably for annealing temperatures $T > 550$ °C. As a consequence, the microstructure parameter increases due to the increasing density of defects [17].

The effects of annealing on the defect density depends on various parameters such as the quality of the as-deposited a-Si:H and both the deposition and the annealing temperature. Annealing at the deposition substrate temperature has no significant influence on the density of states [64]. In contrast, annealing above the deposition temperature reduces the defect density, especially in case of deposition at low temperatures [65–68]. In addition, it has been found that the more defects are found in the as-deposited material, the higher is the influence of post-deposition annealing [69].

The structural changes in a-Si:H due to annealing influence the electrical properties. For example, the photoresponse increases due to annealing. Hereby, the impact is mainly on σ_{photo} that increases over more than two orders of magnitude, while σ_{dark} remains in the same order [65, 68, 70].

2.1.2 Microcrystalline Silicon

Application of $\mu\text{c-Si:H}$ Microcrystalline silicon is essentially used as the bottom cell of tandem solar cells (see Section 2.2). Microcrystalline silicon was first used for photovoltaic applications in 1990 at the Institute of Microtechnology of the University of Neuchâtel [20]. In order to produce $\mu\text{c-Si:H}$, the same deposition equipment as for a-Si:H can be used, even though the process parameters are completely different [20, 71].

Structural Properties Microcrystalline silicon consists of small crystalline silicon grains (nanocrystals) in an amorphous tissue with cracks and voids. In general, the crystals themselves have a size on a nanometer scale, though they can agglomerate to columnar structures in the range of micrometers [72, 73]. Figure 2.5 illustrates the schematic cross section of the microstructure of a $\mu\text{c-Si:H}$ film as a function of the crystalline volume fraction on a foreign substrate (e.g. glass). Here, the microstructure ranges from highly crystalline (left) to amorphous (right) [74].

Microcrystalline silicon can be divided in three states:

- isolated grains
- crystalline fibers/ percolation paths
- volume crystal material

The determination of the degree of crystallinity can be performed with Transmission Electron Microscopy, X-Ray diffraction, or Raman spectroscopy.

Raman spectroscopy is a quick and easy method to determine the crystalline volume fraction of $\mu\text{c-Si:H}$, therefore it is used in this work. The application of Raman spectroscopy to measure the Raman crystallinity X_C is described in Chapter 3, Section 3.3.1.

Regarding Figure 2.5, isolated grains are located on the right hand side, crystalline fibers build up in the center, while volume crystal material is shown on the left hand side. Disorder of latter exists only at grain boundaries.

The bandgap of $\mu\text{c-Si:H}$ ($E_g = 1.1$ eV) is in the same order as c-Si and therefore it is lower than in a-Si:H. Subsequently, the near infrared part of the sunlight is absorbed by $\mu\text{c-Si:H}$. On the contrary, the indirect bandgap of $\mu\text{c-Si:H}$ is a disadvantage concerning the use as absorber layer in a solar cell, as it leads to a lower absorption coefficient in the visible range. However, the reduced light induced degradation, compared to a-Si:H, is an obvious advantage of $\mu\text{c-Si:H}$. The structural properties of $\mu\text{c-Si:H}$ depend highly on the deposition parameters. For example, the crystallinity increases with decreasing silane concentration and the diameter of grains increases with increasing deposition time. A detailed description of the structure of microcrystalline silicon, its deposition and the influence on electrical and optical properties is in literature see, for example, [20, 21, 71, 74].

Dangling bonds can occur in amorphous regions, at grain boundaries, and also in crystalline regions of microcrystalline silicon. Though, for reasons of simplicity they are usually summarized to one defect density. Alike in a-Si:H, hydrogen

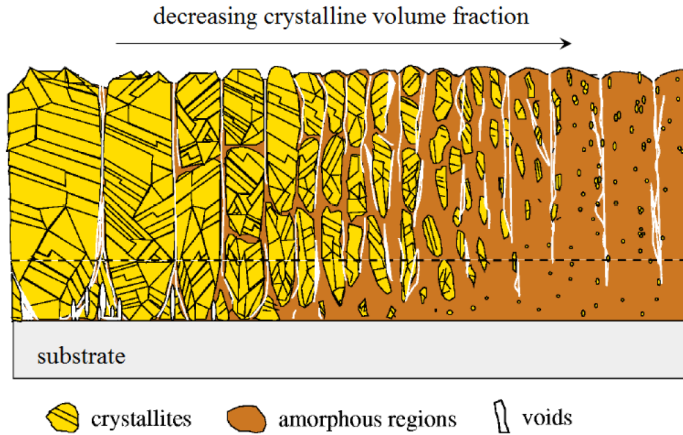


Figure 2.5: Schematic cross section model showing the microstructure of a $\mu\text{c-Si:H}$ film as a function of the crystalline volume fraction on a foreign substrate (e.g. glass). The microstructure ranges from highly crystalline (left) to amorphous (right). The picture is taken from [74].

passivates the dangling bonds in $\mu\text{c-Si:H}$. As the solubility of hydrogen in crystalline silicon is very low, the hydrogen passivation works primarily on the grain boundaries [75]. Considering the number of defects, $\mu\text{c-Si:H}$ that contains a large number of small crystallites can have almost no defects. Grain boundaries in $\mu\text{c-Si:H}$ can be regarded as normal grain boundaries of any crystalline silicon. The hydrogen concentration of $\mu\text{c-Si:H}$ strongly depends on the deposition temperature and correlates qualitatively with the defect density.

Columnar structures (see Fig. 2.5, left) are agglomerates of smaller crystalline regions, they should contain almost no hydrogen as most hydrogen is in the amorphous phase and can therefore be regarded as highly crystalline. However, these columns are separated by cracks and voids. As a consequence, the nature of the columnar structure limits the coplanar electrical transport. The cracks and voids of the columnar structures become more and more covered with amorphous tissue with decreasing crystallinity. Inside these columnar structures, twin boundaries are the dominating defect, while internal grain boundaries are assumed to contain only very few defects without significant impact. The ideal crystallinity for solar cells is between 60 % and 70 % [76].

Electrical Properties The conductivity of $\mu\text{c-Si:H}$ depends on the crystallinity. Both, σ_{photo} and σ_{dark} increase with increasing X_{c} . Though the increase is more pronounced for σ_{dark} than for σ_{photo} [54, 71]. This crystallinity dependent increase of σ_{dark} is believed to be the result of the increase of the density of free carriers due to the lower bandgap in the crystalline phase. The approximately linear correlation of σ_{dark} on the effective bandgap implies that the mobility of free carriers does not change significantly.

Similarly to for a-Si:H, the photoresponse can be used to qualify whether a $\mu\text{c-Si:H}$ thin-film is potentially good solar cell material, but it is not sufficient as a qualifier [17]. The figure of merit of the photoresponse for a potentially good microcrystalline solar cell absorber material is:

$$\frac{\sigma_{\text{photo}}}{\sigma_{\text{dark}}} > 10^2 \text{ to } 10^3 \quad (2.2)$$

Material with a photoconductivity of $\sigma_{\text{photo}} = 10^{-4} \text{ } \Omega\text{cm}$ for $\mu\text{c-Si:H}$ is considered as device grade material [17, 21]. The photoresponse of $\mu\text{c-Si:H}$ with $X_{\text{C}} = 0.6$ lies between 300 and 1000 [77]. It should be noted that $\mu\text{c-Si:H}$ layers show a strong dependence of the conductivity on the absorption of atmospheric gases and oxidation. As this is related to the porosity, especially highly crystalline layers are subject to atmospheric related degradation.

To sum up, the nature of electronic transport of $\mu\text{c-Si:H}$ lies between a-Si:H and c-Si. The influence of the charge carrier density is important due to the relationships between defects, Fermi level position and σ_{photo} . The amorphous tissue in-between the crystallites acts as matrix for defect passivation of the grain boundaries and as protective film against atmospheric triggered oxidation and degradation.

Optical Properties The optical properties of $\mu\text{c-Si:H}$ are a combination of the optical properties of a-Si:H and c-Si. Figure 2.4 shows α , depending on the photon energy. Hereby, region III is strongly influenced by the amorphous phase, as $\alpha_{\mu\text{c-Si}}$ is almost one order of magnitude higher than for $\alpha_{\text{c-Si}}$ for $3.0 \text{ eV} \geq E_{\text{ph}} > 1.8 \text{ eV}$. In contrast, the lower photon energy regions I+II ($E_{\text{ph}} < 1.8 \text{ eV}$) are dominated by the crystalline phase. The absorption in the sub-bandgap region is governed by the crystallinity. The sub-bandgap absorption increases with increasing X_{C} , where $X_{\text{C}} = 86 \%$ leads to an absorption similar to c-Si.

Doping of $\mu\text{c-Si:H}$ Microcrystalline silicon can be p- or n-type doped by adding gasses to the deposition process. For p-type $\mu\text{c-Si:H}$ B_2H_6 or $\text{B}(\text{CH}_3)_3$ (Trimethylboron, TMB) is added, while PH_3 is used for n-type, respectively. For this work, $\mu\text{c-Si:H}$ was doped with TMB. In case of low doping levels (10^{16} to 10^{17}) the

dopant atoms have to fill up defect states, while for higher doping levels the dopands and the carrier density are in a linear relationship to each other. The doping process in the crystalline phase of $\mu\text{c-Si:H}$ is similar to the process in c-Si , a substitution. As a consequence, high conductivities in the order of 10^2 S/cm can be obtained in $\mu\text{c-Si:H}$ [71]. The Hall mobility of p-type $\mu\text{c-Si:H}$ is in the order of $\mu_{\text{H}} = 0.1 \text{ cm/Vs}$ [78].

Of course, the degree of crystallinity has also an impact on the conductivity. Therefore, a high crystallinity is favorable for doped layers. However, deposition temperature and thickness influence the growth. It has been found that highly crystalline, thin, doped p-layers are difficult to process. Studies showed that the maximum conductivity is reached for a thickness of 20 nm and the maximum crystallinity is obtained for a deposition temperature around 180 °C [72, 78].

2.2 Solar Cells

Single crystal solar cells are highly efficient in performance, while thin-film solar cells have the advantage of being cost-efficient. Even though there are multiple kinds of thin-film solar cells, nowadays mainly CdTe, Cu(In,Ga)Se₂ (CIGS) and thin-film silicon is of importance [26]. Recently, organic-inorganic hybrid solar cells based on metal-halide perovskites are gaining importance. As the focus of this thesis is on the laser treatment of a-Si:H for thin-film solar cells and $\mu\text{c-Si:H}$ for solar cells with tunnel oxide passivated contacts (TOPCon), only these solar cell concepts will be introduced in the following.

Thin Film Silicon Solar Cells

Figure 2.6 illustrates the schematic setup for all thin-film technologies. The thin-film layers of solar cells are deposited on a substrate. In this connection, it is differed between the superstrate configuration (Fig.2.6, left) where the deposition substrate faces the irradiated side and the substrate configuration with the substrate at the bottom of the solar cell (Fig.2.6, right).

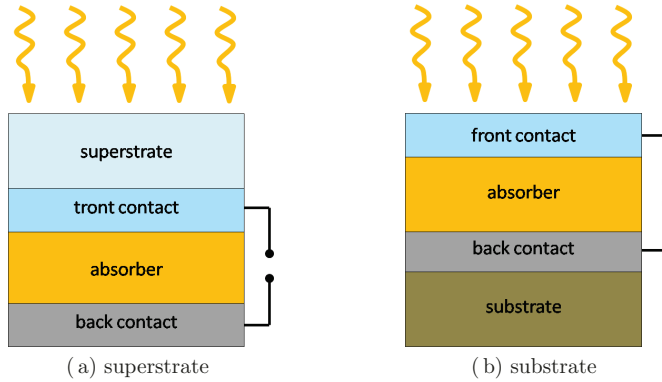


Figure 2.6: a) Basic scheme of the layer sequence for all thin-film technologies in superstrate and b) substrate configuration. The yellow curved arrows indicate the irradiation.

a-Si:H Solar Cells The diffusion length in a-Si:H is far too low for a pn-junction, therefore the pin configuration based on an external electrical field is used. Figure 2.7 a) shows a typical layer stack of a pin solar cell. Solar light passes the substrate and the transparent conductive oxide (TCO), the front contact, and is then absorbed mainly in the i-layer. The intrinsic absorber layer (i-layer) is between p and n doped layers. The doped layers generate a built-in-voltage U_{bi} , whereby an electrical field establishes in the i-layer. As a result of the electrical field, the photogenerated electrons and holes drift to the p and n layer, where they are transferred to the contacts and extracted. The thickness of the doped layers is considerably smaller than the i-layer $d_{p,n} \ll d_{absorber}$ to reduce the parasitic absorption in these layers as the carrier lifetime in doped a-Si:H layers is very short [26]. The charge carriers cannot reach the contacts if the doped layer are too thick as they would recombine within the doped layer.

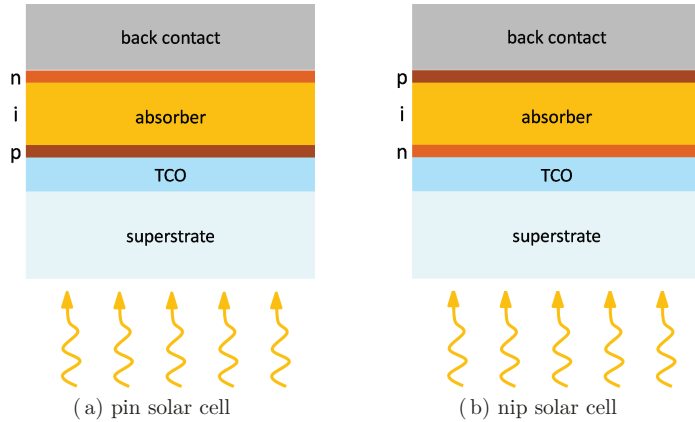


Figure 2.7: Scheme of a-Si:H solar cells. The p, i, and n-layers are made of thin-film silicon. The back contact is a metal and the front contact a TCO. All layers are deposited on a glass substrate. The yellow curved arrows indicate the irradiation with sunlight. a) shows the pin, while b) shows the nip configuration, respectively.

Multijunction Thin-Film Solar Cells As mentioned in Section 2.1.1, amorphous silicon has an onset of the absorption at approximately 1.8 eV which leads to significant transmission losses in a single junction solar cell. In contrast, microcrystalline silicon has a lower onset of the absorption than a-Si:H, however the absorption in the visible range is lower. As $\mu\text{c-Si:H}$ can be fabricated with the same equipment as a-Si:H, it is convenient to build stacked solar cells of $\mu\text{c-Si:H}$ and a-Si:H to use the solar spectrum more efficiently. In case of tandem solar cells, an a-Si:H solar cell is on top of a $\mu\text{c-Si:H}$ solar cell. Putting the absorber with the higher bandgap on the illuminated side is advantageous, as all high energy photons are then absorbed by the high-bandgap layer. Thus, the low energy photons are absorbed in the second layer with the lower bandgap and losses due to thermalization are minimized.

Of course, the built in field decreases with increasing thickness and therewith the charge collection efficiency decreases. To overcome this problem, tandem solar cells consist of two fully functional solar cells. As a result of the series connection of the amorphous and microcrystalline solar cell, the voltages of both cells sum up, while the current is limited by the lowest current.

Wafer Based Solar Cells

In order to approach the theoretical efficiency limit of silicon solar cells, carrier selective contacts are needed. Carrier selective contacts have a low minority carrier recombination and a high majority carrier extraction efficiency. Silicon heterojunction solar cells, a mixed form of crystalline and thin-film silicon, are one attempt to approach the theoretical efficiency limit of 29.4 % [7,27–31,31–33]. The probably most famous is the Panasonic heterojunction with intrinsic thin layer (HiT™), where a record efficiency of 25.6% was achieved in 2014 [79]. In addition, a novel concept with tunnel oxide passivated contacts (TOPCon) was introduced in 2014 by Feldmann et. al [10]. As in this work the laser treatment of $\mu\text{-Si:H}$ is analyzed regarding its use for TOPCon solar cells, only this technique will be explained in the following.

TOPCon Solar Cells The TOPCon structure combines advantages of SHJ solar cells, the good selectivity due to the wide bandgap layer and the low parasitic absorption of semi-insulating polycrystalline silicon (SIPOS) emitters [35,80]. Instead of using a-Si:H with a high absorption in the short wavelength range, a semicrystalline layer is used. This can be achieved by thermal annealing of an a-Si:H thin-film for partial solid phase crystallization. The doped silicon layer is separated from the c-Si base by an optical transparent tunnel oxide layer (SiO_x). This oxide layer chemically passivates the wafer surface, reducing the surface state density and therewith the recombination at the c-Si /doped semicrystalline interface [7,10]. In addition, the tunnel oxide yields a heterostructure. However, the oxide layer has to be ultra-thin to allow tunneling of the majority carriers from the absorber layer to the doped layers [10–13,34]. This heterostructure prevents the back injection of minority carriers from the absorber into the doped layer, the emitter or the back surface field [34]. The back-injection is also reduced by a high net doping of the doped silicon thin-film layer.

Figure 2.8 a) presents the schematic cross section of a TOPCon solar cell. Figure 2.8 b) shows the schematic band diagram for the p-TOPCon heterojunction with n-type base. The heterostructure acts as an electric mirror, where minority carriers from the absorber cannot be reinjected into the doped silicon layer. Due to the band bending of the c-Si an efficient selective carrier extraction is realized [10,14]. Please note that the p-type back contact is still subject to research and a industrial feasible cell concept has not yet been demonstrated [10].

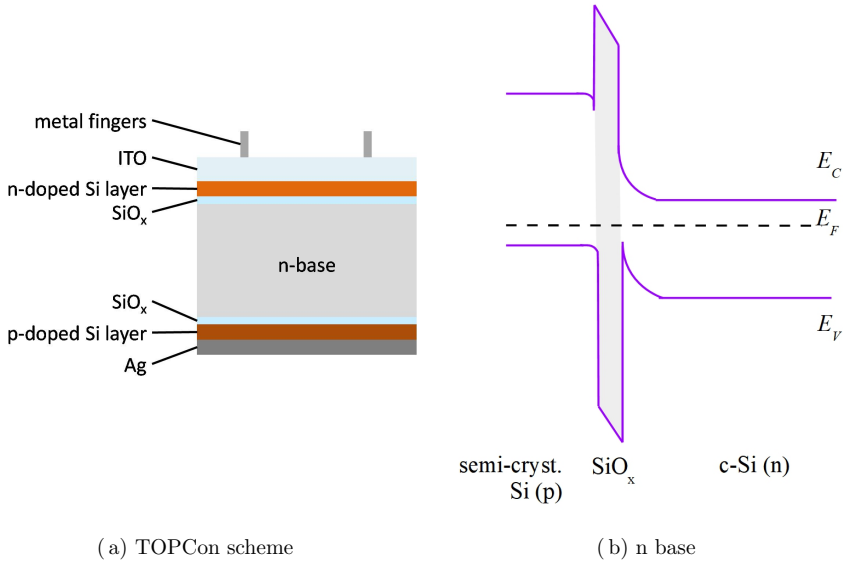


Figure 2.8: a) Schematic sketch of a TOPCon solar cell with c-Si(n) (gray). The tunnel oxide on both sides of the wafer is indicated in blue, the TCO - here Indium Tin Oxide (ITO) - is shown in gray, while the thin-film silicon is colored brown (p-type) and orange for n-type. b) Band diagram of the p-TOPCon/c-Si(n) heterostructure as demonstrated in [10].

2.2.1 Laser Processes in Solar Cell Fabrication

Lasers are already used for various applications in the production of solar cells. For instance, laser ablation processes are widely used for thin-film solar cells [81]. For example, laser scribing is used for isolation and interconnection of the individual functional layers of thin-film solar cells [61, 82–86]. In addition, lasers are used for edge-cleaning of solar cells and for structuring silicon wafers [87]. Laser processes are also included in the fabrication of crystalline solar cells. Here, laser ablation is used for the opening of the insulating layer [88]. Moreover, nanosecond lasers are used for contact opening, while femtosecond laser sources are used for structuring [88].

Moreover, lasers are used for liquid phase crystallization [46, 48, 89]. Here, the phase-transition from amorphous to crystalline is achieved by means of laser treatment. The use of lasers for the modification and optimization of material

properties is only logical as laser systems are already integrated in the production of solar cells.

2.3 Finite Element Method Simulations

For a better understanding of the physical processes and the verification of the experimental results of the laser treatment of a-Si:H, simulations were performed. In this work, the multi-physics program ELMER was used for heat transfer and diffusion simulations. Time and space dependent physical problems are in general described by partial differential equations (PDE). Though, most time these PDE cannot be solved analytically. Instead, numerical solutions are needed whenever the analytic solution is not possible. Hence, an approximation is achieved using discretization methods that use equations which can be solved with numerical methods.

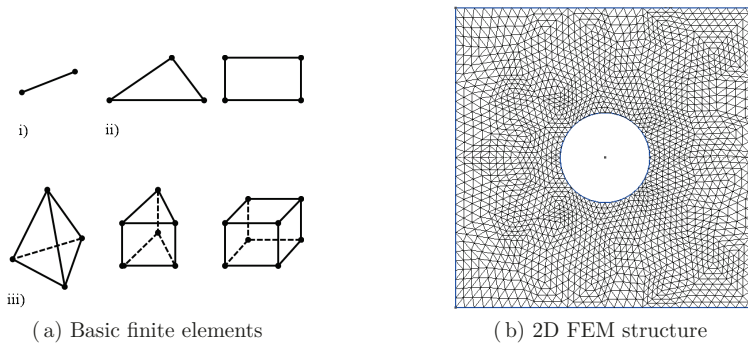


Figure 2.9: a) shows basic finite elements for 1D i), 2D ii) and 3D iii) structures. b) is an example of a 2D structure that is approximated with triangles.

In case for FEM, functions that are defined in a local area are used. Therefore, the simulation area is divided into finite elements. Each function is defined only on one element and zero on all other elements [90,91].

Figure 2.9 shows various finite elements, beginning with the most simple element for 1D simulation, a line. Finite elements for 2D simulations are either triangles or rectangles, while finite elements for 3D simulations can take various forms. In addition, a 2D structure divided into triangles is presented in Figure 2.9 b. This image demonstrates how the size of the finite element can change in order to approximate desired shapes.

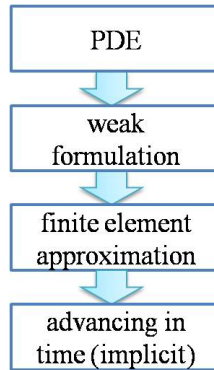


Figure 2.10: Basic concept of solving a multiphysics problem with ELMER

Figure 2.10 illustrates the concept for FEM simulations as used in ELMER. Based on the PDE, a weak formulation (or variational formulation) of the problem is formed. A weak formulation is an alternative function to express a PDE, though it is not an exact solution and the weak formulation is only defined in a local area (finite elements). In this work, the Garlekin finite element method of ELMER is used for the weak formulation.

After the weak formulation is obtained, the simulation structure has to be divided into finite elements [91,92]. The geometries as well as the meshes in this work were generated with Gmesh© [93].

Time Integration Time dependent solutions were needed for this work. Here, backward differential formulas (BDF) that are based on numerical differentiation are used for the time discretisation. Simulations were either performed with a BDF order of 2, or in case of adaptive time-stepping with a BDF order of 1 (= backward Euler).

Elmer Model Setup Figure 2.11 illustrates the work flow for simulations with ELMER. First, the geometry is designed and the mesh is calculated (here: Gmesh©). This mesh is then transformed into a file format that is compatible with Elmer (here: ElmerGrid).

Next, the model has to be defined in ELMER within the solver input file (.sif). Therefore, the

- coordinate system
- simulation type (steady state or transient)

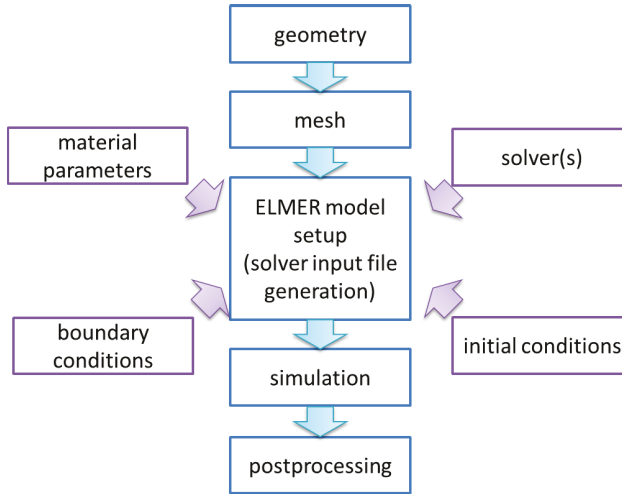


Figure 2.11: Process flow for simulations with ELMER

- timestepping parameters
- timestepping method

have to be defined for the simulation. Third, the physical models that have to be solved must be declared (e.g. Heat, Advection-Diffusion).

The material section of the solver input file contains all material specific parameters for the designated material. In addition, initial conditions and boundary conditions (BCs) can be declared for the ELMER solver input file. Boundary conditions define the constraints of a PDE on the boundary. They can be defined by a constant value (e.g. a temperature) in case of Dirichlet BCs or the value of the normal derivative of the function in case of Newman BCs (e.g. a heating rate).

After the simulation the obtained data is post-processed with any desired program (e.g. octave, Origin, ElmerPost, Paraview etc) and analyzed.

2.3.1 Heat Transfer Model

Solving the heat equation is often a linear problem. However, the temperature dependence of the heat conductivity and radiation effects result in a nonlinear problem. The heat equation, as used in ELMER is defined as:

$$\rho c_p \left(\frac{\partial T}{\partial t} + (\vec{u} \nabla) T \right) - \nabla \cdot (\kappa \nabla T) = \rho h, \quad (2.3)$$

where c_p is the heat capacity at constant pressure, ρ is the density, T is the temperature, \vec{u} the convection velocity, κ the thermal (heat) conductivity and h is the source of heat. Hereby, it is assumed that there is no frictional viscous heating. In addition, the convection velocity is $\vec{u} = 0$ for solids and the rate of heat generation is defined as $\rho h = Q$, resulting in [92]:

$$\rho c_p \left(\frac{\partial T}{\partial t} \right) - \nabla(\kappa \nabla T) = \rho h = Q. \quad (2.4)$$

The increase of heat is described with $\partial T / \partial t$ and the rate of heat conduction is described with $\nabla(\kappa \nabla T)$, respectively. Heat transfer simulations are conducted for a-Si:H on glass substrates in this work. The corresponding material parameters for the heat conductivity κ , the heat capacity c_p and the density ρ are listed in Table 2.1. In addition, the temperature dependence of $\kappa_{\text{a-Si}}$ and κ_{Corning} is plotted in Figure 2.12. For comparison, the thermal conductivity of c-Si is added.

Table 2.1: Material parameters used for heat transfer simulations [94, 95]

| material | parameter | value |
|-----------------|--|--------------|
| a-Si | thermal conductivity κ [W/(Km)] | Fig. 2.12 a) |
| | heat capacity c_p [J/(kgK)] | 1000 |
| | density ρ [kg/m ³] | 2150 |
| Corning EagleXG | thermal conductivity κ [W/(Km)] | Fig. 2.12 a) |
| | heat capacity c_p [J/(kgK)] | Fig. 2.12 b) |
| | density ρ [kg/m ³] | 2380 |

The heat generation in this thesis is a result of the absorption of light. The reflectance, as determined with a spectrophotometer (see Ch. 3, Sec. 3.3.3), was taken into account for the heat transfer simulations. However, a dependency of the refractive index and the absorption on temperature and hydrogen concentration were not taken into account. As $d_{\text{a-Si}} \ll d_{\text{substrate}}$, surface absorption was assumed for the exclusively heat-transfer simulations. Consequently, only the material parameters of Corning EagleXG have to be considered in this case. The temperature dependence of c_p is presented in Figure 2.12 b). Here, the squares refer to the values obtained from the data sheet, while the values in-between are approximated with a linear dependency.

Considering the diffusion simulations (see next section), an approximation with a constant value for c_p , a-Si was made as no reliable data was available for the a-Si:H used in this work.

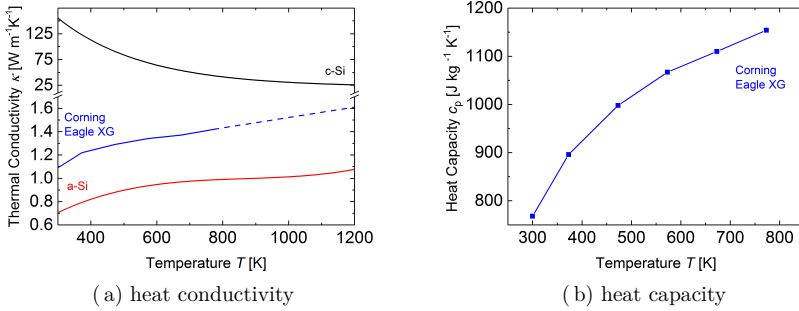


Figure 2.12: Fig. 2.12 a) thermal conductivity depending on the temperature of a-Si:H (red line), Corning Eagle XG (blue line) and c-Si (black line) [92,94,95]. Here, the dashed part of the blue line indicates the linear extrapolation made where no data were available. Fig. 2.12 b) shows the temperature dependence of c_p of Corning Eagle XG [94].

2.3.2 Diffusion Model

In general, the advection-diffusion equation is expressed in relative mass concentrations ($c = C/\rho$) or in absolute mass concentrations $C = [\text{kg}/\text{m}^3]$, while ρ is the density of the mixture. All simulations in this work were performed with absolute mass concentrations. The index i refers to the material specific properties that are given in Table 2.1 and Table 2.2.

Table 2.2: Material parameters used for diffusion simulations of Equation 2.7, 2.6 and 2.5 [61,92,96,97]

| material | parameter | value |
|--------------|---|----------------------|
| a-Si | diffusion coefficient prefactor D_0 [m ² /s] | 10^{-7} |
| | activation energy E_A [eV] | 1.3 |
| c-Si | diffusion coefficient prefactor D_0 [m ² /s] | 8.9×10^{-7} |
| | activation energy E_A [eV] | 0.58 |
| fused silica | diffusion coefficient prefactor D_0 [m ² /s] | 8.1×10^{-7} |
| | activation energy E_A [eV] | 0.2 |

$$\rho \left(\frac{\partial c_i}{\partial t} + (\vec{v} \nabla) c_i \right) = \rho \nabla (D_i \nabla c_i) + S_i \quad (2.5)$$

In case of solids, the velocity field \vec{v} is zero. For solids, without source or sink, the advection-diffusion equation reduces to the diffusion equation, driven by the first (eq. 2.6) and second law (eq. 2.7) of Fick.

$$\frac{\partial C_i}{\partial t} = \nabla (D_i \nabla C_i) \quad (2.6)$$

$$D_i = D_0 \exp \left(\frac{-E_A}{k_B T} \right) \quad (2.7)$$

Equation 2.7 describes the temperature dependence of the diffusion coefficient D_i . Here, D_0 is the diffusion coefficient prefactor, E_A the activation energy, k_B the Boltzmann constant ($k_B = 8.617 \times 10^{-5}$ eV/K) and T is the temperature. Though, neither the dependency of E_A nor D_0 on the temperature and the hydrogen concentration were considered.

3 Characterization Methods

3.1 Thin-Film Layer Thickness

The knowledge of the film thickness d is necessary to calculate material properties such as conductivity, absorption coefficient or the sub-bandgap absorption. In this thesis, thin-films were deposited on glass substrates as well as on *c*-Si wafers. The thickness on glass substrates is measured, using a stylus profiler (Veeco DEKTAK 6M Stylus Profiler), while the film thickness on *c*-Si wafers is measured by spectroscopic ellipsometry (SE).

Stylus Profiler After layer deposition, a laser system was used to ablate double lines of the deposited film. After that, the height difference between the layer and the substrate can be determined. Therefore, the stylus is moved in contact with the sample over the sample. Scanning speed and stylus pressure as well as the expected step height can be adapted to the sample. The height difference is determined from the analogous signal of the height position of the stylus. However, due to the necessity to ablate parts of the thin-film, this is a destructive measurement method. For this thesis, laser lines were ablated as an example on one $10 \times 10 \text{ cm}^2$ glass substrate of each deposition at five different positions and the average step height was calculated.

Spectroscopic Ellipsometry (SE) In order to determine the thickness of $\mu\text{-Si:H}$ on *c*-Si wafers, SE measurements were performed. For the samples used in this thesis the change in the polarization state of a light beam upon reflection is determined [98]. The ellipsometry angles ψ and Δ are defined by

$$\tan \psi e^{i\Delta} = \frac{r_p}{r_s} \quad (3.1)$$

Hereby $\tan \psi$ is the amplitude change upon reflection and Δ is the phase shift, respectively. The complex amplitude reflection coefficients are denominated r_s and r_p . The index s is assigned to the component of the electric field that vibrates perpendicular to the plane of incidence, while p is the component that oscillates parallel to the plane of incidence. Using a model based analysis, parameters like film thickness and refractive index can be determined out of ψ and Δ . Here, the resulting layer thickness was calculated with SCOUT©.

3.2 Electrical Characterization

3.2.1 Photo- and Dark Conductivity Measurements

Electrical properties, like the dark- and photoconductivity are part of the minimum set of parameters, required to characterize amorphous and microcrystalline silicon [21]. The quotient of the dark conductivity and the photoconductivity is referred to as photoresponse. The dark conductivity, the photoconductivity and in particular their ratio give information about the material quality regarding its use as solar cell absorber material, as conductivity measurements give information about the influence of impurities as well as the type of impurities.

In order to determine the dark- and photoconductivity, a single layer of a-Si:H or $\mu\text{c-Si:H}$ is deposited on a highly resistive glass substrate. In this work Corning Eagle XG was used. Two coplanar silver contacts with a thickness of $d = 700$ nm were evaporated on the thin-films, as illustrated in Figure 3.1. For dark- and photoconductivity measurements, the thickness of the semiconductor layer has to be taken into account. Hereby, the thin-film should be high enough to avoid the extension of the depletion to areas exterior the contacts. On the other hand, it has to be thin enough to guarantee the excitation throughout the whole film during photoconductivity measurements. In this work, dark- and photoconductivity measurements were made for a-Si:H. In order to meet the criteria just mentioned, the thickness of the a-Si:H layer was set to approximately 300 nm.

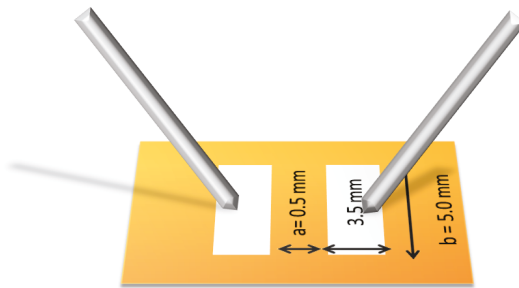


Figure 3.1: Measurement scheme for photo- and dark conductivity measurements. Two silver (Ag) contacts with a size of 3.5×5 mm and a distance of $a = 0.5$ mm are deposited on the thin-film. They are contacted with pogo pins.

The dark conductivity is defined as

$$\sigma_{\text{dark}} = \frac{Ia}{Vbd}, \quad (3.2)$$

while I is the measured current, V the applied voltage, a the distance between the contacts, b the length of the contacts (perpendicular to the current flow) and d is the layer thickness. The contacts have a size of $3.5 \times 5 \text{ mm}^2$. The distance between the contacts is $a = 0.5 \text{ mm}$. In a standard measurement $V = 100 \text{ V}$ is applied to the contacts.

The photoconductivity is determined in the same manner. The only difference is, that it is performed under illumination using the AM 1.5 spectrum with an energy intensity of 100 mW/cm^2 . Under irradiation the number of free carriers increases and the amount of free carriers is limited only by recombination. Both, photo- and dark conductivity measurements were performed under vacuum conditions.

3.2.2 Sheet Resistance Measurements

Kelvin Resistance Measurements are used to determine the sheet resistance R_{sh} of a thin-film. This is a 4-point-method where two contacts are used to apply a current to the sample, while the other two contacts are used to measure the voltage drop.

In this work, two different measurement systems are used to determine the sheet resistance. For samples that are much larger than the distance between the contacts, a linear setup can be used. In order to determine the sheet resistance of small samples, the Hall measurement setup is used (see Sec. 3.2.3).

The setup of the linear measurement system is illustrated in Fig. 3.2. The distance of the contacts D has to be considerably smaller than the sample size. A current I is applied between the outer contacts, while the voltage drop V due to the sheet resistance is measured between the inner contacts. The voltmeter has a high inner resistance and the contact resistances as well as the wire resistances can be neglected compared to the sheet resistance. For equidistant contacts, the resistivity ρ is

$$\rho = \frac{V}{I} 2\pi D. \quad (3.3)$$

A geometry specific correction factor f must be introduced to calculate the sheet resistance R_{sh} . In this work the focus was on the influence of a specific treatment on the sheet resistance, not on the absolute value. For samples with equal geometry, the correction factor can be neglected to determine the relative change in the sheet resistance.

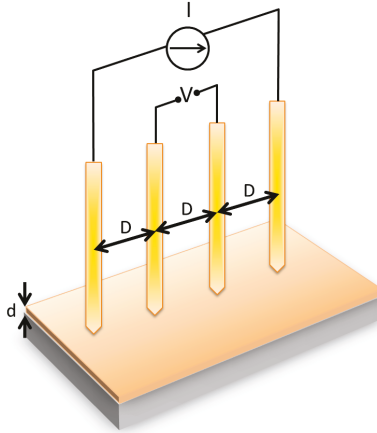


Figure 3.2: Sketch of the setup for the measurement of the sheet resistance using a linear contact alignment. The distance of the contacts is D and the film thickness is d . A current I is applied between the outer contacts, while the voltage drop V due to the sheet resistance is measured between the inner contacts.

3.2.3 Determination of Hall Mobility and Carrier Density

The Hall effect is used to determine the carrier concentration p , n and the mobility μ of a semiconductor. In addition, the electrical conductivity σ can be obtained, as it is proportional to the product of the carrier concentration n , p and the mobility μ . In this work, Hall measurements are performed for p-type $\mu\text{-Si:H}$ in order to qualify the influence of laser treatments on electrical properties. Therefore, the resistivity, the majority carrier density, and the Hall mobility are determined before and after laser treatment.

Hall Mobility and Carrier Concentration In order to perform Hall measurements, a sample with the film thickness d is placed in a magnetic field \vec{B} (here: z-direction Fig. 3.3) that is perpendicular to the thin-film. A voltage is applied between two opposite contacts (here: 2 and 4, x-direction). Due to the Lorentz force, the charges are separated in the magnetic field. This charge separation creates an electric field (here: y-direction), opposing further charge migration. As long as the charge is flowing, a steady electrical potential builds up. This potential, the Hall voltage V_H , can be measured perpendicular to both the applied current flow and the magnetic field (V_H here: 1 and 3, y-direction).

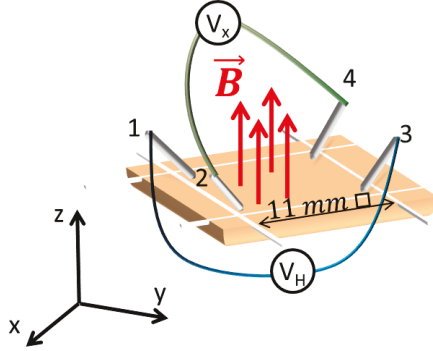


Figure 3.3: Measurement scheme for Hall measurements. Here, the voltage is applied between the contacts 2 and 4. Due to the magnetic field that is perpendicular to the thin-film, the Hall voltage can be measured between the contacts 1 and 3.

The resistivity ρ of a square shaped sample with its contacts in the four corners is given by:

$$\rho = F \frac{\pi d}{2 \ln 2} (R_1 + R_2). \quad (3.4)$$

Hereby F is a correction factor for asymmetric samples, R_1 and R_2 are the resistances derived from the Kelvin resistance measurements that are explained in detail in the last subsection (Sec. 3.2.2). All samples used in this work are square shaped resulting in $F \approx 1$. By convention the Hall voltage V_H denotes as

$$V_H = vBw \quad (3.5)$$

where v is the drift velocity of the electrons, B the magnetic force perpendicular to the sample and w is the width of the sample. Considering the measurements the Hall voltage V_H is obtained with:

$$V_H = \frac{R_H I}{d} \quad (3.6)$$

while R_H is referred to as Hall coefficient. The schematic setup of the measurement configuration is illustrated in Fig. 3.4. The Hall voltage V_H is measured between both opposite contact pairs, 1, 3 and 2, 4 respectively. In addition, the direction of the magnetic field \vec{B} is applied for both the positive and negative z-direction (see Fig. 3.3). Following the convention, the crossed circles refer to

a magnetic field pointing into the plane of drawing while the dotted point in opposite direction. This leads to four measurements.

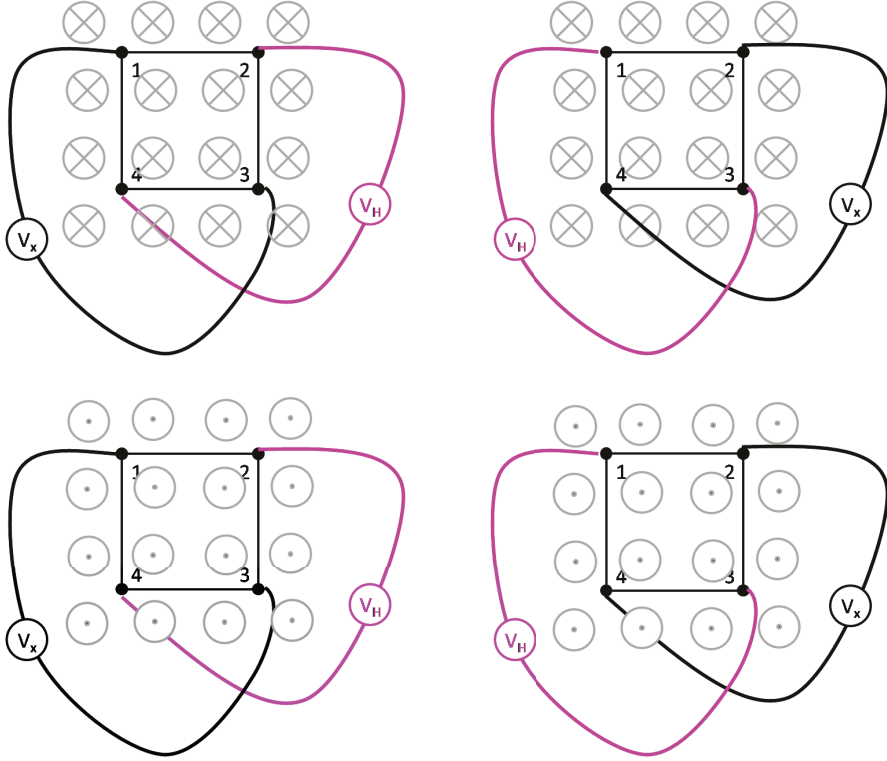


Figure 3.4: Schematic configuration of the four different conditions for the determination of the Hall voltage V_H . The Hall voltage is measured between both opposite contact pairs (1,3 and 2,4). The crosses in the circles refer to a magnetic field \vec{B} pointing into the paper, while those with crosses point outside, respectively.

The Hall coefficient R_H is obtained automatically by the measurement system with

$$R_H = \frac{D}{2B} (R_{+B} - R_{-B}) \quad (3.7)$$

where D is the distance between the contacts (here: 1,3 and 2,4). The carrier concentration, mobility and the carrier type are calculated with

$$\rho = \frac{1}{q} \frac{1}{(p + nb)\mu_p} \quad (3.8)$$

and

$$R_H = \frac{1}{q} \frac{p - nb^2}{(p + nb)^2} \quad (3.9)$$

Hereby b is the quotient of the mobilities $b = \mu_n/\mu_p$ of a semiconductor. In a p-doped semiconductor is $p \gg n$. As a consequence, only the concentration and the drift mobility of the majority carriers (here: p , μ_p) have an impact. This leads to a simple relation of the Hall mobility with

$$\mu_H = r_H \mu_p \quad (3.10)$$

for a p-type semiconductor. the Hall factor r_H is constant. For large magnetic fields with $B \gg 1/\mu$, as used in this work, $r_H = 1$. Finally, this leads to the resistivity ρ , the Hall coefficient R_H , the p-type carrier concentration p and the mobility μ_p .

$$\rho = \frac{1}{qp\mu_p} \quad (3.11)$$

$$R_H = \frac{1}{qp} \quad (3.12)$$

$$p = \frac{1}{qR_H} \quad (3.13)$$

$$\mu_p = \frac{R_H}{\rho} \quad (3.14)$$

The sign of the Hall constant V_H characterizes the type of charge carriers and doping, respectively. In general, a negative Hall constant V_H is related to electrons, while holes have a positive sign. However, a-Si:H exhibits opposite signs. This effect has been investigated for many years but is not yet fully understood [17,99].

For this thesis a PhysTech™ RH2030 Hall Effect Measurement System was used to determine the influence of laser treatment on the the carrier concentration p , the mobility μ_p and the resistivity ρ of $\mu\text{c-Si:H}$.

For the Hall measurements, a square sample is needed. This sample is contacted at four points in a square $10 \times 10 \text{ mm}^2$ configuration, while the contacts should be small compared to the sample surface. In this work, laser scribing was used for the electrical isolation of the samples. To facilitate the contacting with the four pogo pins of the PhysTech® RH2030 a square surface of $w_{\square} = 11 \text{ mm} \times 11 \text{ mm}$ was

isolated electrically for the samples used in this work (Fig. 3.3). As the mechanical setup of the measurement system does not allow sample sizes of $10 \times 10 \text{ cm}^2$, the substrate was cut into individual samples. The geometry is described in detail in 3.2.2.

Sheet Resistance The Hall measurement setup used in the work makes use of the van-der-Pauw method to measure the sheet resistance. This method requires a uniform film thickness throughout the measured sample. The resistance R is calculated with

$$R = \frac{l}{\sigma db} = R_{\text{sh}} \frac{l}{b} \quad (3.15)$$

$$R_{\text{sh}} = \frac{1}{\sigma d} = \frac{\rho}{d} \quad (3.16)$$

where l is the length, d the layer thickness, and b the width of the sample. For the special case of a square sample, as used in this work, is

$$R = R_{\text{sh}}. \quad (3.17)$$

When using the Hall measurement setup, the specific resistivity ρ and the Hall coefficient R_{H} are both determined with this 4-point method. A preset sample specific current is used to measure the I/V characteristic of the sample. Afterwards, the resistivities are calculated from the I/V data, using linear regression. The conductivity σ is defined as

$$\sigma = ne\mu, \quad (3.18)$$

while n is the carrier concentration, e the elemental charge and μ the carrier mobility. The principle of Kelvin probe measurements is illustrated in Fig. 3.5.

Measurement Instability During the characterization of the $\mu\text{-Si:H}$ samples on glass it was found that the Hall mobility and the carrier density are subject to systematic measurement instabilities, while the measured resistivity was constant for subsequent measurement. Either the carrier density decreased with subsequent measurements, while the Hall mobility increased on the same time, or vice versa. Nevertheless, the values of the first measurement were recovered after waiting or re-contacting of the sample.

As a consequence of the subsequent measurements of the samples, the measurement error seems to be higher for the measurements of the Hall mobility and the carrier density than it is in reality. However, this effect was not observed for the GaAs reference or other samples. The resistivity, which is the product of the mobility and the carrier density, is constant for subsequent measurements.

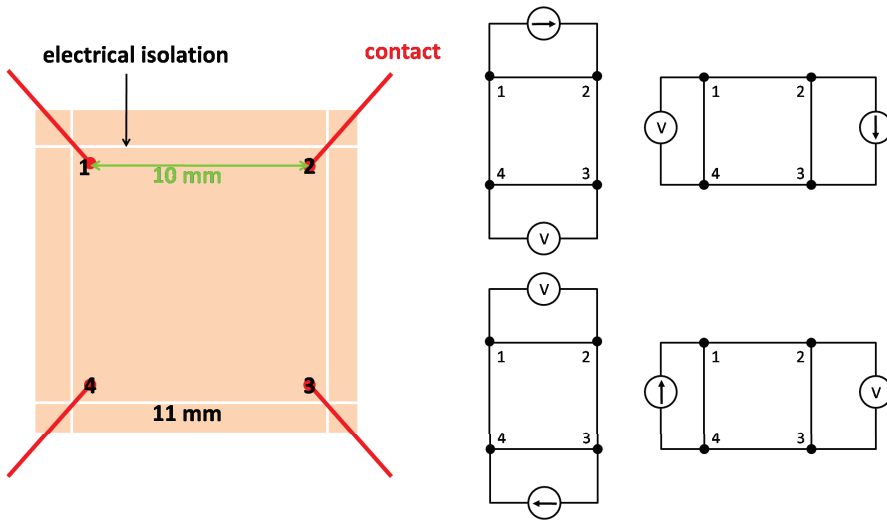


Figure 3.5: Scheme of Kelvin Resistance Measurement. The geometry of the sample is illustrated on the left side, while the four different electrical contact schemes are illustrated on the right. The current flows between one contact pair in forward and backward direction, while the voltage drop is measured between the second contact pair. Current source and voltage measurement are altered in order to contact each contact of the sample once.

Hence, the resistivity was used in this work to evaluate the influence of the laser treatment on $\mu\text{c-Si:H}$. Further investigations that are beyond the scope of this thesis would be necessary to investigate this systematic measurement instability.

3.3 Spectroscopy

3.3.1 Raman Spectroscopy

Raman spectroscopy is a fast, non-destructive and contact free material analysis method that measures the specific vibrational modes of matter. Therefore, light that is inelastically scattered on matter is analyzed. The frequency shift between the incoming and the scattered light is referred to as Raman shift ν and is indicated in wavenumbers cm^{-1} [100]. Raman spectra are unique fingerprints, enabling qualitative material analysis. Moreover, Raman spectroscopy is intensity sensitive and quantitative analysis can be performed. It can be applied as well for liquids and gases as for solid state matter.

The inelastic scattering of light on matter was first demonstrated by Chandrasekhara Venekata Raman (C. V. Raman) [100], who observed the effect in liquids. In this work, Raman spectroscopy is used to detect changes in the hydrogen concentration of a-Si:H, its microstructure, and to measure the crystallinity of a-Si:H and $\mu\text{c-Si:H}$.

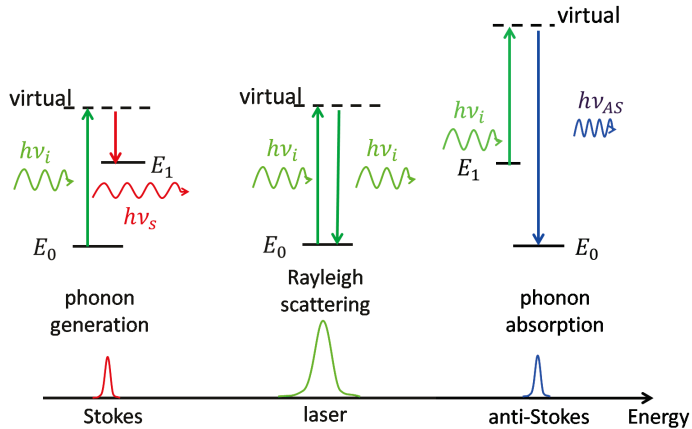


Figure 3.6: Principle of Raman scattering. In case of Stokes-shift, photons transfer energy to the phonons (left) leaving the molecule in an excited state. In case of the anti-Stokes shift, the molecule is in an excited state before the inelastic scattering. The photons absorb energy from the phonons. Consequently the energy of the scattered light is higher than the incoming light in case of the anti-Stokes shift while the energy of the scattered light is lower in case of the Stokes shift.

Figure 3.6 presents the principle of Raman scattering. Raman scattering is based on the energy exchange of light between the photons of the incident light and the phonons (lattice oscillations or molecular vibrations) of the matter due to inelastic scattering. As a consequence of the energy exchange, the energy of the incident light changes and the scattered light has a shifted frequency. The energy exchange can result either in an increase or a decrease of the energy of the scattered light. Hereby, the molecule is pumped into a virtual energy state due to the interaction with the incident light. In case of the Stokes shift, the molecule is in ground state before the interaction with the light and the molecule vibrations (phonons) absorb energy from the incident light. As a consequence, the scattered light has a lower energy than the incident light. In the second case, the anti-Stokes shift, the molecule is already in an excited state before the interaction with the incident light. Due to the inelastic scattering, the incident light absorbs energy from the molecule vibrations (phonons). Consequently, the inelastically scattered light has a higher energy than the incident light. The absolute value of the energy change is equal for both Stokes and anti-Stokes. The principle of Raman and Rayleigh scattering is illustrated in Figure 3.6.

In general, Raman activity requires the change of the polarisability α during the oscillation. This is referred to as "selection rule". However, in amorphous material like a-Si:H the selection rule is not valid.

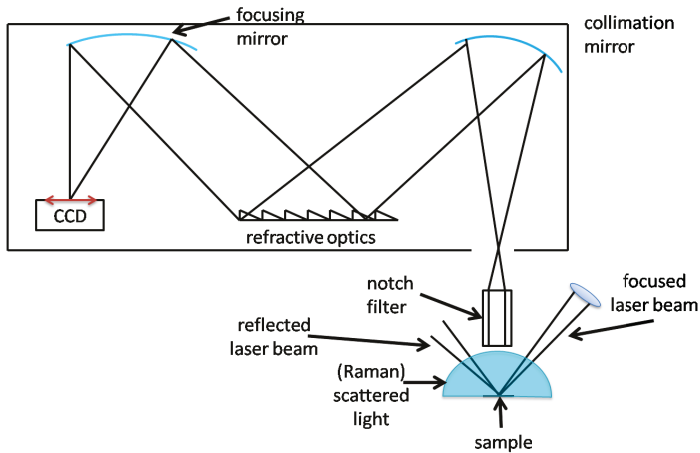


Figure 3.7: Schematic setup for Raman spectroscopy. A laser beam is focused on the sample. The scattered light passes through a notch filter into a spectrometer where it is detected by a camera.

The scheme of Raman spectroscopy is illustrated in Figure 3.7. A narrowband light source (e.g. laser) is needed for Raman spectroscopy in order to enable the detection of the frequency shift. In addition, the frequency of the excitation ν_0 light source must neither be too high, nor too close to the eigenfrequency of the molecules or lattice vibrations. If the excitation frequency ν_0 is too high, the Compton effect is too pronounced and interferes. On the other hand, for a very low excitation frequency close to the eigenfrequencies, the interaction of light with matter cannot be explained with standard scattering theories. Therefore, primary light sources in the visible range are favorable for Raman spectroscopy. In addition, the wavelength of the inelastically scattered light will also be in the visible range, or very close to it. Hence, powerful detectors (e.g. Si-CCD) are available at large range. As the intensity of the inelastically scattered light is several orders of magnitude smaller than the intensities of elastically scattered light, powerful optical filters and gratings are needed to filter the elastically scattered light.

Raman spectroscopy is a non-destructive method and in case of solid states, as used for this work, no specific sample preparation is required. In this work, Raman spectroscopy was operated in backscattering mode with excitation at $\lambda = 532$ nm and $\lambda = 488$ nm.

3.3.2 Fourier Transform Infrared (FTIR) Spectroscopy

Fourier transform infrared spectroscopy is based on the absorption of incident light in the layer of interest. Due to the absorption, bond vibrations can be induced. The vibration mode, which is induced between two (polar!) bonds is subject to the wavelength of the infrared light. Depending on the quantity of vibrational bonds induced at a certain wavelength, the amount of the absorbed part will increase with the amount of triggered bonds. In short, the higher the amount of absorption for the infrared wavelength is, the higher is the amount of the bonds that are triggered at that wavelength.

Fourier transform infrared spectroscopy is a standard method to determine the microstructure and the hydrogen concentration c_H of amorphous silicon [17, 21, 101]. The microstructure parameter R^{IR} is considered as a figure of merit for the material quality of a-Si:H [102].

Historically, the stretching modes centered at 2100 cm^{-1} were attributed to di- and tri-hydrides (Si-H_2 and Si-H_3), while those centered at 2000 cm^{-1} were attributed to Si-H [17, 21, 103–105]. It should be noted that both 2100 cm^{-1} and 2090 cm^{-1} are found in literature. However, they both refer to the same stretching mode. In this thesis 2100 cm^{-1} is used. Wagner and Beyer showed that the stretching mode absorption centered at 2100 cm^{-1} is related to surface bound hydrogen in voids whereas the 2000 cm^{-1} mode can be attributed to hy-

drogen incorporated in a dense material [57]. High micro-void densities in a-Si:H are related to material with potentially high degradation [17]. The ideal a-Si:H structure is linked with the peak at 2000 cm^{-1} while the peak at 2100 cm^{-1} is related to a deviation from the ideal structure [17, 105–107]. The microstructure parameter is defined as

$$R^{IR} = \frac{I_{2100}}{I_{2000} I_{2100}}, \quad (3.19)$$

while I_{2000} and I_{2100} are the intensities of the FTIR signal at 2000 cm^{-1} and 2100 cm^{-1} , respectively. Shah [17] states, that the R^{IR} should be 0.2 or smaller, while Schropp [21] defines a R^{IR} of 0.1 or smaller as requirement for device grade material.

In addition to the determination of the R^{IR} , these modes (2000 cm^{-1} , 2100 cm^{-1}) as well as the SiH_n wagging mode at 640 cm^{-1} can be used to calculate c_H . The hydrogen concentration is proportional to the integrated FTIR signal at 640 cm^{-1} or the peak sum of 2000 cm^{-1} and 2100 cm^{-1} .

$$c_H = A \int \frac{\alpha(\omega)}{\omega} d\omega \quad (3.20)$$

where A is a proportionality constant and α is the absorption coefficient at the wavenumber ω . [17, 21, 104, 105]

However, an infrared transparent substrate is required. As a consequence, layers that are deposited on glass substrates cannot be analyzed with FTIR spectroscopy. Thin-film solar cells are mostly deposited on glass substrates. Consequently, this method is not appropriate for in-production process control and analysis. FTIR spectroscopy requires the deposition on c-Si substrates as a reference for analysis.

3.3.3 Reflectance, Transmittance and Absorptance

The spectral reflectance $R(\lambda)$ and transmittance $T(\lambda)$ are measured with an optical spectrometer. However, the absorptance is calculated from the retrieved $T(\lambda)$ and $R(\lambda)$. In order to qualify the laser treatment, the knowledge of the reflectance of the samples and the absorptance within a specific layer is needed. The spectral absorptance $A(\lambda)$ is calculated with

$$A(\lambda) = 1 - R(\lambda) - T(\lambda). \quad (3.21)$$

Hereby, $T(\lambda)$ and $R(\lambda)$ are determined with an optical spectrometer (Perkin ElmerTM LAMBDA 950).

For transmittance measurements the samples are placed in front of an integrating sphere, while the samples are placed behind the integrating sphere to measure the reflectance. The optical spectrometer used for this work has a spectral range from $\lambda = 250$ nm to $\lambda = 2500$ nm. Thus, the optical data can be retrieved within a margin of 2 %. As a result, low absorptance values cannot be retrieved with this method. Low absorption requires a different measurement setup, like Photothermal Deflection Spectroscopy (PDS) for example.

3.3.4 Photothermal Deflection Spectroscopy (PDS)

Photothermal deflection spectroscopy is used to measure the sub-bandgap absorption α of a thin-film. This method has a large measurement range that detects simultaneously the optical bandgap, or in case of amorphous silicon the mobility gap, the absorption in the band tails and the sub-bandgap energy. The sub-bandgap absorption of thin-films is in the range of 0.1 % to 0.2 %. Consequently, the sub-bandgap absorption cannot be detected with an optical spectrometer. PDS works on the principle of absorption of light and the resulting heat generation. As a consequence to the absorption of light in a semiconductor, phonons are generated by non-radiative recombination and the thermalization of photo-generated carriers.

For the PDS system used in this work, the sample size must not exceed 8 mm \times 15 mm. The samples are placed in a cavity with an optical transparent CCl₄ fluid. The refractive index of this fluid is highly sensitive to temperature changes. The sample in the cavity is illuminated with monochromatic light in the wavelength range between $\lambda = 310$ nm (halogen lamp) and $\lambda = 2600$ nm (high pressure xenon lamp). Due to the absorption of the incident light, the sample heats up and transfers the heat to the surrounding fluid. Then, the deflection of a laser beam in the CCl₄ fluid is measured in order to determine temperature changes of the CCl₄ fluid. A phase correction procedure using chopped light and lock-in technique is applied to reduce the contribution of glass substrate by delaying the substrate signal. The sub-bandgap absorption is directly related to deep defects in a-Si:H like dangling bonds. In this work PDS was used to evaluate changes in the sub-bandgap absorption due to laser treatment.

3.4 Photoluminescence (PL)

Photoluminescence (PL) imaging is a non-destructive method to obtain insight into the spacial resolved quality of a silicon wafer [108]. Luminescence can occur when the thermal equilibrium of a solid is disturbed. If this deviation results in the emission of light, this is referred to as luminescence. For a deviation

of the thermal equilibrium that is caused by the absorption of light, the term photoluminescence is used.

Photoluminescence imaging can be divided into two different types of measurements. First, PL imaging under steady state conditions where the generation is constant. PL imaging provides images with a high resolution, where the intensity is a qualitative indication for the local lifetime. The second type is referred to as PL lifetime or dynamic infrared lifetime mapping. Here, the resolution is smaller in both intensity counts and lateral resolution than for PL imaging. However, a carrier lifetime can be extracted. Photoluminescence measurements are contactless and no device structure is needed [108]. In addition, no special sample preparation is needed. Photoluminescence lifetime is a rather new method. The potential and accurateness are still under investigation.

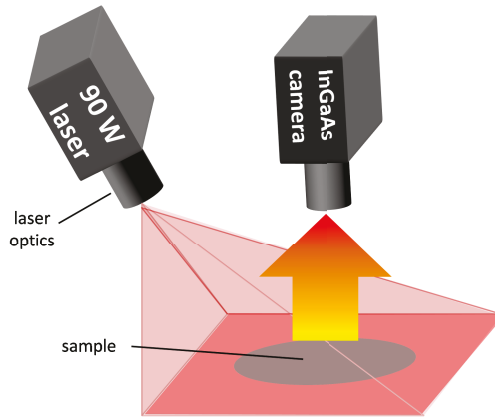


Figure 3.8: Scheme of the PL measurement setup. The sample (grey circle) is illuminated with a 90 W laser (light red). The luminescence is detected with a camera that is mounted over the sample.

The PL measurement system used for this thesis consists of a 90 W laser source at a wavelength of $\lambda = 808$ nm for the generation of the electron-hole pairs and an indium gallium arsenide camera for the imaging (Fig. 3.8). The camera is cooled at $T = -80$ °C. The sample is illuminated with 1 sun equivalent intensity, while the imaging time can be varied. Both, illumination and imaging occur from the side facing to the camera.

PL Imaging The PL intensity I_{PL} is proportional to the excess carrier concentration Δn with:

$$I_{\text{PL}} = c \tau_{\text{eff}} \quad (3.22)$$

where c is a material and system dependent constant and

$$\tau_{\text{eff}} = \frac{\Delta n}{G} \quad (3.23)$$

G denotes the generation rate per unit volume [108] and τ_{eff} effective minority carrier lifetime.

$$I_{\text{PL}} = C_{\text{cal}} (N_{\text{A/D}} + \Delta n) \Delta n \quad (3.24)$$

where C_{cal} is a calibration factor [109] and $N_{\text{A/D}}$ is the background doping.

In short:

$$I_{\text{PL}} \propto \tau_{\text{eff}} \propto \Delta n \quad (3.25)$$

Due to this proportionality, the PL intensity gives insight into the passivation quality and defects. The brighter the PL intensity the better is the passivation quality.

PL Lifetime Dynamic PL measurements (PL lifetime) are used to gain insight into the time dependent behavior of Δn . To verify the obtained lifetime, the PL lifetime of as-deposited samples has been double-checked with results of quasi-steady-state photoconductance measurements [110].

Figure 3.9 illustrates the principle of the image acquisition to determine the lifetime. Four images (gray vertical markings) are recorded during each lock-in period. The width of these lines indicates the image acquisition time t_{int} . The solid black line refers to the generation rate (left y-axis), while the solid red curve illustrates Δn (right y-axis), respectively. Both, the generation rate and the excess carrier density have been normalized to their maximum values. The first image records Δn during its exponential rise, the second image is recorded after steady state conditions have been reached. Then a third image is taken when the generation light source is switched off and a fourth one after Δn has decayed. Latter is needed for background subtraction. The data acquisition and the image data processing is performed corresponding to Ramspeck et al. [111].

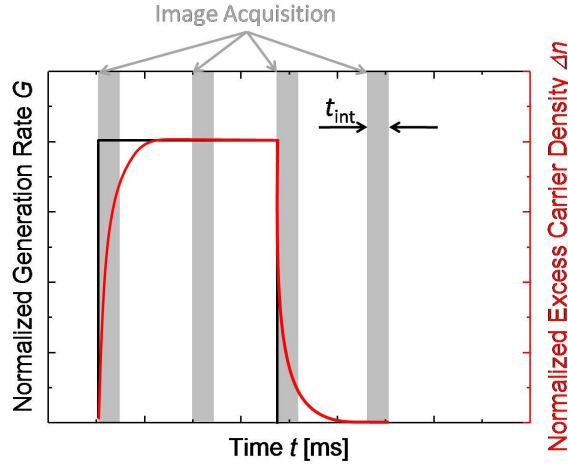


Figure 3.9: Principle of the image acquisition for dynamic PL measurements. The solid black line refers to the generation rate G (left y-axis), while the solid red curve illustrates the Δn (right y-axis), respectively. Gray vertical markings indicate the time of image acquisitions that are recorded during each lock-in period. The width of these lines indicates the image acquisition time t_{int} .

The resolution of steady-state PL images is orders of magnitude higher than of dynamic measurements. The dynamic images look blurred compared to the steady state image. Figure 3.10 shows exemplary the image obtained by dynamic PL (Fig. 3.10 a) and by steady-state PL (Fig. 3.10 b). One exemplary region where a defect cannot be resolved in the dynamic imaging is marked with the light blue circle on both images. This blurring is ascribed to internal total reflection of the infrared light inside the wafers.

Based on the higher spacial resolution of steady-state images, it is recommended to use those for the lateral analysis of the lifetime. The PL intensity images can be calibrated to the PL lifetime. For the calibration of the intensity images to the lifetime, the method as described by Ramspeck [112] is used. The relation of the local lifetime derived from steady state images τ_{SS} is proportional to I_{PL} . The PL intensity has to be multiplied with a sample specific factor X which is obtained by the quotient of the mean lifetime of the area with the highest lifetime $\tau_{\text{PL, max}}$ and the mean PL intensity $I_{\text{PL, max}}$ of the corresponding area.

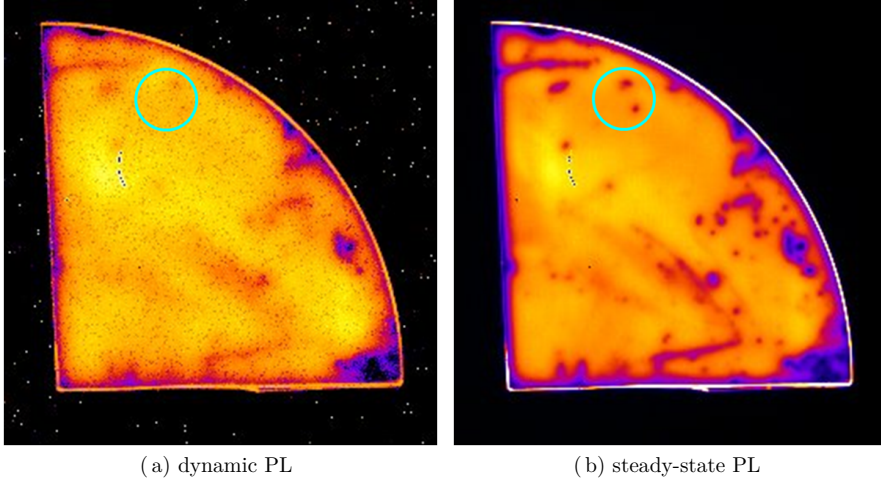


Figure 3.10: Dynamic PL (Fig. 3.10 a) and steady-state PL intensity (Fig. 3.10 b). One exemplary region where the dynamic PL cannot resolve the defect is marked with the light blue circle.

$$\tau_{SS} = I_{PL} \frac{\tau_{PL, \max}}{I_{PL, \max}} \quad (3.26)$$

The correction factors for the as deposited X_{as-dep} and the laser treated X_{as-dep} samples are defined as:

$$X_{as-dep} = \frac{\tau_{PL, \max, as-dep}}{I_{PL, \max, as-dep}} \quad (3.27)$$

$$X_{laser} = \frac{\tau_{PL, \max, laser}}{I_{PL, \max, laser}} \quad (3.28)$$

This calibration method for the PL images is applied in this work to gain detailed insight into the local influence of laser treatment on the passivation quality for c-Si wafers.

3.5 Secondary Ion Mass Spectrometry (SIMS)

Secondary Ion Mass Spectrometry (SIMS) analysis was used in order to determine the depth dependent hydrogen concentration. SIMS was applied to both, furnace annealed references and laser treated samples.

In SIMS analysis, primary ions are used to bombard material off the target to be analyzed. Those primary ions collide with a solid surface. The kinetic energy of the primary ions is transferred to the target, resulting in a sputtering process. The ions ejected from the target are referred to as secondary ions. Those secondary ions are analyzed with a mass spectrometer. Depending on the material to be analyzed, SIMS is rather qualitative than quantitative. Hydrogen, for example is part of the residual gas. Consequently, the quantitative values for hydrogen are falsified due to the hydrogen in the residual gas. Alternatively, the isotopes of the Si-H bondings with an atomic mass of $m_a \approx 31$ u can be analyzed. However, the contribution of Si-H₂ and Si-H₃ is neglected. The analysis will be explained in more detail in Chapter 6. The SIMS measurement was performed on the ToF-SIMS (Time-of-flight SIMS) in the Central Division of Analytical Chemistry, Forschungszentrum Jülich.

4 Laser Sources

This chapter is dedicated to the description of the laser sources and their setup as used in this work. In section 4.1, the characteristics of the 532 nm laser source will be presented. This section is divided into two subsections showing first the setup for the treatment of a-Si:H and secondly the setup for the treatment of μ -Si:H. Section 4.2 is dedicated to the 355 nm laser source used for the treatment of μ -Si:H as well as for the ablation of the electrical isolation lines.

4.1 532 nm (vis) Short Pulse Laser Source

In this work an EdgewaveTM HD30II-E Innoslab laser with a wavelength of $\lambda = 532$ nm is used. This laser has a tunable repetition rate of up to $\nu_{\max} = 60$ kHz. For the experiments performed in this thesis, the laser was operated at $\nu = 40$ kHz, with a resulting pulse duration of $\tau_{\text{pulse}} = (7.7 \pm 3.3)$ ns and a maximum laser power of $P = 150$ W [113]. The high deviation of the pulse duration results from the decrease of the pulse duration with increasing laser diode current. As the pulse duration is in the same order of magnitude for all laser diode currents applied in this work, this dependency on the laser diode current is not expected to affect the results.

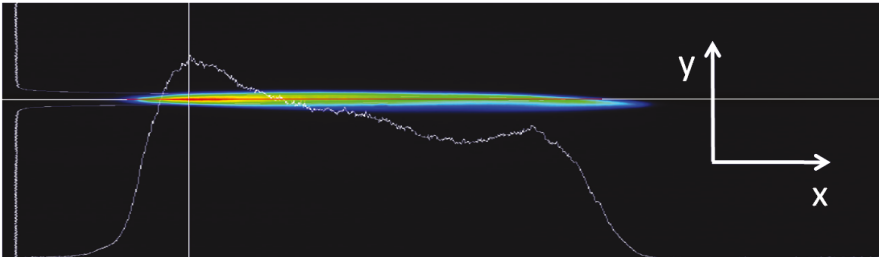


Figure 4.1: Intensity beam profile of the Edgewave HD30II-E Innoslab laser in far field setup. The intensity is presented as 2D false color plot. In addition, the intensity profile is shown for a line scan in both x-direction and y-direction. Source: [114]

This laser source should exhibit a line shaped beam profile, resembling a tophat intensity profile in the x -direction as well as in the y -direction. The far field beam profile, as characterized by the manufacturer EdgeWave GmbH, is presented in Fig. 4.1. The beam profile is shown in color scale, while the corresponding intensity is the white line in the graph in arbitrary units. The far field beam profile exhibits an asymmetric intensity profile in the x -direction and the maximum of the intensity is not in a centered position. The size of the far field beam profile, shown in Fig. 4.1, is measured at an intensity of $I = I_0 / e^2$.

This results in a far-field beam size of $w_x = 18642 \mu\text{m}$ in x -direction and $w_y = 143 \mu\text{m}$ in y direction, respectively.

4.1.1 Setup for the Laser Treatment of a-Si:H

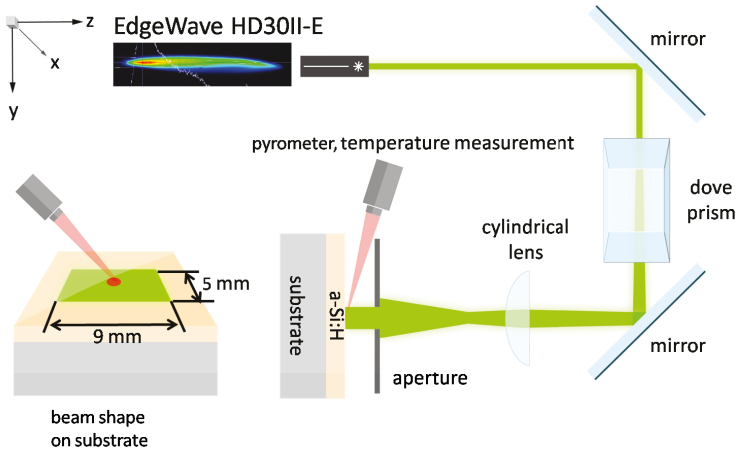


Figure 4.2: Sketch of the experimental setup for the treatment of a-Si:H. The line-shaped laser beam is magnified the y -direction with a cylindrical lens, while the x -direction is unmodified by optical beam shaping. In addition, the schematic laser beam profile on the substrate for the treatment of a-Si:H is shown. The irradiated surface (green rectangle) has a size of approximately $5 \times 9 \text{ mm}^2$ on the substrate (brown square).

With the aim of generating a laser treatment process that is independent of electrical translation stages, a rectangular beam profile with an area of approximately $4.5 \times 10^{-5} \text{ m}^2$ (Fig. 4.2) was shaped. To achieve this, the laser beam was

magnified in the y-direction using a cylindrical lens, while the beam in x-direction remained unmodified and was enlarged only due to the beam divergence (Fig. 4.2). Measurements of the beam profile showed a rotation in the x,y plane. In order to obtain an intensity beam profile that is symmetrical in both the x-axis and the y-axis, a dove prism was integrated in the beam path to rotate the laser beam. The principle of the beam path of the laser is sketched in Fig. 4.2. As illustrated in Fig. 4.2, the resulting irradiated area (green rectangle) on the substrate (brown square) has a size of approximately $5 \times 9 \text{ mm}^2$ after beam shaping.

The beam profile at the substrate position has been determined with a DataRay WinCamD beam profile camera for laser diode currents ranging from $I = 37 \text{ A}$ to $I = 53 \text{ A}$ (Fig. 4.3). Even though, the position of all optical elements and the beam profile camera were fixed, the maximum intensity shifted along the x-axis. This instability of the beam profile intensity can be traced to the laser source itself.

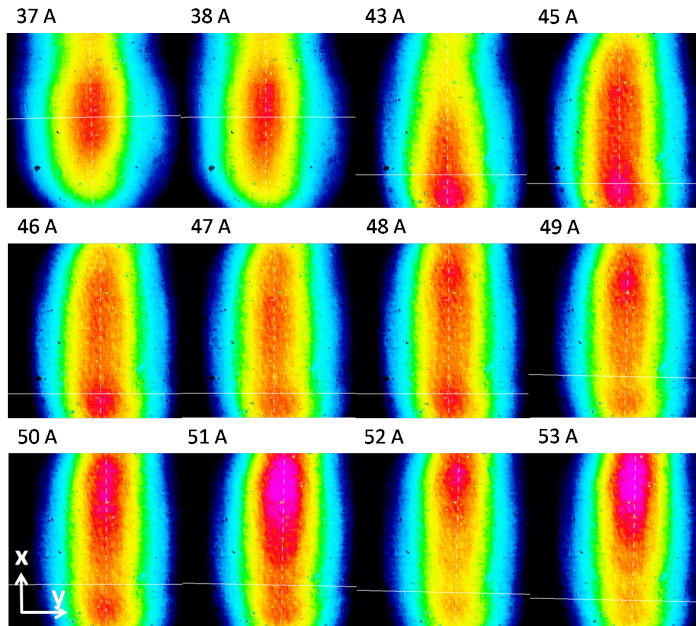


Figure 4.3: False color plot of the beam profile of the extended laser beam as used for the treatment of a-Si:H at sample position for laser diode currents ranging from $I = 37 \text{ A}$ to $I = 53 \text{ A}$.

With respect to having a suitable value to compare the results of the variation of the irradiation time and the laser power, the process temperature was chosen. A pyrometer was used to monitor the temperature development during and after irradiation and to obtain the maximum process temperature. The temperature measurements are described in detail in Chapter 5. As a consequence to the shifting of the position of the maximum intensity along the x-axis, the process temperature is not necessarily measured at the spot with the maximum laser intensity. However, it was attempted to measure the temperature, the hydrogen concentration, the conductivity, and the sub-bandgap absorption at the same spot on the sample. This should lead to consistent results, independent on the shifting of the maximum laser intensity.

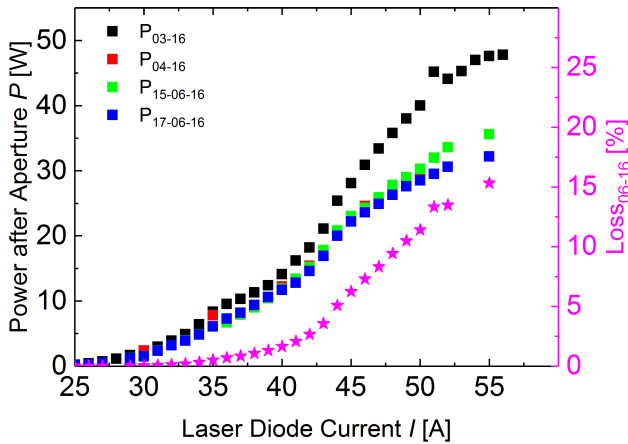


Figure 4.4: Laser power after the rectangular aperture, measured at different dates. Black squares refer to the initial power, while red, green, and blue refer to later dates, respectively. The power measured at the end of the experiments is plotted in blue squares. The loss of the laser power is indicated on the right y-axis (pink stars).

In addition, the average power of the laser was measured directly after the aperture (see Fig. 4.2). The dependency of the average power P on the laser diode current is shown in Fig. 4.4. Repeated measurements during the course of the experiments revealed a decrease of the laser power after the aperture with increasing operating hours of the laser system. The initial laser power, as determined at the beginning of this experimental series is plotted in black squares. The subsequent

measurements are shown in red, green, and blue. The percentage power loss at the end of the experiments compared with the initial power is indicated with the pink stars on the right hand y-axis. This power loss could be traced back to a degradation of the dove prism. Preliminary experiments were performed with the initial laser power, while the final results of this thesis were produced with the degraded power. Even though the relation between the laser diode current and the average laser power can be approximated linearly over a wide current range, the results will be presented in relation to the measured maximum process temperature. In doing so, all variation due to the power loss as well the influence of varying process parameters are considered in the results.

4.1.2 Setup for the Laser Treatment of $\mu\text{-Si:H}$

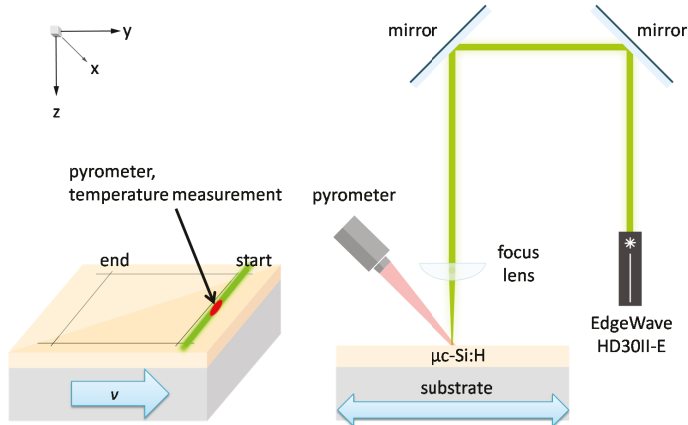


Figure 4.5: Sketch of the experimental setup for the treatment of $\mu\text{-Si:H}$. The line shaped laser beam is focused in y-direction on the sample. The substrate is mounted on an electrical translation stage that moves the sample in y-direction under the focus of the laser beam.

For the treatment of $\mu\text{-Si:H}$, the experimental setup of the Edgewave HD30II-E Innoslab laser was modified. Here, the line shaped laser beam was focused in the y-direction (see section 4.1, Fig. 4.1) on a substrate to increase the power density. This substrate was moved with an electrical translation stage in the focus of the laser beam. Analogous to the treatment of a-Si:H, the laser beam size in x-direction was subject to the beam divergence. The principle of the beam

path is illustrated in Figure 4.5. Again, the process temperature was monitored with a pyrometer.

Due to the modified setup for the treatment of $\mu\text{c-Si:H}$, it was not possible to measure the laser power at the substrate position without further optical devices, as the diverged laser beam was too large in the x-direction. Additional optical elements would lead to a significantly increased uncertainty in the measured power compared to the measurement directly after the laser aperture. Based on this, the experimental results for the treatment of $\mu\text{c-Si:H}$ with $\lambda = 532 \text{ nm}$ are referenced to either the laser diode current or the measured process temperature. The dependency of the average laser power measured directly behind the laser aperture on the laser diode current, is plotted in Fig. 4.6.

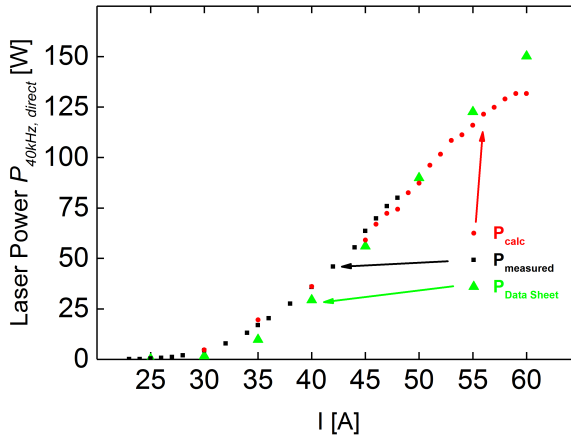


Figure 4.6: Average laser power depending on the laser diode current for a repetition rate of $\nu = 40 \text{ kHz}$. Green triangles refer to the laser power as annotated in the data sheet. The black squares result from direct measurement, while the red dots are calculated from a measurement after reflection on a glass window.

As a consequence of the high intensity of the focused line shaped laser beam and the fact that the size in x-direction exceeds the sensor size of the beam profile camera, the beam profile could not be analyzed for the scanned treatment of $\mu\text{c-Si:H}$.

4.2 355 nm (uv) Short Pulse Laser Source

As ultraviolet (uv) laser source at a wavelength of 355 nm a ROFIN Powerline RSY 20 E / THG laser was used to scribe the electrical isolation lines and for the treatment of $\mu\text{c-Si:H}$. The pulse duration depends on both the repetition rate and the applied current. For reasons of optical stability, this laser is operated at a fixed current ($I = 29 \text{ A}$) and repetition rate ($\nu = 15 \text{ kHz}$), resulting in a pulse duration of approximately $\tau_{\text{pulse}} = 6 \text{ ns}$. The laser power on the sample can be reduced with a motorized polarizer and a Glen-Taylor prism. In doing so, the laser output power can be varied between 20 mW and 800 mW. In addition, the intensity can be further reduced by placing the samples off-focus, as done for the treatment of $\mu\text{c-Si:H}$. This laser source should have a gaussian beam shape and exhibits a spot diameter of $d_{\text{spot}} = 30 \mu\text{m}$. The beam profile is illustrated in Fig. 4.7 with false colors.

As this laser source is integrated into a commercial laser patterning system, no specific setup or system modification could be applied.

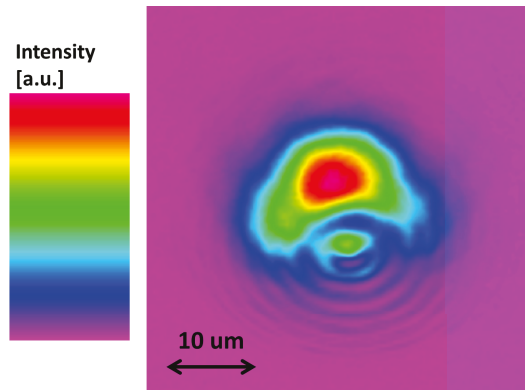


Figure 4.7: False color beam profile of the ROFIN Powerline RSY 20 E / THG laser in focus position.

Part II

Results and Discussions

5 Temperature Measurements

The systems and methods used for the temperature measurements in this work are described in this chapter. Moreover, the method for the calibration of the pyrometers is explained in Section 5.1.1. The determination of the temperature dependent correction functions for a-Si:H and μ c-Si:H are presented in Section 5.2 and Section 5.3, respectively.

5.1 Pyrometers

In order to measure the temperature development during the laser treatment of a-Si:H, a LumaSense™ IMPAC IN 5/5 plus pyrometer (IN 5/5) was used. This pyrometer has a measurement range from 100 °C to 1300 °C and a spectral range centered at 5.14 μ m. The spot size diameter is 2.5 mm in focal distance of 100 mm. Due to a defect of the IMPAC IN 5/5 plus pyrometer, an IMPAC IPE 140 MB 12 pyrometer (IPE 140) was used for the laser treatment of μ c-Si:H. The measurement range of the IPE 140 ranges from 75 °C to 1200 °C, while the spectral range is centered at 3.9 μ m. The measurement spot diameter of this pyrometer is 2.3 mm at a distance of 345 mm.

5.1.1 Calibration Setup

Most materials do not hold the emissivity of a black or gray body. Instead, the emissivity is temperature dependent. As the pyrometers used in this thesis work with a constant emissivity, the measured temperature has to be corrected for all temperature values with deviating emissivity. Therefore, a temperature dependent correction factor f_{corr} is introduced. In order to determine the real sample temperature and the corresponding pyrometer temperature, the sample temperature was measured simultaneously with a thermoelement and the dedicated pyrometer. This setup is sketched in Figure 5.1.

The sample is placed on a high power heating plate reaching temperatures above $T = 600$ °C. To receive the reference surface temperature T_{TE} , a thermoelement is attached to the sample surface with silver paint conductive adhesive (Fig. 5.1). For the positioning of the pyrometer two issues have to be respected. First, the pyrometer should not be aligned perpendicular to the sample surface,

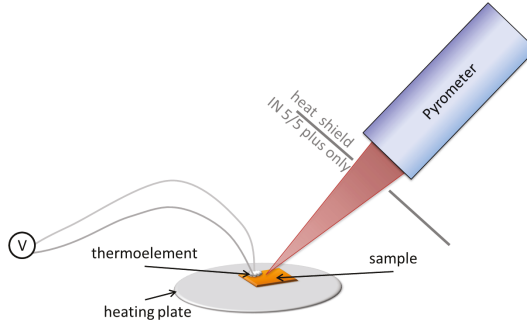


Figure 5.1: Sketch of the experimental setup for the determination of the temperature correction function and the temperature dependent specific emissivity of a-Si:H.

favoring the setup during the laser treatment. Second, the pyrometer measurement spot must not coincide with the thermoelement or the silver paint or exceed the sample surface.

The focusing and the positioning of the measurement spot is eased by a pilot laser included in both pyrometers. As the focal length of the IN 5/5 pyrometer is only $f = 100$ mm, an additional heat protection shield was installed between the heating plate and the pyrometer to prevent the heating of the pyrometer during the measurements. Due to the longer focal length, this is not necessary for the INP 140. The signals from the pyrometer and the thermoelement are logged during heating and cooling of the sample.

In order to qualify the analogous output of the pyrometers, the temperature was logged simultaneously for both the analogous output and the thermoelement with a National Instruments NI USB 6000™ data logger. The correction factor is calculated using the relation of the temperature indicated by the pyrometer $T_{\text{pyro, meas}}$ and the temperature measured in contact with the thermoelement T_{TE} . The temperature output value of the pyrometer is calculated according to the manufacturers directive. Glass cools down more slowly than the CrNi thermoelement that is attached to the surface with silver paint conductive adhesive. Therefore, values obtained during heating were used for the determination of the correction function.

Various methods were tested to determine a fitting function with good results over a large temperature range. They were analyzed regarding the resulting temperature difference. The temperature difference ΔT between T_{TE} and the calculated pyrometer temperature T_{corr} is used to qualify the fit function for f_{corr} .

This temperature dependent correction factor $f_{\text{corr}}(T)$ is defined as

$$f_{\text{corr}}(T) = \frac{T_{\text{TE}}}{T_{\text{pyro, meas}}} \quad (5.1)$$

Based on f_{corr} , the corrected pyrometer temperature is calculated using

$$T_{\text{corr}} = T_{\text{pyro, meas}} f_{\text{corr}} \quad (5.2)$$

5.2 Pyrometer Temperature Correction for a-Si:H

In this section, the correction function for the temperature measurements during the treatment of a-Si:H on glass substrates is presented. The emissivity of the IN 5/5 plus was set to a fixed value and was not modified during the experiments. The pyrometer used for the temperature measurement during the treatment of a-Si:H is not suited for temperatures below 100 °C. In addition, the temperature output of the pyrometer is too high compared with the thermoelement. Therefore all values below $T_{\text{TE, min}} = 100$ °C can be neglected for the fitting. The correction factor for a-Si:H on glass decreases with increasing temperature and converges to $f_{\text{corr}} = 0.85$ (Fig. 5.2 a).

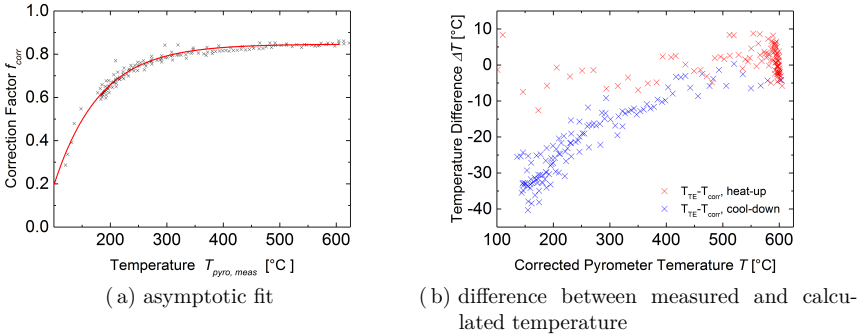


Figure 5.2: (a) Calculated correction factor (black crosses) and corresponding asymptotic fit (red curve) for the determination of a correction function for the determination of the temperature. (b) Temperature difference between the temperature measured with the thermoelement and the pyrometer after application of the correction function. Red crosses refer to the heat-up while the blue crosses refer to the cool-down.

In case of a-Si:H on glass, an asymptotic fit function was used to calculate the temperature dependent correction factor. This function is shown with the red solid line in Figure 5.2 a). The correction function used for a-Si:H with analogous output is defined as:

$$f_{\text{corr}} = \frac{1}{1.17 + 2.11 \cdot 0.987^{T_{\text{pyro}}/^\circ\text{C}}} \quad (5.3)$$

The temperature difference ΔT between T_{TE} and the calculated pyrometer temperature T_{corr} versus the T_{TE} is shown in Figure 5.2 b).

$$\Delta T = T_{\text{TE}} - T_{\text{corr}} \quad (5.4)$$

Again, the red crosses refer to the values retrieved during the heating, while the blue crosses refer to the values obtained during the cooling down, respectively. It can be seen that the calculated temperature is higher than the temperature measured in contact during the cooling down period. This can be traced back to the higher heat conductivity of silver compared to glass or a-Si:H and emphasizes using only the heating period to determine the correction factor.

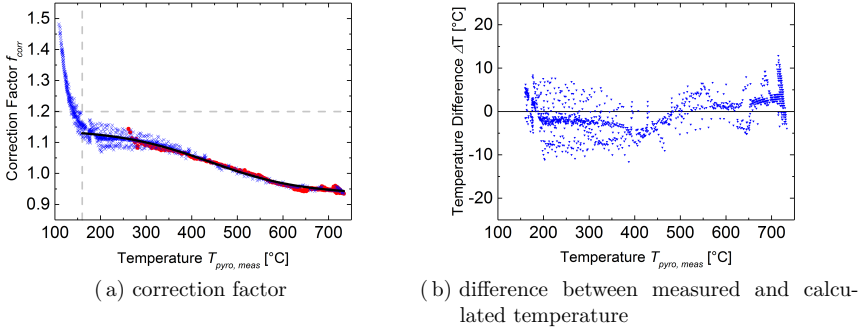


Figure 5.3: (a) Calculated correction factor for the INP 140 pyrometer for the temperature measurement of $\mu\text{c-Si:H}$ on c-Si substrates. The values retrieved from the heating period are plotted in red, while the values obtained during cooling down are plotted in blue, respectively. (b) presents the temperature difference of the thermoelement temperature and the calculated pyrometer temperature resulting of a Boltzmann fit (blue down triangles).

5.3 Pyrometer Temperature Correction for $\mu\text{c-Si:H}$

In this section the correction function for the temperature measurements during the treatment of $\mu\text{c-Si:H}$ on c-Si wafers is presented. The emissivity of the IPE 140 was set to a fixed value $\epsilon = 0.51$ and was not modified during the experiments.

In order to qualify the quality of the correction method, the temperature difference between the thermoelement and the pyrometer was analyzed (Fig. 5.3 b). The function that was chosen for the calculation of the temperature dependent correction factor is plotted with the black solid line in Figure 5.3 a). Due to the strong increase of the correction factor for $T \leq 160$ °C, the fit was applied to $T \geq 160$ °C with corresponding correction factors of $f_{\text{corr}} \leq 1.2$. These limits are indicated with the dashed grey lines in Figure 5.3 a).

Here, T_{pyro} is the temperature retrieved from the INP 140 at an emissivity of $\epsilon = 0.51$. The temperature difference resulting from the use of a Boltzmann function to calculate the temperature dependent correction factor is shown with blue down triangles in Figure 5.3 b). Here, the temperature difference does neither decrease or increase considerably for low or high temperatures. Consequently, this Boltzmann fit can be used to calculate the corrected temperature for the experiments with $\mu\text{c-Si:H}$ on glass.

The function to calculate the correction factor f_{boltz} is defined as

$$f_{\text{boltz}} = 0.935 + \frac{0.195}{1 + \exp((T_{\text{pyro}} - 462)/75 \text{ °C})} \quad (5.5)$$

6 Development of a Method for the Structural Characterization of a-Si:H

Amorphous thin-film solar cells make use of glass as substrate material [115]. The hydrogen concentration c_H and the microstructure parameter R^{IR} of a-Si:H are typically measured by Fourier Transform Infrared Spectroscopy (FTIR) [105, 107, 116]. Standard FTIR measurements involve the use of infrared transparent substrates (e.g. crystalline silicon), as these measurements are performed in transmission.

In this thesis, the amorphous silicon layer was treated with a laser process after deposition. Hereby, thermal annealing was evoked through the absorption of the laser radiation. However, the thermal conductivity of c-Si is two orders of magnitude larger than of Corning Eagle XG substrates, as used in this work. As a consequence, the heat development and dissipation due to the absorption of laser radiation are not competitive on these two substrates. Consequently, c-Si wafers can not be used as substrates for analysis to qualify the influence of the laser treatment on c_H and R^{IR} of a-Si:H. Due to the necessity of using glass substrates, standard FTIR measurements can not be used here. As the modes used to determine c_H and R^{IR} are as well FTIR as Raman active [104, 117, 118], Raman spectroscopy is potentially qualified as a method to determine the hydrogen concentration in this work.

6.1 Analysis of a-Si:H using Raman Spectroscopy

One of the aims in this work is to develop a non-destructive and fast method to improve the understanding of hydrogen in a-Si:H by improving the substrate independent measurement of the hydrogen concentration and enabling a depth-dependent analysis. Typically, the hydrogen concentration is either analyzed by effusion, SIMS or FTIR. Here, different Raman excitation wavelengths are used to gain information about the depth profile of the hydrogen concentration.

In addition, Raman spectroscopy is evaluated as a mean to measure the microstructure parameter. In general, either FTIR or Raman was used in literature

to determine the average hydrogen concentration or to obtain information about the average microstructure [99, 119–121].

The Si-H vibrational modes centred at 640 cm^{-1} (wagging mode) and the vibrational modes between 2000 cm^{-1} and 2100 cm^{-1} (stretching modes) are both infrared and Raman active [120, 122]. Raman spectroscopy is already used for in-situ growth analysis of microcrystalline silicon [99, 120]. Recently, Volodin and Koshelev presented both Raman spectroscopy as well as FTIR absorption data on a wide series of as-deposited a-Si:H films. They determined the concentration of bonds with stretching vibrations at 2000 cm^{-1} and 2100 cm^{-1} with both methods. Using the approach developed by Langford [123] the microstructure parameter for FTIR R^{IR} and Raman R^{Ram} was determined here for the values of the hydrogen concentration published by Volodin [118]. The comparison of both microstructure parameters demonstrates that both methods lead to similar results (Fig. 6.1), emphasizing the usefulness of further investigations to compare those methods.

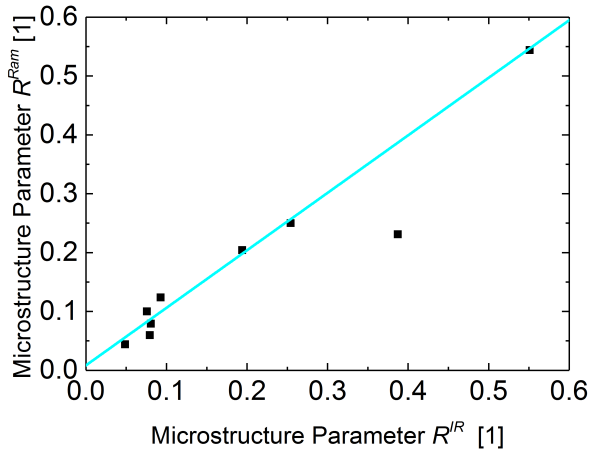


Figure 6.1: Calculated microstructure parameter for FTIR and Raman data obtained from the work of Volodin [118] (black squares). The linear fit of all data points is plotted with the light blue line.

In this work, a comparison of Raman and FTIR as methods for measuring the bulk hydrogen concentration and microstructure as well as the depth dependent hydrogen concentration and microstructure of furnace annealed a-Si:H thin films

on c-Si substrates is made. The results of the depth dependent hydrogen concentration obtained with Raman are compared with SIMS measurements. For easier reading R^{IR} is used for the microstructure determined with FTIR, while R^{Ram} refers to Raman spectroscopy.

6.2 Raman Spectra and Fitting

In this thesis, two different Raman setups were used. One reason for that is to qualify the measurements at equal excitation wavelength and the second was due to the availability of different wavelengths on the individual systems. The analysis of the data followed similar procedures for all systems and wavelengths.

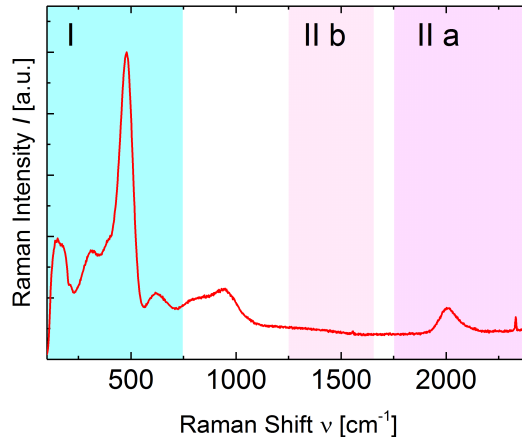


Figure 6.2: Raman spectrum of a-Si:H for the full spectral range detectable with a Renishaw spectrometer. Three different regions I, II a, and II b are highlighted.

In Figure 6.2 an example Raman spectrum of a-Si:H is presented. For this example spectrum, a Renishaw Raman Microscope with a spectral range from $\nu = 100 \text{ cm}^{-1}$ to $\nu = 2400 \text{ cm}^{-1}$ was used. Here, the spectrum was divided into three regions of interest for the analysis (I, IIa, and IIb). This is useful for two reasons. First, one of the systems provides multiple spectra over the whole wavelength range analyzed. Second, each of these chosen ranges contains at least one vibrational mode analyzed in this work and a peak for normalization.

Region I) includes the Si-Si modes, that are needed to find whether the material is crystalline, micro-crystalline or amorphous. In addition, the Si-H wagging mode at 640 cm^{-1} is situated in that region (Fig. 6.3 a).

The region IIa) exhibits the Si-H doublet, while IIb) exhibits the Si-D doublet, respectively. The regions IIa) and IIb) can be used to determine the R^{Ram} , c_H or the deuterium concentration, respectively. The Raman modes of interest for this thesis are listed in Table 6.1. Please note that the modes marked with * were first correlated with Si-H_n and Si-D_n (here n> 1) bondings. However, Beyer and Wagner found that the Si-H mode centered at 2100 cm^{-1} is attributed to hydrogen bonds at (inner) surfaces. The same attribution should be made for deuterium at surfaces [57]. The position of the modes in the spectra are indicated in Fig. 6.3 a) for region I), and in Fig. 6.3 b) for region IIa) and IIb), respectively.

Table 6.1: Raman modes used in this work for the analysis of a-Si:H (a-Si:D) and $\mu\text{c-Si:H}$. (* historical assignment)

| wavenumber [cm^{-1}] | mode | references |
|---------------------------------|--|------------------------------|
| 140 | TA phonon | [103] |
| 314 | LA phonon | [103] |
| 390 | LO phonon | [103] |
| 480 | TO phonon (a-Si) | [103, 107, 122] |
| 520 | TO phonon (c-Si) | [107] |
| 610-620 | 2 LA | [103, 107, 124, 125] |
| 640 | Si-H _n wagging | [17, 75, 104, 105, 117, 126] |
| 1454-1473 | Si-D stretching | [103, 104, 122, 127] |
| 1510 | Si-D ₂ stretching * | [107] |
| 1550 | O ₂ (air) | [104] |
| 1990-2010 | Si-H | [103–105, 120, 122] |
| 2080-2000 | Si-H ₂ +Si-H ₃ * | [104, 105, 120] |
| 2330 | N ₂ (air) | [128] |

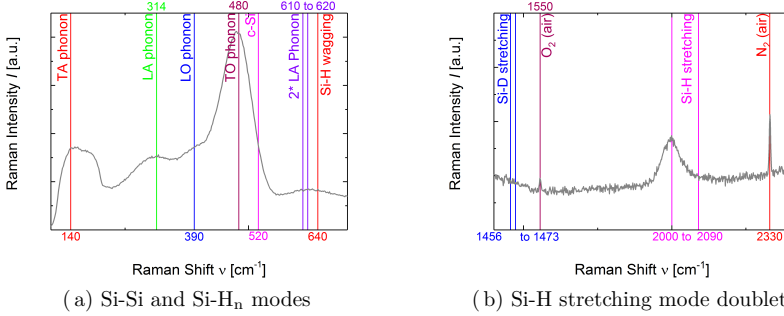


Figure 6.3: Raman modes for the analysis of a) the crystallinity and the c_H using the Si-H wagging modes and b) for the determination of c_H (c_D) with the Si-H (Si-D) stretching modes.

Raman Crystallinity In order to qualify whether the material is amorphous, micro-crystalline or crystalline the wavenumbers of the spectrum ranging from 400 cm^{-1} to 700 cm^{-1} are analyzed. The Raman crystallinity is defined as

$$X_c = \frac{I_c}{I_c + I_a} \quad (6.1)$$

where I_c is the integrated intensity of the Raman signal arising from the crystalline phase and I_a from the amorphous phase, respectively. After normalization to the maximum the baseline is subtracted. Hereby it is assumed that the Raman intensity is zero for both 400 cm^{-1} and 560 cm^{-1} . As there are no Raman active modes in c-Si between 400 cm^{-1} and 450 cm^{-1} , the amorphous fraction must satisfy the Raman intensity in that region. A detailed description of the determination of X_c can be found in [18]. As an example, the Raman spectrum of $\mu\text{c-Si:H}$ with a Raman crystallinity of $X_c = 55.9$ is shown in Figure 6.4. The modes contributing to the Raman intensity in this area of interest are presented in Figure 6.3 a).

Si-H Wagging Mode All Si-H_n (here: $n = 1, 2, 3$) bondings have a wagging mode centered at 640 cm^{-1} . Therefore, it is convenient to use this wagging mode for the determination of the hydrogen concentration. However, the overtone of the Si-Si longitudinal acoustic (LA) phonon mode is situated nearby, and the signal of this wagging mode is weak. As a result, the distinct separation of the Si-H_n wagging mode is difficult. Both modes are indicated in Figure 6.3 a).

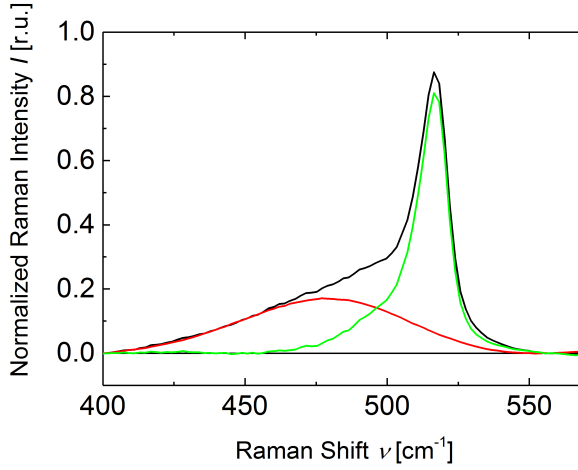


Figure 6.4: Spectrum of $\mu\text{c-Si:H}$ (black) with its amorphous fraction (red) and the crystalline fraction (green) for the wavenumber range from 400 cm^{-1} to 700 cm^{-1} which is analyzed for the determination of the crystalline volume fraction X_c .

Other Modes Other modes contributing to the signal intensity in I) are the transverse acoustic (TA) mode at 140 cm^{-1} , the longitudinal acoustic (LA) mode centered at 314 cm^{-1} , the longitudinal optical phonon (LO) mode at 390 cm^{-1} and the TO phonon mode of *c*-Si at 520 cm^{-1} . All modes contributing to the Raman intensity in this area of interest are presented in Figure 6.3 a) and Table 6.1.

Si-H Doublet (Region IIa) For the determination of the microstructure parameter and the determination of the hydrogen concentration, the Raman shift between 1800 cm^{-1} and 2400 cm^{-1} was extracted. Here, the stretching modes centered at 2000 cm^{-1} and 2100 cm^{-1} are analyzed. All modes contributing to the Raman intensity in this area of interest are presented in Figure 6.3 b). First, the spectrum was normalized to the N_2 peak at $\nu = 2330\text{ cm}^{-1}$ (see Table 6.1). After that, the baseline was subtracted. In order to gain information about the amount of hydrogen and the hydrogen bonding, two individual Gaussian functions were fitted into the Si-H stretching mode doublet, one for each mode. The constraints for the fitting are listed in Table 6.2. For the determination of c_{H} , the sum of the integrated area of the two Gaussian functions was used.

Table 6.2: Parameters and bounds used for the fitting of the two Gaussian peaks in order to determine c_H and R^{Ram}

| parameter | lower limit | upper limit |
|---------------|-----------------------|-----------------------|
| center peak 1 | 1980 cm^{-1} | 2030 cm^{-1} |
| center peak 2 | 2070 cm^{-1} | 2110 cm^{-1} |
| width peak 1 | 20 cm^{-1} | 100 cm^{-1} |
| width peak 2 | 20 cm^{-1} | 120 cm^{-1} |

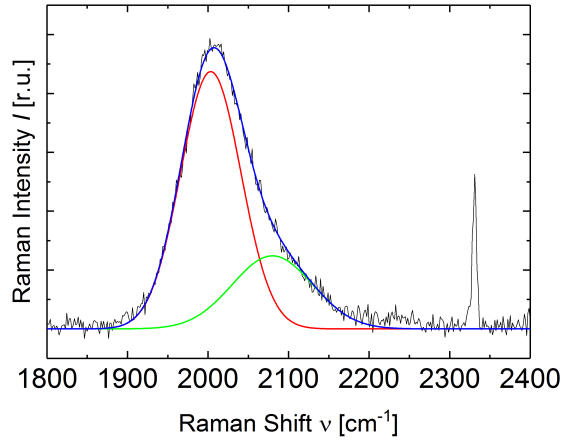


Figure 6.5: Raman spectrum (black) of the 2000 cm^{-1} and 2100 cm^{-1} doublet after normalization and baseline subtraction. The Gaussian fits are printed in red for 2000 cm^{-1} and green for 2100 cm^{-1} , respectively. The resulting curve fit is shown in blue.

Considering the microstructure parameter, the relation of the two peaks was calculated with

$$R^{Ram} = \frac{I_{2100}}{I_{2100} + I_{2000}} \quad (6.2)$$

whereas I_{2100} is the integrated intensity of the Gaussian centered at 2100 cm^{-1} and I_{2000} of the Gaussian function centered at 2000 cm^{-1} , respectively. As an example, fitted curves after normalization and baseline subtraction are presented in Fig. 6.5.

6.3 Sample Fabrication and Measurement

6.3.1 Sample Fabrication

In this work, an a-Si:H thin-film with a thickness of 0.8 μm was deposited on a 4 inch crystalline silicon wafer using a 100 nm thick SiO_x interlayer to avoid blistering and lift-off of the amorphous silicon layer [101]. The a-Si:H film was grown by PECVD at a pressure of $p = 0.66$ mbar, a gas flow of 10 sccm silane (SiH_4), 10 sccm hydrogen and an rf power (13.56 MHz) of $P_{\text{rf}} = 10$ W. As a result, an a-Si:H layer with $c_{\text{H}} = 14$ at.% is obtained. After deposition, the samples were annealed in an ultra high vacuum oven with annealing temperatures ranging from $200\text{ }^\circ\text{C} \leq T \leq 575\text{ }^\circ\text{C}$. Heating and cooling was performed at high rates of 40 K/min with an annealing time of five minutes at the dedicated temperature.

6.3.2 FTIR Reference Measurements

The FTIR measurements were carried out in transmission with a ThermoElectron Nicolet 5700. A detailed description of FTIR spectroscopy is found in Chapter 3, Section 3.3.2.

The stretching modes centered at 2000 cm^{-1} and 2100 cm^{-1} are subject to interferences due to the SiO_x interlayer for the FTIR absorption. As a consequence, the subtraction of the background is crucial for the determination of the hydrogen concentration and small deviations lead to high scattering. The microstructure parameter however is calculated from the relative signal intensity of the two neighbouring stretching modes. Therefore, the setting of the baseline does not have the same impact on the calculation of the microstructure parameter, as for the calculation of the hydrogen concentration. Accordingly, the 640 cm^{-1} wagging mode was used to determine the hydrogen concentration using FTIR as no interferences were observed in this wavenumber region. In addition, the 2000 cm^{-1} and 2100 cm^{-1} stretching modes were evaluated to calculate the microstructure parameter R^{IR} .

6.3.3 Raman Signal Analysis

Raman spectroscopy was performed in backscattering mode for all excitation wavelengths. In order to estimate the Raman information depth, the absorption of the a-Si:H used in this work was measured. The as-deposited a-Si:H exhibits an absorption coefficient of $\alpha_{488} = 1.73 \times 10^5\text{ cm}^{-1}$ for a wavelength of $\lambda = 488$ nm and of $\alpha_{532} = 1.11 \times 10^5\text{ cm}^{-1}$ for $\lambda = 532$ nm, respectively. Taken into account, that the information depth of Raman in backscattering mode is half of the optical penetration depth $1/\alpha$, the information depths are $d_{488} = 29$ nm and $d_{532} = 45$ nm,

respectively. By choosing a Kr-Ion Laser, with an excitation wavelength of $\lambda = 647$ nm, the information depth is calculated with $d_{647} = 618$ nm. Consequently, a more detailed and exhaustive depth dependent hydrogen concentration mapping would be obtained, facilitating the comparison with FTIR. However, the use of a laser with an excitation wavelength of $\lambda = 647$ nm, lead to several problems. First, the stretching modes centered at 2000 cm^{-1} and 2100 cm^{-1} were superposed with an interference. Consequently the setting of the baseline is not straight forward. Indeed, the use of optical simulation software would be required for precise analysis. Next, the signal to noise ratio was too low for peak-fitting even for measuring times of 90 minutes. As this is in contradiction to a fast and straight forward analysis, the excitation wavelength of $\lambda = 647$ nm was not applied in this work.

Si-H Stretching and Wagging Mode Selection The Raman intensity of the Si-H_n wagging mode centred at $\nu = 640\text{ cm}^{-1}$ is weaker than the stretching modes centred at 2000 cm^{-1} and 2100 cm^{-1} . In addition, it is difficult to separate the longitudinal acoustic overtone (2 LA) at 610 cm^{-1} to 620 cm^{-1} of a-Si from the Si-H_n wagging mode centred at $\nu = 640\text{ cm}^{-1}$ [103, 107, 129]. Therefore, the sum of the Raman intensity of the stretching modes at 2000 cm^{-1} and 2100 cm^{-1} was used to determine the hydrogen concentration with Raman spectroscopy. As an example, the Raman spectra of samples with different hydrogen concentration are presented in Figure 6.6. These spectra were measured at $\lambda = 532$ nm and obtained from samples annealed at temperatures $200\text{ }^{\circ}\text{C} \leq T \leq 575\text{ }^{\circ}\text{C}$. The decrease of the Raman shift intensity with increasing annealing temperature is indicated with the arrow.

Hydrogen Concentration The hydrogen concentration is proportional to the sum of the intensity of the stretching modes centered at 2000 cm^{-1} and 2100 cm^{-1} according to

$$c_{\text{H}} \propto \int (I_{2000} + I_{2100}) d\nu \quad (6.3)$$

where ν is the wavenumber, and $I_{2000} + I_{2100}$ is the intensity of the sum of the Raman peaks of 2000 cm^{-1} and 2100 cm^{-1} . In addition, these stretching modes are also used to determine the Raman microstructure parameter R^{Ram} . In order to eliminate changes in signal strength due to changes in reflectivity, the Raman spectra have been normalized. The Raman signal around 2000 cm^{-1} composes of the two individual stretching modes at 2000 cm^{-1} and 2100 cm^{-1} . Two Gaussian functions with peak positions centered at the two individual stretching modes are fitted to match the Raman intensity. For normalization, the signal can

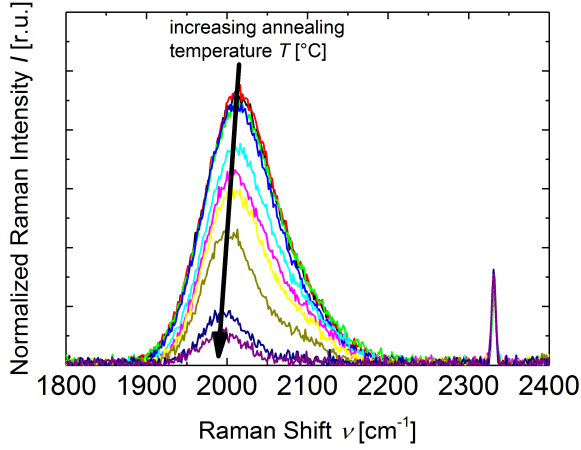


Figure 6.6: Raman spectra of the stretching modes centered at 2000 cm^{-1} and 2100 cm^{-1} for the excitation with $\lambda = 532\text{ nm}$. The decrease of the normalized Raman intensity with increasing annealing temperature is indicated with the black arrow.

normalized to the maximum around 2000 cm^{-1} , imitating the method used for the peak centered at 640 cm^{-1} .

Microstructure Parameter The microstructure parameter is derived for both FTIR and Raman measurements in the same way. The Raman microstructure parameter is calculated from Raman measurements, imitating the method generally used to determine R^{IR} [99, 102]. The microstructure parameter is calculated with

$$R^{IR,Ram} = \int \frac{I_{2100}}{(I_{2000} + I_{2100})} \quad (6.4)$$

where I_{2100} and I_{2000} are the intensities at wavenumbers 2000 cm^{-1} and 2100 cm^{-1} of the FTIR absorption or the Raman intensity, respectively.

SIMS Measurements For comparison of the depth dependent hydrogen concentration and microstructure, SIMS measurements were carried out using a Time of Flight (ToF) SIMS (ION-TOF). Cesium was used as primary ion source. The sputtered area has a size of $300 \times 300\text{ }\mu\text{m}^2$ and was sputtered at a dose of

1.66×10^{18} Ions/cm². For analysis Bi₃ was used with a dose of 5.35×10^{14} Ions/cm². Here, the relation of the signals of mass 31 and mass 30 were analyzed. This resembles the intensity of Si-H/Si. The sputter time is equalized with the depth of the a-Si:H layer.

6.3.4 Depth-Dependent Hydrogen Concentration

Figure 6.7 shows the hydrogen concentration depending on the annealing temperature T for both FTIR and Raman analysis. As can be seen in Figure 6.7, the determined hydrogen concentration decreases with increasing annealing temperature T for both Raman excitation wavelengths (stars) used in this work and FTIR (squares). For all samples, the as-deposited reference is plotted at the deposition substrate temperature $T_{\text{sub}} = 180$ °C. The hydrogen concentration was normalized to the as-deposited reference for all analysis methods.

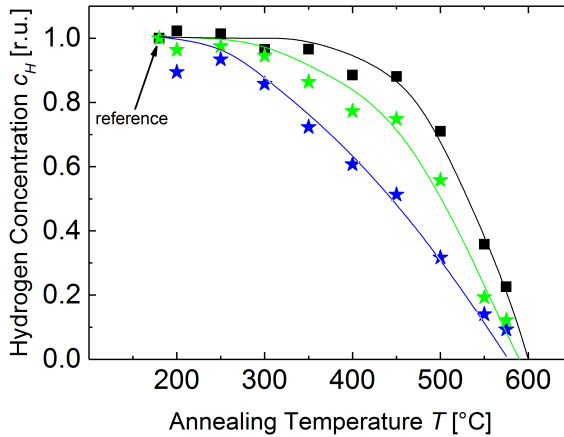


Figure 6.7: Relative reduction of c_H with increasing annealing temperature. The hydrogen concentration is derived from the integrated peak area of the FTIR modes centred at 640 cm^{-1} (black squares). The corresponding c_H obtained from the Raman modes centred at 2000 cm^{-1} and 2100 cm^{-1} is shown in green stars for excitation with 532 nm and blue stars for excitation with 488 nm . The solid lines are guides for the eye.

The hydrogen concentration derived from Raman spectra with an excitation wavelength of $\lambda = 488 \text{ nm}$ is shown with blue stars, while those for the excitation with $\lambda = 532 \text{ nm}$ are illustrated with green stars. The FTIR measurements

show a strong decrease in the hydrogen concentration starting at temperatures $T > 450$ °C. In contrast, the Raman measurements exhibit an onset of hydrogen loss already at much lower temperatures. The corresponding SIMS depth profiles for annealing temperatures of $T = 200$ °C, $T = 400$ °C, $T = 500$ °C, and $T = 575$ °C are presented in Figure 6.8.

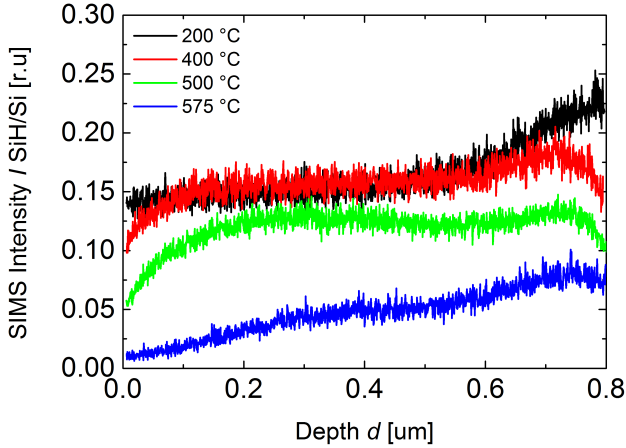


Figure 6.8: SIMS depth profiles of the relative Si-H bonding concentration for annealing temperatures 200 °C $\leq T \leq 575$ °C.

According to former works, the surface as well as the a-Si/substrate interface should work as diffusion sinks [62, 130–133] with a uniform distribution of c_H throughout the a-Si:H layer for the as-deposited reference. However, the SIMS depth profiles show a significant increase of c_H towards the a-Si:H/SiO_x interface for the sample annealed with $T = 200$ °C (Fig. 6.8). As a consequence, the measured hydrogen concentration is higher for all annealing temperatures close to the interlayer interface than to the external surface. The depletion of hydrogen close to the surface is also detected when comparing the hydrogen concentration obtained by FTIR and Raman with different excitation wavelengths. As shown in Figure 6.7, FTIR analysis results in the highest measured hydrogen concentration (black squares), while the Raman measurements with the shortest penetration depth (blue stars) exhibit the smallest hydrogen concentration.

The SIMS results show (Fig. 6.8) that the as-deposited sample has an initial hydrogen enrichment towards the SiH/SiO_x interface instead of the expected symmetrical concentration throughout the whole a-Si:H layer. The investigating of the monitored deposition parameters revealed pressure instabilities during the

SiO₂ deposition. This leads to the conclusion, that there is no stoichiometric SiO₂ interlayer, but a SiO_x interlayer that influences the growth of a-Si:H. However, this anomaly does neither influence the Raman and FTIR analysis, nor the possibility to compare those methods.

Table 6.3: Comparison of the determined hydrogen concentration c_H for SIMS and optical characterization methods. Here, the hydrogen concentration obtained with Raman and FTIR is normalized to the hydrogen concentration obtained for the annealing at $T = 200$ °C

| | 200 °C | 400 °C | 500 °C | 575 °C |
|-----------|--------|--------|--------|--------|
| SIMS FTIR | 1 | 0.96 | 0.72 | 0.29 |
| FTIR | 1 | 0.89 | 0.71 | 0.23 |
| SIMS 532 | 1 | 0.76 | 0.55 | 0.09 |
| Raman 532 | 1 | 0.77 | 0.56 | 0.12 |
| SIMS 488 | 1 | 0.73 | 0.50 | 0.08 |
| Raman 488 | 1 | 0.68 | 0.35 | 0.10 |

The SIMS hydrogen concentration, as listed in Table 6.3, is calculated for Raman considering the depth dependent signal strength with

$$I = \frac{{}^{30}\text{SiH}}{{}^{30}\text{Si}} \quad (6.5)$$

and

$$c_H = \int_0^d I(x) e^{-2\alpha x} dx \quad (6.6)$$

where I is the relation of the mass signals ${}^{30}\text{SiH}$ to the mass signal ${}^{30}\text{Si}$, x is the calculated depth where the signal is obtained, d the film thickness, and α is the absorption coefficient for the Raman wavelength. The SIMS hydrogen concentration calculated for FTIR is the mean of the valid values. Next, the hydrogen concentration was normalized to 1 for the measurement of the sample annealed at 200 °C for all experiments. When comparing the values obtained for the hydrogen concentration from SIMS integration and Raman or FTIR, it was found that the deviation is rather small especially for FTIR and the Raman measurements at $\lambda = 532$ nm.

Discussion

As presented in the experimental part, c_{H} as determined by Raman spectroscopy is smaller than c_{H} determined by FTIR absorption Figure 6.7. This finding is in agreement with the SIMS depth profile (Tab. 6.3), considering the wavelength dependent absorption of amorphous silicon.

As mentioned above, the determined hydrogen concentration is in agreement for the spectroscopic methods Raman and FTIR, and SIMS. Considering the SIMS profile of the $T = 200$ °C annealed sample (Fig. 6.8) two results can be noted. First, there is no measurable hydrogen diffusion for annealing at $T = 200$ °C, as the SiH/Si intensity does not decrease towards the external surface. Consequently, the measurements of the $T = 200$ °C samples can be used as reference for SIMS. Secondly, it is indicated that the Raman reference for the excitation wavelength of $\lambda = 488$ nm is estimated too high, as the drop of the hydrogen concentration for $T = 200$ °C is not detected in the SIMS profile (Fig. 6.7, Fig. 6.8). A lower hydrogen concentration for the as deposited reference would shift all subsequent hydrogen concentrations to higher values. As a result, the hydrogen concentration retrieved with an excitation wavelength of $\lambda = 488$ nm would approach the values obtained with SIMS.

In summary, SIMS measurements proofed that Raman spectroscopy can be used to perform a depth dependent analysis of the hydrogen concentration of amorphous silicon. However, the determination of the hydrogen concentration of a reference is crucial for Raman analysis. In Figure 6.7 for example, the hydrogen concentration obtained with Raman spectroscopy at 532 nm is higher for samples annealed at $T = 250$ °C than at $T = 200$ °C. This can be an indication for a poorly determined reference hydrogen concentration as an increase of the hydrogen concentration due to thermal treatment is not expected. On the other hand this can also indicate a locally constrained variation of c_{H} that was not detected with FTIR. For the shorter excitation wavelength of $\lambda = 488$ nm, a strong local drop of the hydrogen concentration is found for $T = 200$ °C. This might result either out of a deviation for the reference or an irregularity of the $T = 200$ °C sample that leads to a weaker signal. Here, it has to be taken into account that the measurements for different annealing temperatures cannot be performed at the same sample position. As a consequence, layer inhomogeneities can also lead to evaluation uncertainties. For annealing temperatures below $T = 300$ °C, the diffusion length L_{diff} is in the order of several nm or smaller. Accordingly, the hydrogen concentration does not change markedly for annealing temperatures below $T = 300$ °C.

6.3.5 Depth-Dependent Microstructure Parameter

The derived annealing temperature dependent microstructure parameters, are illustrated in Figure 6.9. All characterization methods show first a decrease of the microstructure parameter to a local minimum. This minimum of the microstructure parameter is followed by an increase, exceeding the initial microstructure parameter. After reaching the maximum, the microstructure parameter decreases again. The FTIR microstructure parameter R^{IR} is maximal at $T = 500$ °C, while the maximum of the Raman microstructure parameters is shifted to lower temperatures. Even though, the evolution is similar for FTIR and both Raman excitation wavelengths, the calculated values for the microstructure parameter are shifted towards higher values for longer excitation wavelengths. Hence, the values derived with Raman at an excitation wavelength of $\lambda = 488$ nm are smallest, while FTIR yields the highest values. Regarding the relative change of the microstructure parameter from the as-deposited sample to the maximum, R^{IR} increases by 69 %, R_{488}^{Ram} by 66 %, and R_{532}^{Ram} by 42 %.

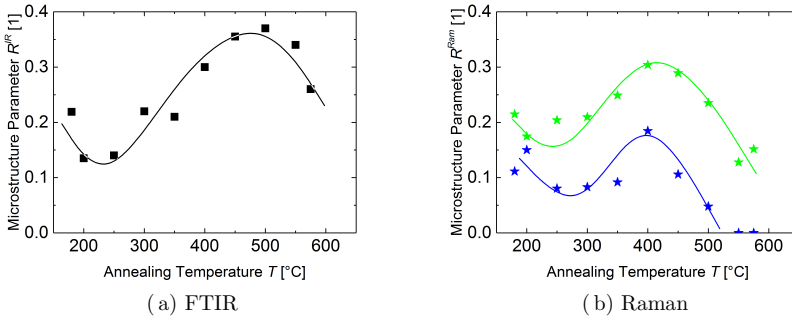


Figure 6.9: Calculated microstructure parameter derived from a) FTIR R^{IR} black squares and b) Raman measurements R^{Ram} . Blue stars denote the Raman microstructure parameter derived from the measurements with an excitation wavelength of 488 nm, while green stars refer to an excitation wavelength of 532 nm. For all samples, the as-deposited reference is plotted at the deposition substrate temperature $T_{sub} = 180$ °C. The solid lines are inserted as guides for the eye.

Discussion

The course of the microstructure parameter, depending on the annealing temperature T is comparable for Raman and FTIR (Fig. 6.9). The increase of

the microstructure parameter with increasing annealing temperature has been explained by an increase in void concentration due to an inhomogeneous densification (shrinkage) of the material [116] that is resulting of the hydrogen out-diffusion. The nature of the decrease of R^{Ram} for annealing temperatures below $T = 350$ °C and above $T = 450$ °C is not yet explained.

As mentioned before, the calculated values of the microstructure parameter are smaller for Raman than for FTIR ($R^{Ram} \leq R^{IR}$). This is in agreement with the hydrogen depletion towards the film surface and with a direct dependence of the microstructure parameter on the hydrogen concentration [116] for the annealed samples. This emphasizes the finding, that the hydrogen concentration c_H changes within the layer and that the microstructure parameter directly depends on the hydrogen concentration for our thermally annealed samples. Moreover, due to the growth properties of amorphous silicon, a variation of the microstructure parameter throughout the thin film is reasonable [17, 124]. Hence, additional information is obtained in using Raman with different optical penetration depths.

Nevertheless, it has to be taken into account that the intensity of the peaks decreases with decreasing hydrogen concentration, leading to a reduced accuracy in the derived hydrogen concentration. With regard to using the microstructure parameter as a figure of merit for potentially good solar cell absorber material [21], the absolute values of the microstructure parameter derived with Raman are not competitive with those obtained with FTIR. Though, the evolution of both methods is competitive. Accordingly, Raman can also be used to qualify if quantity of voids decreases or increases due to a post-deposition treatment.

6.4 Conclusion

Here, a comparison of Raman and FTIR spectroscopy for the evaluation of the hydrogen concentration and the microstructure parameter for a-Si:H thin-films is presented. It could be shown that both methods lead to comparable results regarding the hydrogen concentration of amorphous silicon considering the analyzed depth. Furthermore, the influence of annealing on the microstructure can be qualified with both methods. Although the values of the microstructure parameter are not equal for both methods, the evolution as a function of annealing temperature is comparable. The deviation of the values is partially attributed to the limited penetration depth of Raman spectroscopy, depending on the excitation wavelength.

In contrast, Raman spectroscopy can be used to make a depth selective analysis on the hydrogen concentration c_H and the microstructure R^{Ram} by adapting the excitation wavelength to the depth of interest. Therefore, surface analysis should be feasible by choosing a wavelength in the UV-region that will be absorbed within

the first few nanometers. Further experiments should be performed to investigate whether UV-Raman spectroscopy with a very short penetration depth can be used to qualify the a-Si:H passivation of solar cell concepts with passivated contacts. Raman spectroscopy can be used helping to understand and analyze the growth process of a-Si:H, as depth dependent changes and irregularities can be detected in a thin film at any production stage or even in-situ deposition.

7 Laser Treatment of Amorphous Silicon on Glass Substrates

In this chapter, the influence of a post-deposition laser treatment on device grade a-Si:H is investigated. Therefore, a PECVD grown a-Si:H thin-film is deposited on Corning Eagle XG substrates. After deposition, the amorphous silicon layer is exposed to laser radiation of a short-pulse laser at a wavelength of $\lambda = 532$ nm. Due to the absorption of the laser radiation in the a-Si:H layer, the a-Si:H thin-film is heated up on a short time scale. The influence of this laser treatment on the hydrogen concentration c_H , the photo-response, and the sub-bandgap absorption is studied.

The samples as well as the laser system and the experimental parameters are described in Section 7.1. For a better understanding of the heat transport and temperature evolution due to the laser treatment, 2D heat transfer FEM simulations were carried out. These simulation results are presented in Section 7.2.4. The influence of the laser treatment on a-Si:H is presented in Section 7.2. There, the impact on the hydrogen concentration as well as on electrical and optical properties is shown.

Section 7.3 comprises simulations for a better insight into the experiments. First, the influence of the short laser pulse on the temperature development was investigated and compared to an assumed cw-laser with the same average power (Sec. 7.3.1). In addition, 1D FEM simulations were performed for a better understanding of the hydrogen diffusion during the irradiation. The simulation and experimental results are compared in Section 7.3.2.

In Section 7.4 the results of the experiments and the simulations are recapitulated and discussed.

7.1 Experiments

7.1.1 Sample Fabrication

For this part of the thesis a-Si:H thin-films with a thickness of $d = 0.36$ μm were deposited on 10×10 mm² Corning Eagle XGTM substrates by plasma-enhanced chemical vapour deposition (PECVD). The PECVD was performed at a pressure

of $p = 0.66$ mbar, a gas flow of 10 sccm silane (SiH_4), 10 sccm hydrogen, and a rf power (13.56 MHz) of $P_{\text{rf}} = 10$ W. Using these deposition parameters, an a-Si:H layer with a hydrogen concentration of approximately $c_{\text{H}} = 14$ at.% is obtained. These deposition parameters result in a device-grade material that has been demonstrated as absorber layer without further defect annealing for thin-film solar cells. This amorphous silicon, as used in this work, has an absorption coefficient of $\alpha = 9.45 \times 10^4 \text{ cm}^{-1}$ at $\lambda = 532$ nm. The corresponding optical penetration depth is 106 nm.

7.1.2 Laser Treatment

The post-deposition laser treatment was performed with an Edgewave HD30II-E Innoslab laser at a wavelength of $\lambda = 532$ nm, a pulse duration of $\tau_{\text{pulse}} = 7$ ns, and a repetition rate of $\nu = 40$ kHz. The average laser power applied on the sample ranged from $P = 10$ W to $P = 46$ W. A cylindrical lens and a rectangular aperture were used to form a rectangular laser beam on the sample, resulting in an irradiated area of approximately $5 \times 9 \text{ mm}^2$. The beam profile at the sample surface is similar to a tophat in both directions. The irradiation time was varied between $t = 3$ s and $t = 10$ s. In Section 7.2.4, a corresponding 2D FEM temperature simulation is performed for one chosen laser power and an irradiation time of $t = 10$ s. The laser as well as the setup used for these experiments are described in detail in Chapter 4.1.

During the laser treatment, the sample temperature was monitored with a LumaSense IMPAC IN 5/5 plus pyrometer. The spectral range of the detector of this pyrometer is centered at $5.14 \text{ }\mu\text{m}$. Consequently, the laser wavelength of $\lambda = 532$ nm does not influence the pyrometer measurement. The pilot laser of the pyrometer was used to align the pyrometer measurement area to the area with the maximum temperature during the laser treatment. However, the setup does not allow a perpendicular alignment of the pyrometer to the sample surface. As a consequence, the measurements are performed under an angle smaller than $\alpha = 45^\circ$. Details on the temperature measurement and analysis are described in Chapter 5.

The sampling time of the pyrometer was varied between $t_{\text{samp}} = 40$ ms and $t_{\text{samp}} = 80$ ms. The individual pulses in the order of nanoseconds cannot be resolved with the pyrometer. As a consequence an average temperature is measured over the sampling time. The spot size of $D_{\text{spot}} = 2.5$ mm in focus is larger than the hottest spot on the sample. Thus, the measured temperature is smaller than the highest temperature on the sample. The samples used in this work do not exhibit the behavior of a gray body, instead they feature a temperature dependent emissivity. Therefore, a temperature dependent correction function was used to

calculate the temperature from the radiation intensity (see Cha. 5). It has to be noted that the peak intensity of the laser beam shifts with changing laser diode current. However, the laser output power is subject to fluctuation. Therefore, the temperature measurements undergo certain measurement uncertainties that have to be considered when comparing the results.

7.2 Experimental Results and 2D Heat Transfer Simulation

7.2.1 Time Dependent Process Temperature

Figure 7.1 a) shows as an example the time dependent temperature increase and decrease for a laser treatment time of $t = 3$ s. The average laser power was varied from $P_{\text{avg}} = 11.7$ W (black line) to $P_{\text{avg}} = 24.9$ W (magenta line). Similar results were obtained with an irradiation time t of 4 s, 7 s and 10 s, though the results are not shown here.

The temperature does not reach a steady-state value over the duration of the laser irradiation. A steep increase in temperature over the entire irradiation time was also observed for the other applied irradiation times. The saturation is not even reached for the irradiation time of $t = 10$ s. The black arrow is positioned on the time axis, when the laser is switched off and indicates the increasing applied laser power.

Figure 7.1 b) presents the maximum temperature depending on the laser power for laser treatment time of $t = 3$ s. The graph shows that a linear dependency of the maximum process temperature can be assumed for a wide range of applied laser power.

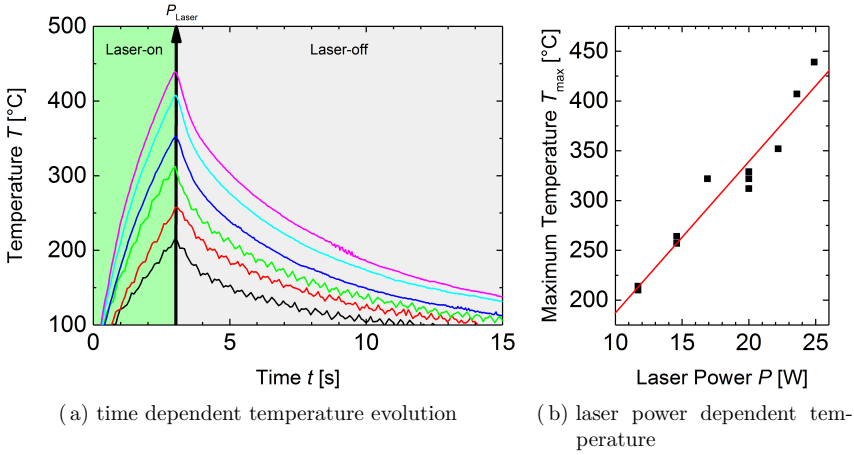


Figure 7.1: a) Time dependent process temperature for a laser treatment time of $t = 3$ s. The average laser power was increased from $P_{\text{avg}} = 11.7$ W (black line) to $P_{\text{avg}} = 24.9$ W (magenta line). The black arrow indicates the increasing maximum temperature with increasing laser power. It is set on the time scale at the laser-off time. b) Maximum temperature depending on the laser power for a laser treatment time of 3 s (black squares). The red line refers to a linear fit for the measured values.

7.2.2 Hydrogen Concentration

The hydrogen concentration was determined following the procedure as described in Chapter 6. The results presented in this section were obtained using a Renishaw Raman spectrometer with an excitation wavelength of $\lambda = 532$ nm. Figure 7.2 shows the relative hydrogen concentration depending on the maximum process temperature T_{max} . The colors used in this figure indicate the irradiation times of the experiment (green 3 s, blue 4 s, red 7 s, violet 10 s).

Figure 7.2 indicates that the hydrogen concentration is primarily dependent on the maximum process temperature T_{max} . The hydrogen concentration decreases steadily with increasing T_{max} . For temperatures above $T_{\text{max}} = 600$ °C, the hydrogen concentration is below the detection limit of the Raman spectroscopy systems used for this work. It is noticeable that c_{H} seems to decrease already for maximum temperatures below $T_{\text{max}} = 300$ °C, despite the scatter in the data. Figure 7.2 reveals that the scattering between the individual samples is higher than the

impact of the irradiation times applied in this work. This is also consent with the theory of diffusion, where the impact of the temperature is higher than the impact of time. Therefore, T_{\max} can be used as a reference value to compare the individually treated samples.

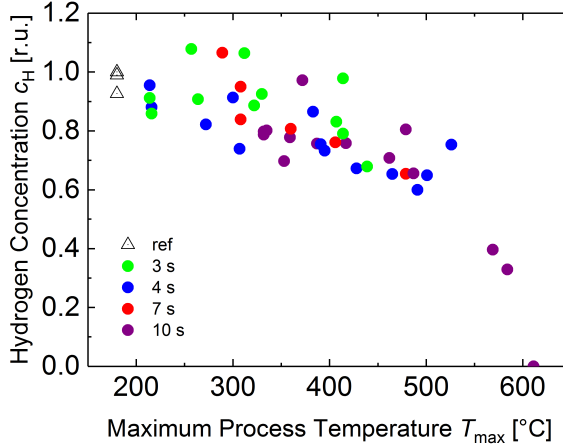


Figure 7.2: Relative change of c_H depending on the maximum temperature due to laser treatment. The as-deposited references are illustrated in open triangles. The colors refer to the exposure time (green 3 s, blue 4 s, red 7 s, violet 10 s).

7.2.3 Electrical and Optical Properties

Electrical Properties Due to the laser treatment in ambient atmosphere impurities, as for example oxygen, could diffuse into the a-Si:H layer. Therefore, photo- and dark conductivity measurements were performed in order to qualify the influence of the laser treatment on the quantity and the type of impurities.

The influence of the laser treatment on the photo- and dark conductivity and the resulting photoresponse was investigated for selected samples covering a temperature range for maximum process temperatures reaching from $T_{\max} = 264$ °C to $T_{\max} = 655$ °C, as well as an as-deposited reference. The photoconductivity (Fig. 7.3 a, right axis, red) is in the same order of magnitude for all analyzed samples. However, a strong increase of σ_{dark} is observed for all maximum process temperatures $T_{\max} > 600$ °C (Fig. 7.3 a, left axis, black). For these samples σ_{dark} increases over four orders of magnitude compared to the as-deposited reference.

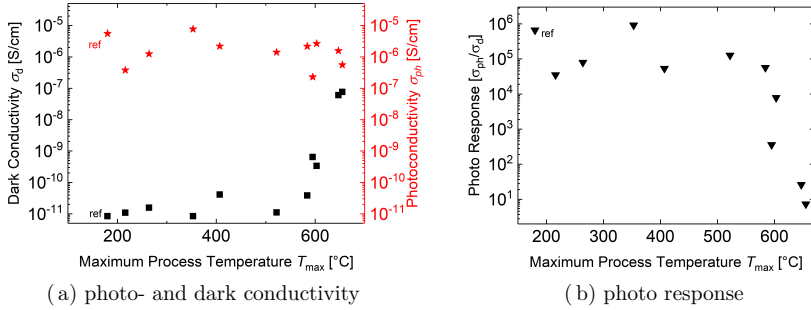


Figure 7.3: (a) Influence of the maximum process temperature on the dark conductivity (black squares, left y-axis) and photoconductivity (red stars, right y-axis). (b) Photo response of the laser treated amorphous silicon thin-film depending on the maximum temperature measured during the laser treatment.

As a result of the increasing dark conductivity, the photo response drops for $T_{max} \geq 575$ °C over four orders of magnitude (Fig. 7.3b). As observed for the hydrogen concentration, the photo response is dominated by the maximum temperature during the laser treatment that is resulting from the absorption of the laser radiation (Fig. 7.3 b).

Photothermal Deflection Spectroscopy In order to gain a more detailed insight into the influence of the laser treatment on deep defects, the sub-bandgap absorption was determined with PDS measurements [17,134]. The influence of the laser treatment on the sub-bandgap absorption coefficient of a-Si:H is presented in Figure 7.4 a). Here, the measured maximum process temperatures range from $T_{max} = 250$ °C to $T_{max} = 660$ °C. The optical gap shifts to lower energies for $T_{max} \geq 520$ °C. The results indicate no influence on the sub-bandgap absorption at $E = 1.2$ eV for measured maximum process temperatures $T_{max} < 584$ °C.

An increase of the sub-bandgap absorption is observed exclusively for measured process temperatures above $T_{max} > 600$ °C (Fig. 7.4 b). Here, the sub-bandgap absorption increases over one order of magnitude for $T_{max} = 655$ °C, compared to the untreated reference. The observations made for the sub-bandgap absorption are in agreement with the findings for the increasing dark conductivity.

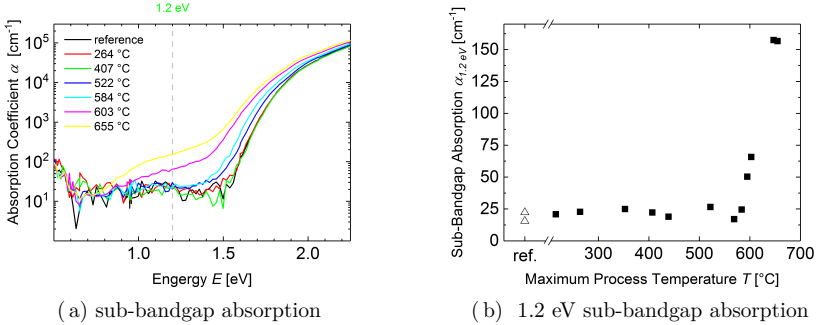


Figure 7.4: (a) Influence of the laser treatment of a-Si:H on the sub-bandgap absorption. The sub-bandgap absorption is shown for the maximum process temperatures $250\text{ }^\circ\text{C} < T_{\text{max}} < 660\text{ }^\circ\text{C}$ that were achieved due to the laser treatment of a-Si:H. The sub-bandgap absorption at 1.2 eV is indicated with the gray dashed line. (b) Sub-bandgap absorption at 1.2 eV depending on the measured maximum process temperature (black squares). The sub-bandgap absorption of the deposited references is shown in open triangles.

7.2.4 2D FEM Heat Transfer Simulation

In order to gain insight into the temperature distribution on the sample surface and throughout the sample (Fig. 7.6), a 2D FEM simulation was performed with ELMER for one example laser process. The simulation was performed for an absorbed average laser power of $P = 10\text{ W}$ ($\cong 44\text{ A}$ laser diode current) and an irradiation time of $t = 10\text{ s}$. These parameters result in a measured temperature of $T = 584\text{ }^\circ\text{C}$. As will be demonstrated later in this chapter, temperature simulations can be conducted with the average laser Power.

Here, the temperature distribution was simulated for area of $10 \times 1.1\text{ mm}^2$. Figure 7.5 illustrates the simulation model. Surface absorption was assumed for this simulation as $d_{\text{a-Si:H}} \ll d_{\text{substrate}}$ and both a-Si:H and glass exhibit a similar heat conductivity. In this 2D axis symmetric simulation an ideal tophat beam profile is assumed. The irradiated area is situated between the symmetry axis $w = 0\text{ mm}$ and $w = 2.5\text{ mm}$. This region corresponds to the source of heat and is indicated in Figure 7.5 (left) with the red line.

Losses are taken into account at the interfaces (blue arrows). As the intensity of the laser radiation is orders of magnitude higher than the heat radiation, losses due to heat radiation can be neglected. A heat transfer coefficient of

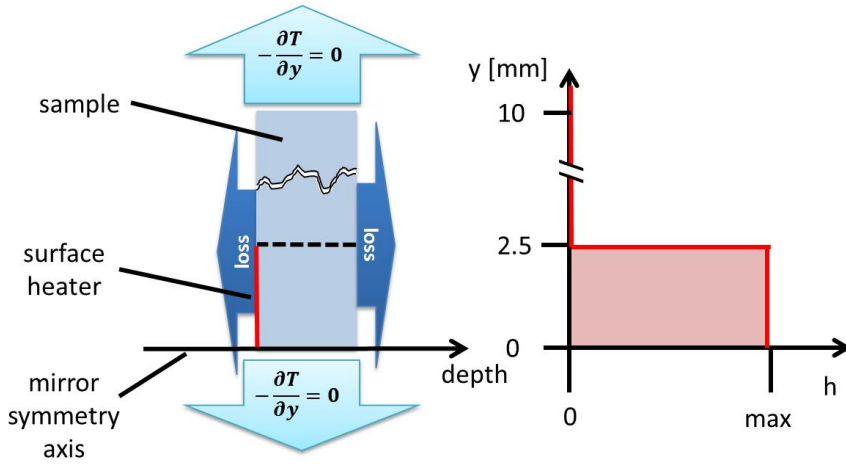


Figure 7.5: Simulation model for the determination of the heat diffusion in non-irradiated areas (left) under the assumption of an ideal tophat laser beam profile. The assumed laser intensity profile is represented by the power of a heat source (h) depending on the position (right).

$\alpha = 12 \text{ W/m}^2$ is applied for the heat transfer from glass to air. Newman BC with zero heat flux are assumed at the boundary of the simulation area.

Figure 7.6 presents the simulated heat distribution of a Corning Eagle XG glass substrate with a thickness $d = 1.1 \text{ mm}$ after an irradiation time of $t = 10 \text{ s}$. The simulation results show that even assuming an ideal tophat beam profile, a strong temperature gradient of approximately $\Delta T = 225 \text{ }^\circ\text{C}$ is found at the sample surface over the irradiated area. The maximum temperature at $x = 0 \text{ mm}$, $y = 0 \text{ mm}$ is $T_{\text{sim,max}} = 664 \text{ }^\circ\text{C}$, while the temperature at $x = 0 \text{ mm}$, $y = 10 \text{ mm}$ is $T = 33 \text{ }^\circ\text{C}$. The maximum temperature retrieved from FEM simulations is considerably higher than the measured maximum temperature of $T_{\text{pyro,max}} = 584 \text{ }^\circ\text{C}$. This will be discussed in Section 7.4.

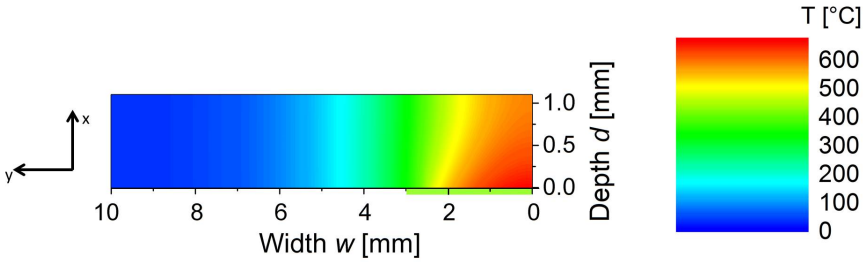


Figure 7.6: Simulated temperature profile after an irradiation time of $t = 10$ s for an absorbed average laser power of $P = 10$ W assuming an ideal tophat beam profile. The irradiated region is indicated with the green line.

Lateral Resolved Hydrogen Concentration

In addition, c_H was determined with Raman spectroscopy depending on the position on the sample (Fig. 7.7). Therefore, ten measurements with an offset of 0.5 mm each, were performed parallel to the x-axis attempting to measure over the hottest spot on the sample.

The simulated surface temperatures, according to Figure 7.7, are assigned to the x-axis for the corresponding positions. The relative c_H is plotted on the y-axis. Here, the hydrogen concentration was normalized to a non-irradiated area on the sample.

The results of the Raman measurements show an asymmetric hydrogen concentration (Fig. 7.7) distribution. The slope of the c_H increase is steeper on the right hand side than on the left hand side. This asymmetry is in accordance with the beam profile presented in Section 4. In conclusion, the lateral resolved analysis and the 2D heat transfer simulations show that a small displacement of the measurement point for both temperature and Raman have a huge impact on the measured values. This is assumed to be a major impact on the scattering of c_H depending on T (Fig. 7.2).

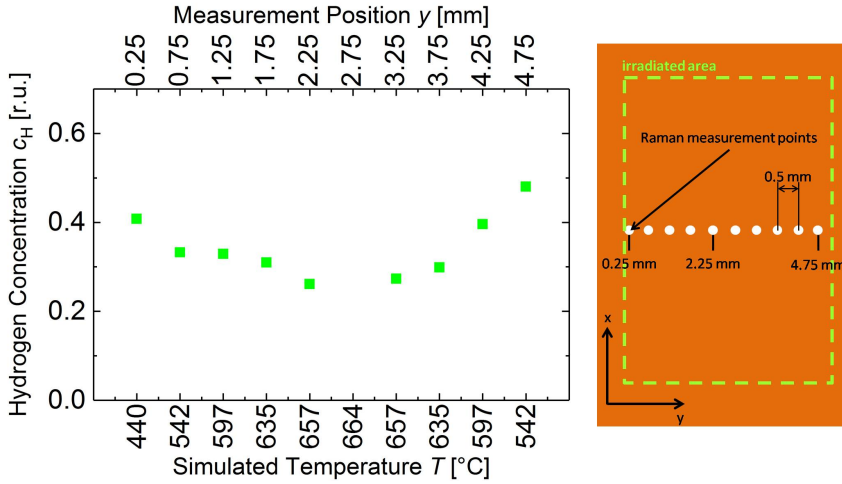


Figure 7.7: Relative change of c_H determined with Raman spectroscopy for an excitation wavelength of $\lambda = 532$ nm (green squares). The hydrogen concentration is plotted depending on the position on the sample while the corresponding simulated maximum process temperature is indicated on the x-axis. On the right hand side a sketch of the analyzed sample is shown. The white dots indicate the Raman measurement points, while the dashed green line indicates the irradiated area on the sample.

7.3 Simulations

In this section simulations of hydrogen diffusion as a result of a measured temperature development as well as the temperature evolution due to a laser treatment are performed. Therefore, 1D simulations based on Fourier transformation were used in order to evaluate the influence of the pulses on the temperature. This pulse-dependent temperature development is presented in Section 7.3.1.

Based on the results of Section 7.3.1, 1D FEM simulations are performed with ELMER® to determine the hydrogen concentration profile. Based on the results of Chapter 6, the expected measured hydrogen concentration (by Raman) is calculated from the diffusion profiles. The hydrogen concentration resulting from the laser treatment is determined for measured temperature profiles.

7.3.1 1D Laser Pulse Dependent Temperature Evolution

In order to calculate the time dependent temperature evolution of a pulsed laser source with nanosecond laser pulses, simulations on a sub-nanoscale time resolution are inevitable. Though, 2D or 3D simulations on a time scale in the order of several tens of seconds with a sub-nanosecond time resolution would be extremely computation intensive. Therefore the simulation model has to be simplified. In this section it is evaluated, if the temperature course of the treatment with nanosecond laser pulses can be approximated with a mean laser power. Therefore, 1D temperature calculations were used to compare the resulting temperature evolution for a mean laser power and a pulsed laser source with the same mean power.

First, the time-dependent temperature on the sample surface is calculated for a single pulse. Therefore, the temperature evolution corresponding to two simplified pulse forms is analyzed. The temperature developments for a boxcar function and a δ -function are calculated. In order to obtain a strong temperature increase on a short time scale, it is assumed that an average laser power of $P = 17.4 \text{ W}$ is absorbed on a surface with a size of $5 \times 9 \text{ mm}^2$. These parameters result in a power density of $3.9 \times 10^5 \text{ W/cm}^2$ and a pulse energy of $1.93 \times 10^1 \text{ J/m}^2$ for a pulse duration of $\tau_{\text{pulse}} = 7 \text{ ns}$.

The amount of energy is equal for both the boxcar function and the δ -function. Regarding the boxcar function, a pulse duration of $\tau_{\text{pulse}} = 7 \text{ ns}$ is considered. The resulting time-dependent temperature development for one single pulse is presented in Figure 7.8 for both the δ -function (black line) and the boxcar function (red line). The simulation time ends at the beginning of the next pulse ($t = 25 \text{ }\mu\text{s}$). After approximately $t = 50 \text{ ns}$ the temperature evolutions for the δ -function and the boxcar function are almost identical. The inset on the upper right proves that the temperature increase is equal for both methods at the beginning of the next pulse. Indeed, the integrated surface $A_{\text{integ}} = 1.405 \times 10^{-5}$ is equal for both functions up to three digits. Accordingly, the δ -function can be used with Fast Fourier Transformations (FFT) to calculate the time-dependent temperature development for the pulsed laser source.

In addition, the time-dependent temperature evolution of the boxcar function (Fig. 7.8) indicates that the elevated temperature due to the short laser pulses has no significant contribution to the hydrogen diffusion. Taken into account the diffusion length L_{diff} with

$$L_{\text{diff}} = \sqrt{Dt} \quad (7.1)$$

and the diffusion coefficient D ,

$$D = D_0 e^{-E_A/(k_B T)} \quad (7.2)$$

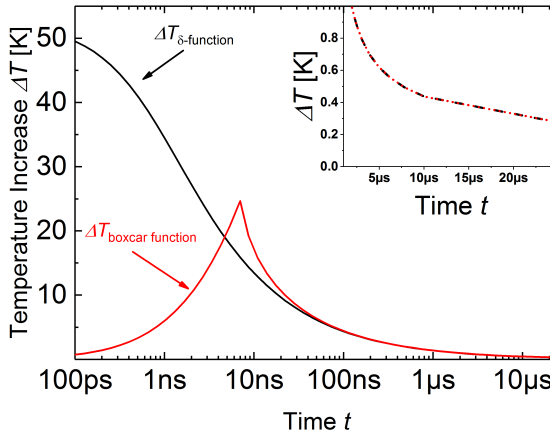


Figure 7.8: Simulated temperature course on a logarithmic time scale for a single pulse at room temperature for a delta function shaped pulse form (black line) and a boxcar-function pulse form (red line). The inset presents the same simulation result on a linear time scale.

where D_0 is the diffusion coefficient prefactor, E_A the activation energy, k_B the Boltzmann constant and T the temperature, it is obvious that the contribution of the pulses to the diffusion length at an elevated temperature of less than $T \leq 30$ °C on a ns time scale is small compared to the overall pulse pause time. This implies that a cw laser source can be used in FEM simulations without a significant loss of accuracy.

In order to validate that the average laser power and the resulting average temperature can be used for the FEM simulations, the time-dependent temperature development is calculated for 10000 laser pulses. For these calculations, the temperature that is retrieved 25 μ s after the beginning of the pulse, just at the beginning of the next pulse, is used as initial temperature for the following pulse. In addition, the temperature after $t = 25$ μ s is calculated for an average laser power (cw).

Figure 7.9 shows the time dependent temperature increase for both, the δ -function and the corresponding cw time dependent temperature calculations. The black line refers to the temperature increase generated by a pulsed power source (δ -function), while the red line refers to a continuous power source, respectively. Please note, that the accumulated temperature increase at the beginning of the

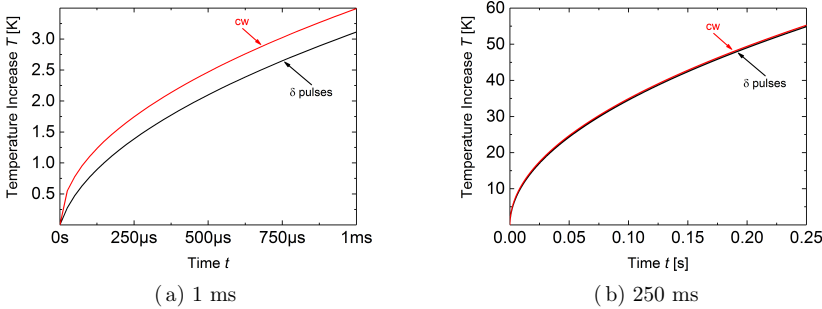


Figure 7.9: Comparison of the temperature development for a pulsed laser source (black line) and a cw laser source (red line).

next pulse is compared here. Both simulations, for laser pulses and for cw, lead to similar results. The evolution of both cw and pulses develops parallel after an initial higher increase for the cw laser (Fig. 7.9 a). The temperature difference for two subsequent pulses converges with increasing number of pulses n . After a simulated treatment time of $t = 25$ ms (1000 pulses), the temperature difference of $\Delta T_{\text{cw,pulse}} = 0.4$ K stays constant between the pulsed and cw case (Fig. 7.9 b).

It has been demonstrated that the results of the 1D calculations for the time dependent temperature development of the accumulated temperature increase and the time dependent temperature development of a continuous heating lead to comparable results. In addition, the time dependent temperature increase of an individual pulse is in the order of several tens of Kelvin on a nanosecond timescale. Therefore, the elevated temperature increase due to the laser pulses can be neglected for the hydrogen diffusion simulations. As a consequence, the temperature profiles that were measured with a pyrometer can be used to calculate the expected hydrogen content and distribution for a given time dependent temperature profile. In addition, these results show that FEM heat transfer simulations can be conducted with the equivalent average power as done in Section 7.2.4.

7.3.2 1D FEM Hydrogen Diffusion Simulations

For the 1D FEM hydrogen diffusion simulations, room temperature and a constant hydrogen concentration throughout the layer were assumed as initial conditions. Dirichlet BC with $c_{\text{H}} = 0$ for both the a-Si/air interface as well as the a-Si/glass interface were applied in this simulation. Details on the simulation and

the parameters are given in Chapter 2. The temperature was recorded during the experiments. This time dependent temperature evolution was used as surface heater for the simulations to determine the c_H profiles. Due to the high absorption of a-Si:H at $\lambda = 532$ nm, the laser power is completely absorbed within the a-Si:H layer. First, the resulting hydrogen concentration was calculated exclusively for thermal effects.

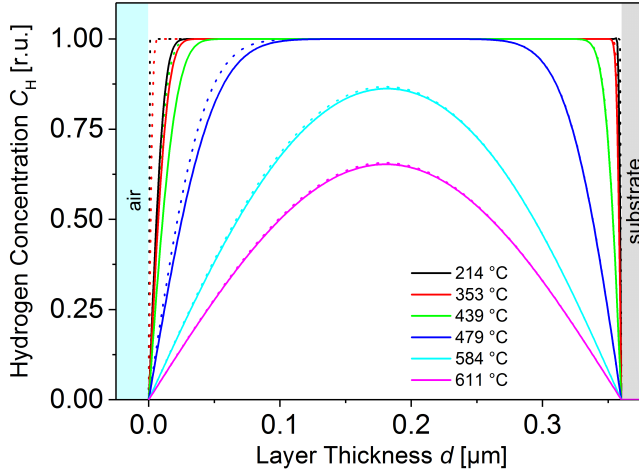


Figure 7.10: Dashed lines show the simulated c_H profile based on the measured temperature evolution as a result of the laser treatment. The solid lines refer to a simulated c_H profile under consideration of both, the temperature evolution and the laser power dependent irradiation intensity. Light enhanced diffusion is seen to be active at low temperatures and at the irradiated side (here: left) of the thin-film.

It has been demonstrated before that intense irradiation has an impact on the hydrogen diffusion in a-Si:H [135–137]. Therefore, a term corresponding to the absorption of light in a-Si:H, due to the law of Lambert-Beer, was added mathematically in a second simulation. The results of both simulations are compared and discussed in this section.

Figure 7.10 shows the simulated hydrogen concentration profile in the a-Si:H layer exclusively due to the measured temperature evolution (dashed lines) and as a result of light-enhanced diffusion (solid lines). Here, differences in the diffusion profile are observed. First, the simulation including the light enhanced diffusion (Fig. 7.10, solid lines) exhibits an asymmetric diffusion profile, while

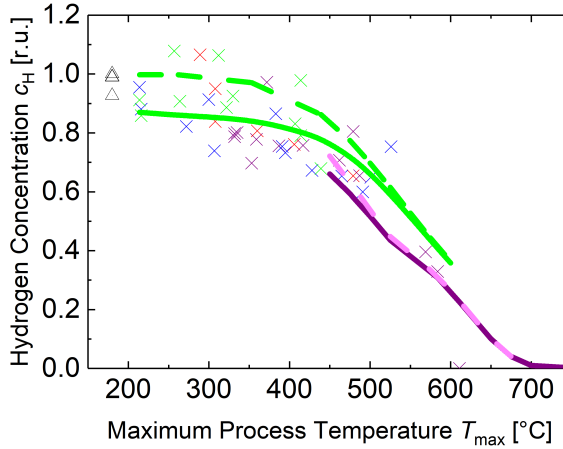


Figure 7.11: Hydrogen concentration depending on the maximum process temperature. The crosses refer to the Raman measurements (green $t = 3$ s, blue $t = 4$ s, red $t = 7$ s, and violet $t = 10$ s), while the lines result from simulations (green $t = 3$ s, violet and the pink dashed line $t = 10$ s). The dashed lines result from the simulations exclusively due to thermal effects, while solid lines refer to simulations considering the light enhancement. The open triangles refer to the as-deposited reference.

the simulation considering exclusively a thermal contribution to the diffusion are symmetric. This asymmetry is more pronounced for lower temperatures while the development of both simulation models converges for higher temperatures. Secondly, the hydrogen concentration decreases already for maximum process temperatures as low as $T_{\max} = 214$ °C at the irradiated side (air). On the other hand, the c_H profile does not change significantly for $T_{\max} \leq 439$ °C for an exclusively thermal driven diffusion (Fig. 7.10, dashed lines).

Figure 7.11 presents c_H depending on the maximum temperature measured for the laser treatment. The plot colors refer to a dedicated laser treatment time. Here, green refers to $t = 3$ s, blue to $t = 4$ s, red to $t = 7$ s and the violet to $t = 10$ s, respectively. The colored crosses illustrate c_H as determined using Raman spectroscopy while the open triangles refer to the as-deposited reference. The lines are evaluated from FEM simulations.

In order to obtain simulation results for maximum temperature values without existing measured temperature profiles, constant values were added or subtracted

from measured temperature profiles. When a constant value is added to a measured temperature evolution, the integral temperature is overestimated, while it is underestimated for a subtraction, respectively. The laser power was adapted by the linear regression of T_{\max} versus P_{laser} in these simulations (see Fig. 7.1 b).

Most of the measured values of c_{H} are smaller than the values obtained from exclusively thermal driven diffusion (green dashed line). The hydrogen concentration resulting from the light enhanced diffusion is presented in Figure 7.11 with solid lines. Both, the light enhanced and the exclusively thermal simulated hydrogen concentration converge for higher temperatures.

7.4 Discussion

Figure 7.11 shows a lot of scatter for the hydrogen concentration determined with Raman spectroscopy. This effect will be discussed in the following. According to the results of Section 7.3.2 a residual hydrogen concentration of $c_{\text{H,sim}} = 0.31$ is expected for the irradiation time of $t = 10$ s and the temperature profile with $T_{\max} = 584$ °C. Considering a spot diameter of the pyrometer of $D_{\text{spot}} = 2.5$ mm this is equivalent to c_{H} obtained by the average of the measurement positions 3-8 (Fig. 7.7). Even though the maximum of the simulated temperature is higher than the measured temperature, the resulting c_{H} is in agreement with both. The expected measured c_{H} is calculated from the simulated depth-dependent hydrogen concentration profile analogous to the expected hydrogen concentration calculated from SIMS measurements (see Chapter 6, equation 6.6) with

$$c_{\text{H}} = \frac{1}{d} \int_0^d C_{\text{H}}(x) \cdot e^{-2\alpha x} dx \quad (7.3)$$

where C_{H} is the depth-dependent hydrogen concentration of the FEM simulations, d is the depth where the signal is obtained, and α is the absorption coefficient for the desired Raman wavelength.

Due to the strong surface temperature gradient (see Fig. 7.6), small displacements of the pyrometer measurement point from the center will lead to smaller measured temperatures. In addition, the measurement area is larger than the spot with the maximum temperature and an average area temperature is measured with the pyrometer. As a result, the maximum measured temperature will always be smaller than the real temperature.

Figure 7.11 presents a comparison of the measured c_{H} with c_{H} calculated from the simulated diffusion profiles. The analysis of the hydrogen concentration using Raman spectroscopy shows a continuous c_{H} decrease with increasing maximum process temperature (see also Sec. 7.2). It can be seen that for exclusively

temperature driven calculations no significant c_{H} decrease is observed for $T \leq 425$ °C (Fig. 7.11, solid line) for the short time at elevated temperatures (see Sec. 7.2.1). However, the results from the Raman measurements indicate a decrease of c_{H} for all laser treated samples. This is in accord with the simulation results that take the irradiation in account (solid lines). Here, the hydrogen concentration decreases even though there is no significant temperature increase compared to the deposition temperature.

Indeed, Figure 7.11 presents a well-defined difference between the measured and simulated hydrogen concentration for maximum process temperatures $T_{\text{max}} < 450$ °C. Due to the simulation results (dashed lines), c_{H} starts to decrease significantly for $T \geq 413$ °C, whereas c_{H} has already been reduced according to the measurements. Here, the scattering of the measured data points has to be taken into account. Though, a clear trend for the decreasing hydrogen concentration is observed. Concerning the scattering, a variation of c_{H} of the individual samples is expected. In addition, measurement uncertainties of the temperature and the Raman measurement position related to T_{max} (Section 7.2.4) as well as the Raman signal intensity lead to scattering of the measurement values. Therefore, a decrease of 15 % to 20 % is estimated for maximum process temperatures between $T = 400$ °C and $T = 450$ °C. As amorphous materials are sensitive to light induced structural changes, the decrease in the hydrogen concentration for process temperatures $T_{\text{max}} < 450$ °C is deduced to a light induced process [120, 122, 138]. Both, the light enhanced and the exclusively thermal simulated hydrogen concentration converge for higher temperatures. The hydrogen concentration decrease for lower temperatures can be traced back to a light enhanced diffusion process. This finding is consistent with the theories of Stutzmann as well as Branz [139, 140]. Stutzmann et al. state that weak Si-Si bonds with H on one of the back bonds in a-Si:H (Fig. 7.12 a) are broken due to irradiation (Fig. 7.12 b) [139].

First, an optically excited hole is then trapped in this weak bonding state. As a result of the nonradiative recombination of an electron in this hole state the vibrational energy is high enough to break this bond (indicated by the pink arrows). The back-bonded hydrogen will then switch into the position of the broken bond (Fig. 7.12 b). Vice versa, the hydrogen can swing back to the stable state (Fig. 7.12 a) under heat influence when an electron of the dangling-bond orbital is excited into a conduction band state. This will allow the silicon to form sp^2 states (Fig. 7.13 b), instead of the usual sp^3 hybrid states of silicon (Fig. 7.13 a) and the hydrogen can swing back. It has been observed before, that irradiation promotes the hydrogen diffusion [135–137, 141]. It is assumed, that a hydrogen atom is available for diffusion as unbounded hydrogen when it switches the bonding position, leading to an augmented diffusion coefficient under intense irradiation. This finding is also in accord with Branz hydrogen collision model, where it is hypoth-

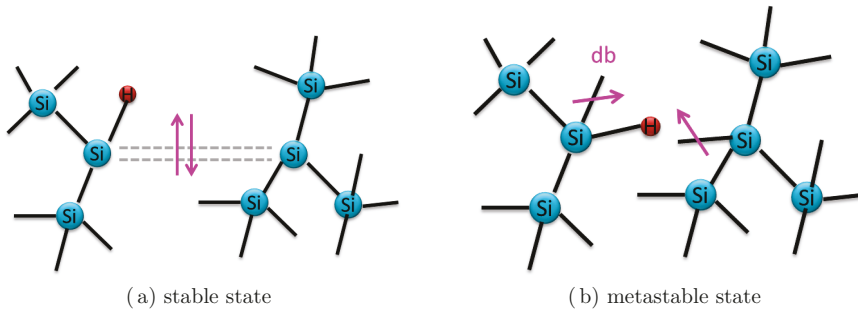


Figure 7.12: Model of the microscopic realization of the stable and metastable state of a-Si:H corresponding to Stutzmann [139].

esized that mobile hydrogen is weakly bound and diffuses through a-Si:H [140]. Here, hydrogen is considered to be already diffusing at room temperature due to irradiation, as demonstrated by Kali et al. [141]. Consequently, an increased temperature will lead to a further increased diffusion coefficient.

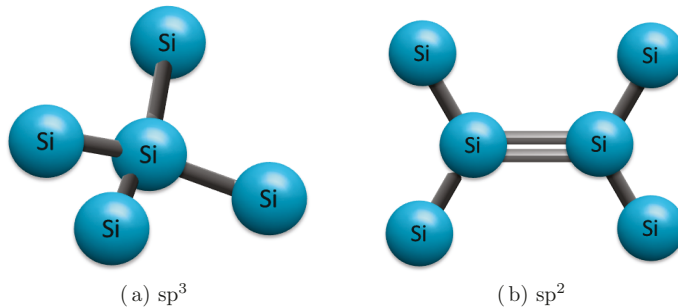


Figure 7.13: Hybrid states for silicon. 7.13 a) sp^3 hybrid state for silicon and 7.13 b) sp^2 hybrid state for silicon.

However, an obvious dependency of the hydrogen concentration depending on the exposure time could not be observed for the Raman measurements. This can be traced back to the strong scattering of the measurement data. In contrast, the hydrogen concentration appears to be primarily dependent on the maximum process temperature. This is in agreement with the diffusion length that is linearly dependent on the time but exponentially dependent on the temperature.

An increase in the number of dangling bonds is not detected here for process temperatures below $T = 603$ °C. This can be deduced to the heating of the

sample during the laser treatment where two concurring processes, the creation of dangling bonds and the healing of dangling bonds occur simultaneously. The results indicate that the maximum process temperature is the limiting factor for the quality of the a-Si:H after dehydrogenation. Though, further experiments should be performed to find whether the number of pulses or the intensity of the irradiation has an influence on the number of dangling bonds.

The investigation of the electrical and optical properties demonstrated that c_H can be reduced by 40 % without negative impact on the electrical or optical properties. The photoresponse was not affected for process temperatures below $T = 522$ °C with a corresponding remaining hydrogen concentration of less than 9 at.%. The photoconductivity is widely used as a figure of merit to characterize the photo-induced degradation. A decrease of σ_{photo} is associated with an increase of the density of dangling bonds [142]. Though σ_{photo} is also sensitive to ionized impurities and will increase e.g. with increasing oxygen concentration. Consequently, a constant photoconductivity is not sufficient as a qualifier for changes in the material. The dark conductivity increases with the doping level, therefore it should be as low as $\sigma_{\text{dark}} = 10^{-10} \text{ } \Omega^{-1}\text{cm}^{-1}$ for device grade intrinsic material. The strong increase of the dark conductivity for $T \geq 584$ °C indicates that either impurities are incorporated in the material or that defects are created. The increase of the sub-bandgap absorption of the PDS measurements is linked to an increase of deep defects that consist mainly of dangling bonds. The sub-bandgap absorption does not increase for all process parameters with a resulting maximum process temperature below $T \leq 584$ °C. This shows that the density of dangling bonds is not affected for a laser treatment within the corresponding parameter range.

Using laser enhanced dehydrogenization it is possible to modify and model the amorphous silicon layer over a wide parameter range without impact on the electrical properties. The optical gap is shifted to lower energies with increasing process temperature (Fig. 7.4 a) due to the decreasing hydrogen concentration. The dependency of the mobility gap on the hydrogen concentration has also been observed for experiments with varying substrate temperatures during the deposition [143]. Yamaguchi et al. found in addition that the degree of disorder does also influence the optical gap. As the optical properties of a-Si:H can be influenced using laser treatment without affecting the electrical properties and without increasing the sub-bandgap absorption it is indicated that the manner of the hydrogen incorporation in the amorphous network is not affected by laser annealing, if the resulting maximum process temperature is smaller than $T = 522$ °C.

8 Laser Treatment of Microcrystalline Silicon

In this chapter, the second aim of this thesis, the use of a laser treatment in order to produce good contacts on passivated c-Si wafers, is investigated and discussed. Hereby, the focus lies on reducing the resistivity of the contact layer (here: $\mu\text{c-Si:H}$) without reducing the quality of the SiO_2 passivation on the c-Si wafer. The resistivity of the contact layer contributes to the series resistance of a solar cell. Hence, a decreased resistivity of the contact layer will lead to a higher solar cell performance.

Section 8.1 presents the properties of p-type $\mu\text{c-Si:H}$ on glass. In order to perform the electrical characterization, an insulating substrate is mandatory. Here, the influence of the specific laser treatment on the resistivity ρ , Hall mobility μ_{H} , and carrier concentration p as well as the Raman crystallinity X_{C} was analyzed. Two different laser concepts were investigated. The first concept is based on a line shaped laser beam at a wavelength of $\lambda = 532 \text{ nm}$. The second concept uses a laser at a wavelength of $\lambda = 355 \text{ nm}$ with a Gaussian beam shape. Both lasers are scanned over the sample. The results are presented in Section 8.1.2 and Section 8.1.3, respectively. Based on the results from Section 8.1.2 and 8.1.3 the laser source with $\lambda = 532 \text{ nm}$ was chosen for the treatment of p-type $\mu\text{c-Si:H}$ on c-Si wafers. The experimental investigations and the results of the laser treatment of p-type $\mu\text{c-Si:H}$ on c-Si substrates are presented in Section 8.2.

8.1 p-type $\mu\text{c-Si:H}$ on Glass Substrates

8.1.1 Sample Fabrication

First, p-type $\mu\text{c-Si:H}$ thin-films were deposited with PECVD on $10 \times 10 \text{ cm}^2$ Corning Eagle XG glass substrates. This deposition was performed at a pressure of $p = 12.5 \text{ mbar}$, a gas flow of 8.6 sccm silane (SiH_4), 3000 sccm hydrogen (H_2), and 0.8 sccm trimethylborane (TMB) and an rf power (13.65 MHz) $P_{\text{rf}} = 400 \text{ W}$. As a result of these deposition parameters, a p-type $\mu\text{c-Si:H}$ layer as used as standard p-layer for tandem or $\mu\text{c-Si:H}$ solar cells is obtained. Figure



Figure 8.1: Sketch of the samples as used for the experiments with p-type $\mu\text{c-Si:H}$ on glass to evaluate the influence of the laser treatment on the resistivity, the Hall mobility, and the carrier concentration.

8.1 illustrates the scheme of the cross section of these samples. In this PECVD deposition process nine $10 \times 10 \text{ cm}^2$ substrates are obtained simultaneously. The arrangement inside the PECVD chamber is illustrated in Figure 8.2. All glass substrates used for this chapter originate from the same deposition run. For the electrical characterization $11 \times 11 \text{ mm}^2$ square samples were electrically isolated as represented in Figure 8.5 and Figure 8.9.

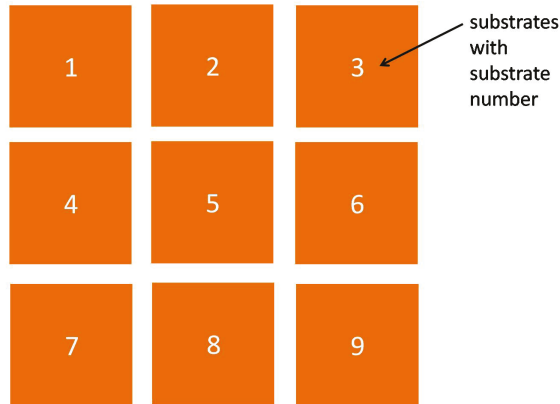


Figure 8.2: Scheme of the substrate arrangement inside the PECVD chamber. The numbers one to nine are assigned to the individual substrate positions.

Thickness of the p-type $\mu\text{c-Si:H}$ Thin-Film on Glass Substrates

To characterize the uniformity of the deposition process and its impact on the reflectance of the laser beam, the layer thickness of one example substrate (substrate no. 3) was determined with a Dektak profiler as described in Chapter 3. Due to

incomplete ablation, only three out of five ablated double lines were evaluated. One of those is situated exactly in the center of the substrate, while the other two are closer to the edges of the substrate. The resulting calculated average layer thickness is $d = 70 \pm 2.5$ nm. Contact layer thicknesses with $30 \text{ nm} \leq d \leq 100 \text{ nm}$ are within the range for the trade-off between low ohmic losses and low recombination losses in the contact layer. The thickness of the p-type $\mu\text{-Si:H}$ thin film is not uniform over the whole deposition surface. Due to the variation of the thickness of about $\pm 3.5\%$ on this example substrate, a thickness variation of $\pm 5\%$ over all substrates is expected.

Reflectance, Transmittance and Absorptance of the p-type $\mu\text{-Si:H}$ Thin-Film on Glass Substrates

In order to find whether the application of the laser treatment from glass side or layer side is more favorable, the reflectance and absorptance as well as the influence of the thickness variation was determined for two randomly chosen substrates (substrate no. 2 and substrate no. 3).

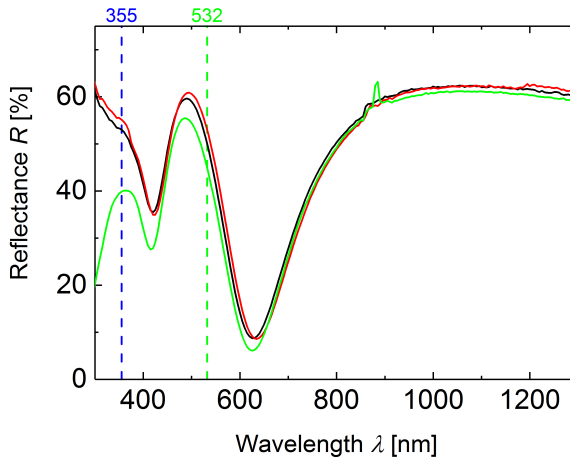


Figure 8.3: Reflectance of the p-type $\mu\text{-Si:H}$ layer on glass of two substrates. The black (substrate no. 2) and red (substrate no. 3) line refer to measurements from the layer side, while the green (substrate no. 2) line refers to a measurement from the substrate side. The vertical dashed lines indicate the reflection at the laser wavelengths, 355 nm (blue) and 532 nm (green).

The reflectance and the transmittance of the p-type $\mu\text{c-Si:H}$ thin-film on glass was measured from both film and glass side according to Section 3.3.3. Then the absorptance was calculated from these measurements. The results of the reflectance measurement are presented in Figure 8.3. Here, the red (substrate no. 3) and the black (substrate no. 2) solid lines refer to the wavelength dependent reflectance of the two individual substrates from the film side, while the solid green line refers to the measurement from the glass side of substrate no. 2.

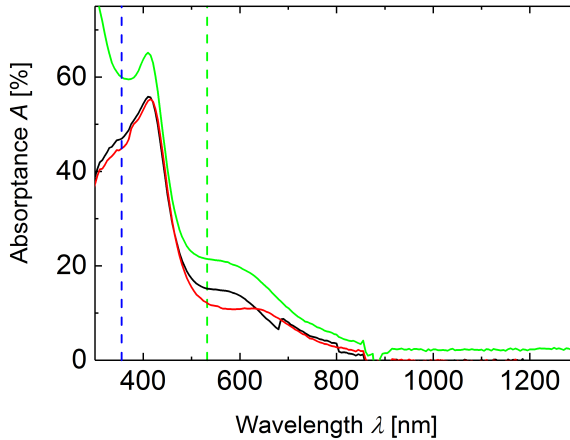


Figure 8.4: Absorbance of the p-type $\mu\text{c-Si:H}$ layer on glass. The black (sample no. 2) and red (sample no. 3) lines refer to measurements from layer side, while the green (sample no. 2) line refers to measurement from the substrate side. The vertical dashed lines indicate the absorbance at 355 nm (blue) and 532 nm (green) laser wavelengths.

The absorption at the laser wavelengths $\lambda = 532$ nm and $\lambda = 355$ nm is of special interest for the subsequent experiments. Therefore, they are shown in Figure 8.3 and Figure 8.4, with green and blue dashed lines. As illustrated in Figure 8.3, the reflectance is lower from the glass side than from the film side for both laser wavelengths. The reflectance changes between the different substrates and even over one substrate are due to the interference of the thin-film. The interference of the thin-film is subject to the non-uniform layer thickness.

The absorbance of the green laser with $\lambda = 532$ nm varies from 12.3% to 15.2% for the treatment from the layer side. However, 21.5% are absorbed for treatment from the glass side (Fig. 8.4). Considering the absorbance of UV-light at a wavelength of $\lambda = 355$ nm, 60% of the incident laser power is absorbed

for treatment from the glass side, while only 45% to 47% are absorbed for the treatment from the layer side, respectively. Based on the higher absorbed fraction, the $\mu\text{-Si:H}$ samples on glass substrates were treated from the glass side for both laser sources used for this part of the thesis.

8.1.2 Laser Treatment of p-type $\mu\text{-Si:H}$ at 532 nm with a Line Shaped Laser Beam

Treatment Details

In this section the impact of a treatment with a $\lambda = 532$ nm laser on the resistivity ρ , the Hall mobility μ_{H} , the carrier density p , and the Raman crystallinity X_{C} of p-type $\mu\text{-Si:H}$ on glass is investigated. For this treatment the Edgewave HD30II-E Innoslab laser (see Ch. 4) at a wavelength of $\lambda = 532$ nm, a pulse duration of $\tau_{\text{pulse}} = 7$ ns, and a repetition rate of $\nu = 40$ kHz was used. This laser has a line shaped beam profile that is similar to a tophat in both x and y-direction. A cylindrical lens was used to focus the y-direction. More details on the system and the setup can be found in Section 4.1.

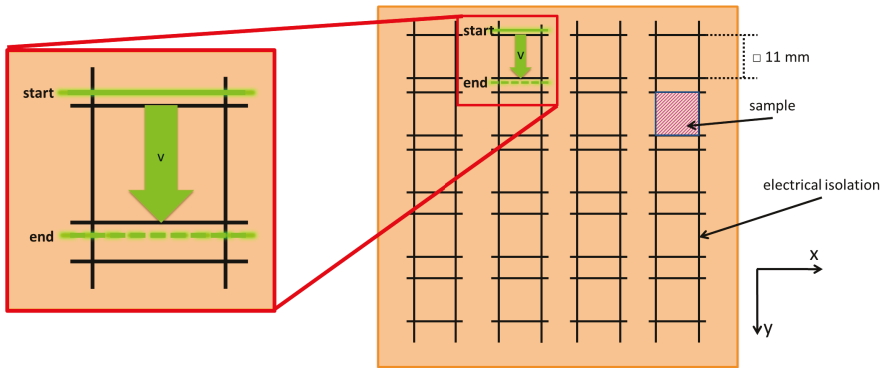


Figure 8.5: Layout of one substrate for the laser treatment of p-type $\mu\text{-Si:H}$ with $\lambda = 532$ nm. The solid black lines show the previously ablated electrical isolation lines. Each sample for the laser treatment has a size of 11×11 mm. One example sample is indicated with the pink hatched square. The substrate is moved in y-direction with the velocity v , while the position of focus of the laser is fixed. The starting and ending position of the laser scan is indicated with the green solid line and the green dashed line, respectively.

Based on the results of Section 8.1, the laser treatment was performed through the glass side. The layout for the treatment of the substrates is shown in Figure 8.5. The laser focus and position is fixed, while the substrate is mounted on an automated x-y translation stage. The width of the laser beam exceeds the size of the beforehand isolated $11 \times 11 \text{ mm}^2$ squares in x-direction (Fig. 8.5). In addition, the laser scan was started and ended outside the isolated $11 \times 11 \text{ mm}^2$ sample area in order to avoid the influence of the acceleration and breaking ramps. The starting and ending positions of the laser scan are indicated in Figure 8.5 with the green solid line and the green dashed line. As the whole substrate exceeds the maximum sample size for the electrical characterization, the samples have to be singularized after the laser treatment with a glass cutter.

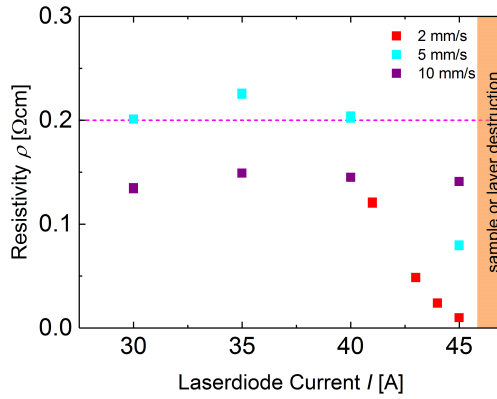


Figure 8.6: Influence of laser treatment with a pulsed line laser at a wavelength of $\lambda = 532 \text{ nm}$ on the resistivity of p-type $\mu\text{c-Si:H}$ dependent on the laser diode current and the scanning velocity. The pink dashed horizontal line indicates the average as-deposited resistivity. The different colors of the squares refer to the scanning velocity (violet: $v = 10 \text{ mm/s}$, cyan: $v = 5 \text{ mm/s}$, red: $v = 2 \text{ mm/s}$)

Parameter Range

In order to determine suitable parameters for the laser treatment, the velocity and the laser diode current were varied on one substrate over a wide range. The parameters are listed in Table 8.1 and the results are shown in Figure 8.6. The sample resistivity prior to processing was measured by $\rho_{\text{initial}} = (0.199 \pm 0.015) \Omega\text{cm}$. For the reason that the reference on this substrate was destroyed during the cutting

process, the as-deposited resistivity was determined on another substrate of the same deposition run. At a laser velocity of $v = 10$ mm/s, the resistivity ρ does not change for laser diode currents between $I = 30$ A and $I = 45$ A (Fig. 8.6, violet squares). On the other hand, the resistivity ρ decreases by a factor of two for the treatment at $v = 5$ mm/s and a laser diode current of $I = 45$ A (Fig. 8.6, blue squares). Treatment parameters at an elevated laser diode current or slow scanning velocities can lead to ablation or partial ablation of the p-type $\mu\text{-Si:H}$ layer and to cracks in the substrate. Those destructions of the samples are marked in the parameter tables.

Table 8.1: List of samples and the corresponding treatment parameters as well as the state of those samples

| sample ID | I [A] | v [mm/s] | comment |
|-----------|---------|------------|---------------------------|
| 1 | 30 | 5 | |
| 2 | 35 | 5 | |
| 3 | 40 | 5 | |
| 4 | 45 | 5 | |
| 5 | 50 | 5 | partial ablation |
| 6 | 55 | 5 | partial ablation |
| 7 | 30 | 10 | |
| 8 | 35 | 10 | |
| 9 | 40 | 10 | |
| 10 | 45 | 10 | |
| 11 | 50 | 10 | ablation, crystallization |
| 12 | ref. | – | broken |
| 13 | 25 | 2 | destroyed |
| 14 | 30 | 2 | destroyed |
| 15 | 35 | 2 | destroyed |
| 16 | 40 | 2 | destroyed |
| 17 | 45 | 2 | destroyed |
| 18 | 50 | 2 | partial ablation |

The increased resistivity of $v = 5$ mm/s compared to $v = 10$ mm/s between $I = 30$ A and $I = 40$ A may have occurred because all samples processed at $v = 5$ mm/s were situated closer to the sample edge than those processed at

$v = 10$ mm/s. As a result, the initial resistivity could have been lower for all samples treated with $v = 10$ mm/s than for $v = 5$ mm/s. A decrease of the resistivity is observed for $v = 5$ mm/s at $I = 45$ A, indicating that $v = 2$ mm/s would lead to even lower resistivities. Unfortunately, the initial samples processed at $v = 2$ mm/s were destroyed during the laser ablation of the electrical isolation lines.

Table 8.2: List of samples and the corresponding treatment parameters as well as the state of those samples

| sample ID | I [A] | v [mm/s] | comment |
|-----------|---------|------------|-----------|
| 1 | 46 | 2 | |
| 2 | 47 | 2 | ablation |
| 3 | 46 | 2 | |
| 4 | 45 | 2 | |
| 5 | 45 | 2 | |
| 6 | 45 | 2 | |
| 7 | – | – | reference |
| 8 | 45 | 2 | |
| 9 | 44 | 2 | |
| 10 | 44 | 2 | |
| 11 | 44 | 2 | crack |
| 12 | – | – | reference |
| 13 | 43 | 2 | |
| 14 | 43 | 2 | |
| 15 | 43 | 2 | |
| 16 | 42 | 2 | |
| 17 | 42 | 2 | crack |
| 18 | 42 | 2 | crack |
| 19 | – | – | reference |
| 20 | 41 | 2 | |

Based on the results of $v = 5$ mm/s further experiments were conducted at a scanning velocity of $v = 2$ mm/s at laser diode currents ranging from 40 A to 45 A (Fig. 8.6, red squares). The parameters of this laser treatment are listed in Table 8.2. Figure 8.6 shows a significant improvement in the resistivity ρ with

decreasing scanning velocity. Thus, all further experiments on glass substrates with $\lambda = 532$ nm were conducted at $v = 2$ mm/s. Here, repeated treatments were performed with equal parameters. The influence of the laser treatment on the resistivity, Hall mobility, carrier concentration, and Raman crystallinity is presented in detail in the following.

Influence of the Laser Treatment with 532 nm on the Crystallinity of p-type $\mu\text{-Si:H}$

First, the influence of this laser treatment on the Raman crystallinity X_C was determined according to Section 3.3.1. The dependence of the applied laser diode current, for a constant velocity of $v = 2$ mm/s, on X_C was determined as described in Section 3.3.1.

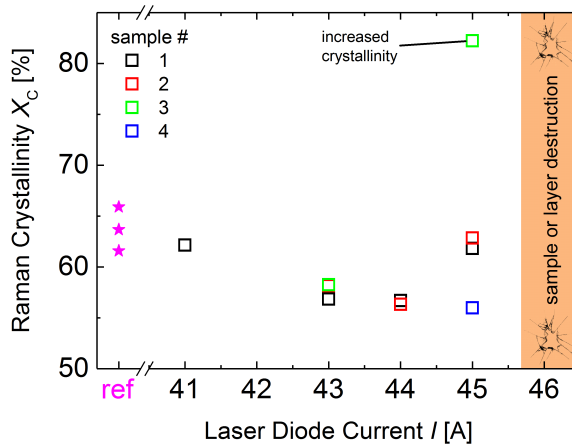


Figure 8.7: Influence of the laser diode current on X_C of p-type $\mu\text{-Si:H}$ due to the laser treatment with a line shaped beam profile and a wavelength of $\lambda = 532$ nm. The open squares refer to the treated samples (# 1 to # 4) while the pink stars refer to untreated references.

The crystallinity of the individual samples is shown in Figure 8.7. In general, the crystallinity is not influenced by the laser treatment. Nevertheless, one of the four samples treated at $I = 45$ A reveals a higher crystallinity. However, this sample was placed close to a mounting clamp during the deposition process. An influence of this clamp on the crystallinity cannot be excluded. In addition,

the individual samples were not characterized before the laser treatment but compared with as-deposited references. As a consequence, it cannot be ruled out that the Raman crystallinity of the sample with a crystallinity of $X_C > 80\%$ was not elevated before the laser treatment. Nevertheless, the treatment was performed close to the crystallization threshold. Hence, small variations of either the laser power or the characteristics of the p-type $\mu\text{-Si:H}$ thin-film can result in an increased Raman crystallinity.

Impact on the Electrical Properties

Using the PhysTech[®] RH2030 Hall measurement setup as described in 3.2.3, the influence of this laser treatment on the resistivity, the Hall mobility, and the carrier concentration was investigated. These measurements were performed in up to four subsequent runs without changing the contact position.

The results are presented in Figure 8.8. The different colors for the same current refer to individual samples that were treated with equal laser parameters. The squares refer to the treated samples while the pink stars refer to untreated reference samples. The error bars arise from subsequent measurements of the same sample without recontacting. Currents higher than 45 A led either to ablation or crystallization of the p-type $\mu\text{-Si:H}$ thin-film.

Resistivity Figure 8.8 a) presents the influence of the laser diode current on the resistivity of p-type $\mu\text{-Si:H}$ for a velocity of $v = 2\text{ mm/s}$. Here, the laser diode current was varied between 41 A and 45 A. The resistivity decreases with increasing laser diode current. As a result of this laser treatment, the resistivity was reduced by a factor of 20 from the initial resistivity $\rho_{\text{initial}} = (0.199 \pm 0.015)\ \Omega\text{cm}$ to $\rho_{45\text{ A}, 2\text{ mm/s}} = 0.01\ \Omega\text{cm}$.

Hall Mobility The influence of this treatment on the Hall mobility of p-type $\mu\text{-Si:H}$ is presented in Figure 8.8 b). As mentioned before, up to four samples were treated with the same laser parameters. The Hall mobility increases steadily with increasing laser diode current for the applied current range. This increase of μ_{H} is limited only by the ablation of the p-type $\mu\text{-Si:H}$ thin-film. The Hall mobility was increased by more than a factor of 6.1 from $\mu_{\text{H,initial}} = (0.71 \pm 0.03)\ \text{cm}^2/\text{Vs}$ for the as-deposited thin-film to $\mu_{\text{H}, 45\text{ A}, 2\text{ mm/s}} = (4.35 \pm 0.02)\ \text{cm}^2/\text{Vs}$ for a laser diode current of $I = 45\text{ A}$. However, the crystallinity of this sample is higher than for all other samples.

Carrier Density The carrier density increases with increasing laser diode current as shown in Figure 8.8 c). The squares show the carrier concentration of the laser

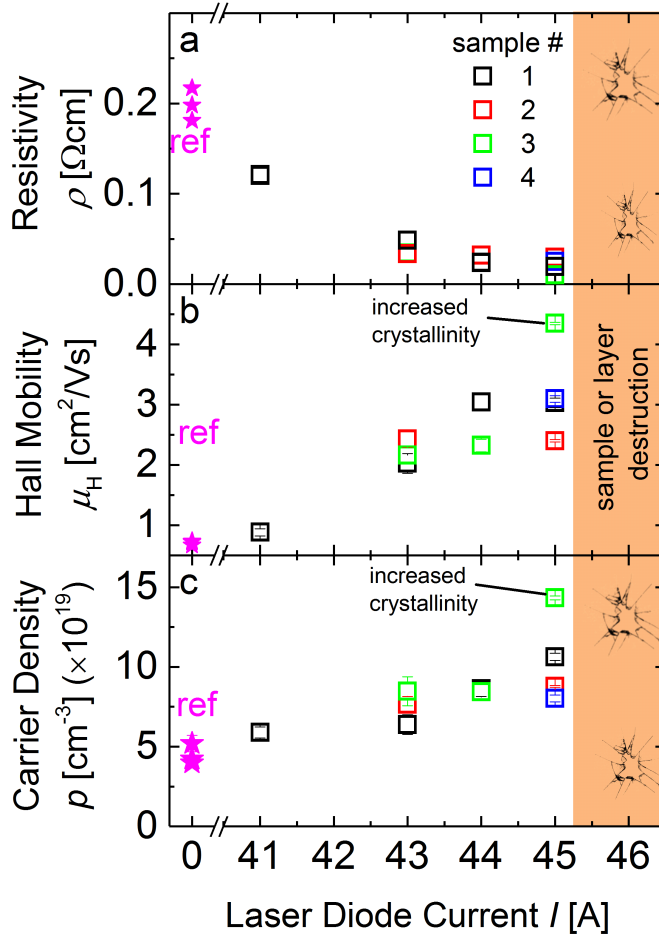


Figure 8.8: Influence of the laser diode current on a) the resistivity, b) the Hall mobility, c) the carrier density of p-type $\mu\text{-Si:H}$ for a laser treatment with a line shaped beam profile and a wavelength of $\lambda = 532$ nm. The squares refer to the treated samples while the stars refer to the untreated references. The different colors indicate individual samples (#1 to #4) that were treated with the same laser parameters. The error bar arises from subsequent measurements of the same sample without recontacting.

treated samples. The carrier density increases by a factor of 3.2 from $p_{\text{initial}} = (4.47 \pm 0.3) \times 10^{19} \text{ cm}^{-3}$ for the as-deposited p-type $\mu\text{c-Si:H}$ sample to a maximum of $p_{45\text{A}, 2 \text{ mm/s}} = (14.3 \pm 0.012) \times 10^{19} \text{ cm}^{-3}$. This best value was achieved for a scanning velocity of $v = 2 \text{ mm/s}$ and a laser diode current of $I = 45 \text{ A}$.

Summary In sum, the treatment of p-type $\mu\text{c-Si:H}$ with a scanned line shaped laser beam at a wavelength of $\lambda = 532 \text{ nm}$, a pulse duration of $\tau_{\text{pulse}} = 7 \text{ ns}$, and a repetition rate of $\nu = 40 \text{ kHz}$ improved the resistivity, the Hall mobility, and the carrier concentration. This improvement regarding the use of p-type $\mu\text{c-Si:H}$ as contact material is feasible without increasing the crystallinity. An increased crystallinity will of course influence the electrical parameters. Therefore, it was attempted to achieve a laser treatment without increasing the crystallinity in order to validate the influence of the laser treatment on μ_{H} , p and ρ . Nevertheless, for the use of p-type $\mu\text{c-Si:H}$ as contact layer, an increased crystallinity is not obstructive. The best results were achieved for the most intense treatment with a scanning velocity of $v = 2 \text{ mm/s}$ and a laser diode current of $I = 45 \text{ A}$, reducing the resistivity by a factor of 20. However, a further increase of the treatment intensity leads to the destruction of the samples.

It should be noted that a measurement instability occurred for the Hall mobility and the carrier density that has not been observed on other samples before. This is described in Chapter 3 Section 3.2.3. Here, the initial measured values are restored after waiting or re-contacting. The resistivity is not subject to the measurement instability. Consequently, this parameter can be used to compare the results of the laser treatment of p-type $\mu\text{c-Si:H}$ on glass and the measurement instability has no impact on the results of this work.

8.1.3 Laser Treatment of p-type $\mu\text{c-Si:H}$ with 355 nm with a Gaussian Beam Shape

In this subsection, the influence of a laser treatment with $\lambda = 355 \text{ nm}$ on p-type $\mu\text{c-Si:H}$ on glass substrates is analyzed. Analogous to Section 8.1.2, the impact of the laser treatment with $\lambda = 355 \text{ nm}$ on the resistivity, the Hall mobility, and the carrier density of p-type $\mu\text{c-Si:H}$ on glass is evaluated. Here, a pulsed uv laser with a wavelength of $\lambda = 355 \text{ nm}$, a pulse duration of $\tau_{\text{pulse}} = (7.2 \pm 1.8) \text{ ns}$, a repetition rate of $\nu = 15 \text{ kHz}$ and a spot diameter of $d_{\text{focus}} = 30 \text{ }\mu\text{m}$ was used. In contrast to the laser used in the previous section this laser has a circular-like beam shape. In order to prevent the ablation of the p-type $\mu\text{c-Si:H}$ thin-film, the laser power was reduced with a half-wave plate and the laser was defocused by $z = 10 \text{ mm}$. This defocusing results in a beam diameter of $d_{z=10 \text{ mm}} = 75 \text{ }\mu\text{m}$. In this section, the laser treatment was performed with an average power of $P_1 = 150 \text{ mW}$ and

$P_2 = 100$ mW. Taken into account the results of Section 8.1, the laser treatment was performed through the glass side in order to minimize reflection losses. The laser setup is described in detail in Chapter 4, Section 4.2.

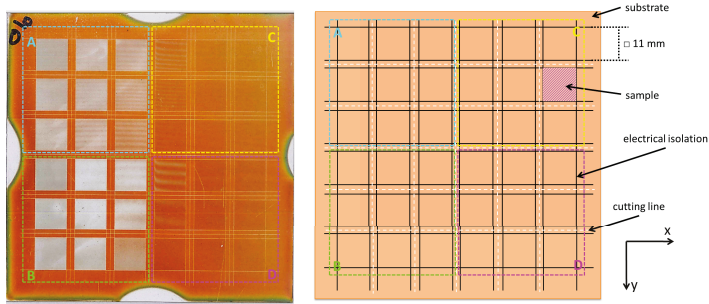


Figure 8.9: Left: image of a 10×10 cm² substrate with a p-type $\mu\text{-Si:H}$ thin-film after laser treatment with $\lambda = 355$ nm. Right: Layout for laser treatment of p-type $\mu\text{-Si:H}$ with $\lambda = 355$ nm. The solid black lines show the previously laser ablated electrical isolation lines, while the dashed white lines refer to cutting lines. Each square has a size of 11×11 mm. The four differently colored squared mark different parameter ranges. As for the treatment on the right hand side a laser power of $P_2 = 100$ mW (A, B) was applied, while on the left hand side the laser power was $P_1 = 150$ mW (C, D), respectively.

Treatment Details

In a first step, as for the previous experiments, the electrical isolation lines and the marking lines for the separation of the individual samples after the treatment were ablated (Fig. 8.9). Again, the individual samples have a size of 11×11 mm².

The scheme of the layout of the whole substrate is sketched in Figure 8.9 on the right hand side. In contrast to the laser treatment with $\lambda = 532$ nm, the treatment was performed only within the electrically isolated square samples as illustrated in Figure 8.10. In both figures the solid black lines refer to the ablated electrical isolation lines while the dashed white lines indicate the lines for glass cutting after the laser treatment. The cutting of the substrates is required for the electrical characterization, as the whole substrate exceeds the maximum sample size. Four different parameter ranges are marked in Figure 8.9 by the dashed, colored squares. For the treatment on the right hand side a laser power of $P = 100$ mW (Fig. 8.9 A, B) was applied, while on the left hand side the laser power was $P = 150$ mW (Fig. 8.9 C,D), respectively.

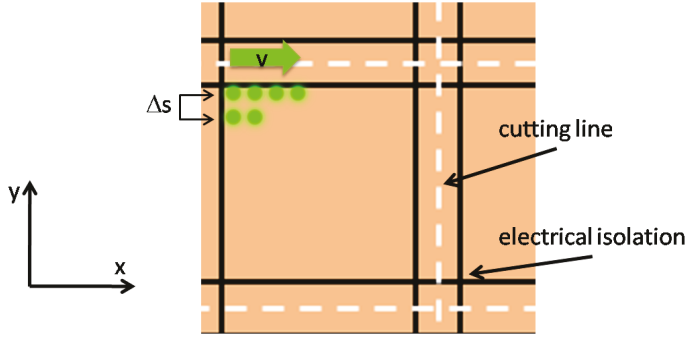


Figure 8.10: Scheme for laser treatment of p-type $\mu\text{c-Si:H}$ with $\lambda = 355 \text{ nm}$ with a Gaussian beam shape. The scanning velocity \vec{v} sets the displacement in x-direction while the shift in y-direction is controlled by the line displacement Δs .

The line displacement Δs (Fig. 8.10) amounted $\Delta s = 0.05 \text{ mm}$ for the upper part (A, C) and $\Delta s = 0.025 \text{ mm}$ for the bottom part (B, D). Within each of those four squares, the scanning velocity v ranged from $v = 20 \text{ mm/s}$ to $v = 400 \text{ mm/s}$. Two substrates from the same deposition run (Sec. 8.1) were treated for each laser parameter set. The picture of one treated substrate shows that the laser power of $P = 150 \text{ mW}$ led to the ablation of the p-type $\mu\text{c-Si:H}$ thin-film, destroying these samples (Fig. 8.9, left; A, B). The influence of this laser treatment on ρ , μ_{H} and p is presented for the remaining samples of one substrate (substrate no. 7, Fig. 8.2) in the following.

Table 8.3: List of sample classification and the corresponding treatment parameters as well as the state of those samples.

| parameter set | P [mW] | Δs [mm] | v [mm/s] | state |
|---------------|----------|-----------------|----------------------|---------|
| A | 150 | 0.050 | $20 \leq v \leq 400$ | ablated |
| B | 150 | 0.025 | $20 \leq v \leq 400$ | ablated |
| C | 100 | 0.050 | $20 \leq v \leq 400$ | ok |
| D | 100 | 0.025 | $20 \leq v \leq 400$ | ok |

Impact on the Electrical Properties

As for the treatment with 532 nm, the PhysTech RH2030 Hall measurement system, as described in Section 3.2.3, was used to study the influence of the laser treatment.

Up to four subsequent measurements were performed without changing the contact position. The results are presented in Figure 8.11 (a-c). In this subsection all graphs have equal symbols for equal laser treatment. The black symbols correspond to the line displacement of $\Delta s = 0.025$ mm, while the red symbols correspond to $\Delta s = 0.05$ mm, and the violet stars refer to as-deposited references. The parameter range with a significant improvement is indicated in each graph with a blue rectangle in Figure 8.11. However, it has to be noted that the reference samples for the treatment with $\lambda = 355$ nm originate from another substrate (substrate no.4, Fig. 8.2).

Resistivity Figure 8.11 a) shows the influence on the resistivity. The resistivity decreases steadily with decreasing scanning velocity for both line displacements $\Delta s = 0.025$ mm (black dots) and $\Delta s = 0.005$ mm (red squares). The line displacement of $\Delta s = 0.025$ mm led to lower resistivities than $\Delta s = 0.05$ mm, supporting the theory that a more intense treatment leads to better material quality. For scanning velocities $v \leq 60$ mm/s, the resistivity ρ was reduced by a factor of 3.75 compared to the reference sample. The lowest resistivities were measured for $v = 20$ mm/s with $\rho = 0.024$ Ωcm for $\Delta s = 0.025$ mm and $\rho = 0.024$ Ωcm $\Delta s = 0.05$ mm.

Hall Mobility Figure 8.11 b) shows the effect of the laser treatment with 355 nm on μ_{H} . The Hall mobility increases steadily with decreasing velocity. As noted for the resistivity, the smaller line displacement leads to a stronger improvement, from which it can be concluded that μ_{H} increases with increasing laser treatment intensity. The laser treatment intensity refers to a combination of laser power and number of dots per inch. In contrast to the resistivity, the measured Hall mobilities show a scattering that can be traced back to the measurement instability.

Analogous to the resistivity results, the Hall mobility was improved for scanning velocities $20 \text{ mm/s} \leq v \leq 60 \text{ mm/s}$ (Fig. 8.11 b, blue box). The highest Hall mobility was obtained for a line displacement of $\Delta s = 0.025$ mm and a velocity of $v = 20$ mm/s with $\mu_{\text{H}} = 1.84 \text{ cm}^2/\text{Vs}$. Here, μ_{H} was improved by a factor of 2.8 compared to the reference.

Carrier Density Figure 8.11 c) presents the influence of the laser treatment with $\lambda = 355$ nm on the carrier density. Similarly to the resistivity and the Hall mobility, the carrier density improved only for scanning velocities of 20 mm/s

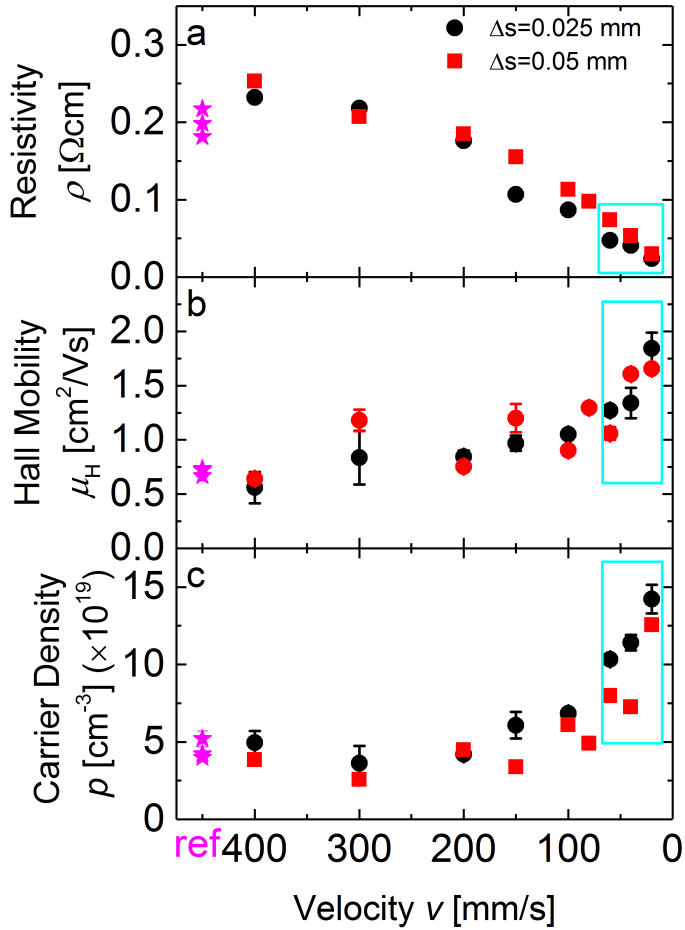


Figure 8.11: Influence of the scanning velocity on a) the resistivity, b) the Hall mobility, and c) the carrier density of p-type $\mu\text{c-Si:H}$ for the treatment with a $\lambda = 355$ nm circular-shaped laser beam. Black dots refer to a line displacement of $\Delta s = 0.025$ mm and red squares to $\Delta s = 0.05$ mm (see Fig. 8.10), respectively. The error bars result of subsequent measurements of the same sample. The untreated references are illustrated with the pink stars. The blue square indicates the region of significant improvement.

$\leq v \leq 60$ mm/s. The carrier density increased from $p = (4.47 \pm 0.3) \times 10^{19}$ cm³ of the reference by a factor of 3.45 to $p = (14.2 \pm 0.09) \times 10^{19}$ cm³ for the best sample.

Summary According to the fact, that the resistivity ρ is not influenced by the measurement instability, μ_{H} must decrease when the carrier density p increases and vice versa. The initial values of the Hall mobility and the carrier density are recovered after waiting or re-contacting the samples. As the results of the treatment with the $\lambda = 532$ nm laser exhibited a lower resistivity and a smaller measurement instability than with the $\lambda = 355$ nm laser, the Raman crystallinity has not been analyzed for the samples treated with $\lambda = 355$ nm. The results of both laser treatments will be compared in detail in the following (Sec. 8.1.4).

8.1.4 Discussion

The influence of laser treatment on p-type $\mu\text{-Si:H}$ was investigated. Two different short pulse laser sources were used for the laser treatment. The first laser source has a wavelength of $\lambda = 532$ nm, featuring a line shaped beam profile, while latter has as wavelength of $\lambda = 355$ nm with a circular beam profile. The influence of the laser treatment on the resistivity, the Hall mobility, and the carrier density of p-type $\mu\text{-Si:H}$ was analyzed for both laser sources. The exemplary results are listed in Table 8.4, and the best values are highlighted.

Table 8.4: Best results of the individual laser treatment of p-type $\mu\text{-Si:H}$ with $\lambda = 532$ nm and $\lambda = 355$ nm. The best values achieved overall are highlighted.

| | ρ [Ω cm] | μ_{H} [cm^2/Vs] | p [$\times 10^{19}$ cm ⁻³] | parameter |
|--------------|-----------------------|--|---|--|
| as-deposited | 0.199 ± 0.015 | 0.71 ± 0.032 | 4.47 ± 0.30 | as-deposited |
| 532 nm | 0.01 | 4.35 ± 0.021 | 14.3 ± 0.096 | $v = 2$ mm/s; $I = 45$ A |
| 355 nm | 0.024 | 1.84 ± 0.144 | 14.2 ± 0.09 | $v = 20$ mm/s; $\Delta s =$ 0.025 mm |

The lowest resistivity and the highest mobility were achieved using the 532 nm laser, while the highest carrier density is competitive for both wavelengths and the difference lies within the error margin. The measurement instability of μ_{H} and p are less pronounced for $\lambda = 532$ nm compared to $\lambda = 355$ nm.

Here, the electrical properties of p-type $\mu\text{-Si:H}$ on glass are in general modified without influencing X_C for the treatment with $\lambda = 532$ nm. However, the influence on the crystallinity was not investigated for the samples treated with $\lambda = 355$ nm. An increase of the crystallinity was not observed save for one of the samples treated with $I = 45$ A. Therefore, the improvement of the electrical properties can be ascribed to a modification of the amorphous tissue and to defect passivation on the grain boundaries of $\mu\text{-Si:H}$ [144–146].

The decrease of ρ upon annealing has been investigated before. This is deduced to the de-passivation of the dopands due to hydrogen reduction [145–148]. In Chapter 7, the influence of laser treatment on the hydrogen concentration and therewith the movement of hydrogen in the amorphous network has already been proofed. As a matter of fact, intense irradiation amplifies the diffusion of hydrogen even at low process temperatures and within a time scale of several seconds.

Finger et al. [147] observed an increase of the conductivity by a factor of 2 – 5 for furnace annealing up to 320 °C, while in this work the conductivity could be increased by a factor of 20. The increase of the conductivity in the work of Finger is attributed to material with only a small amount of amorphous tissue. In this work, the conductivity increased, as a result of the laser treatment, without an augmentation of the Raman crystallinity.

Here, the decrease of the resistivity can be assigned to two major factors. First, the de-passivation of dopands which increases the free carrier density. Second, structural relaxation and annealing of defects at grain boundaries and in amorphous tissue lead to the reconstruction of the amorphous network. This is considered to be the dominant process upon annealing in amorphous tissue [146, 149]. Indeed, defect passivation and dopand activation (=dopand de-passivation) are assumed to play the major role for the reduced resistivity in these experiments [146–148]. In addition, this is supported by the experiments of Winer et al. They found that the conductivity of intrinsic a-Si:H does not increase upon annealing and therefore other effects than the degree of crytallinity must also contribute to changes in the conductivity [145].

It has already been reported, that μ_H increases with increasing laser intensity [144, 145, 148]. According to the results of Matsumura et al. [150], the mobility increases with increasing crystallinity due to a better crystalline quality inside the grains. However, in this work the mobility improves without increasing crystallinity. It is considered as unlikely that the improved mobility results from a better crystalline quality inside the grains. In fact, it is rather assumed that μ_H increases due to lower potential barriers at the grain boundaries as a result of the laser treatment [149, 150].

Based on the results of this section, the laser with a wavelength of $\lambda = 532$ nm was chosen for the application of the treatment of p-type $\mu\text{-Si:H}$ on c-Si wafers. This will be described and evaluated in section 8.2.

8.2 p-type $\mu\text{-Si:H}$ on c-Si Substrates

In this section, the impact of the laser treatment on p-type $\mu\text{-Si:H}$ on c-Si wafers is analyzed. Hereby, the influence of the laser treatment on the sheet resistance R_{sh} of the p-type $\mu\text{-Si:H}$ layer as well as on the PL intensity I_{PL} and lifetime τ_{PL} of the whole sample is studied. Taken into account the results of Section 8.1.2 to Section 8.1.3, the setup of Section 8.1.2 was used for the treatment of p-type $\mu\text{-Si:H}$ on c-Si wafers. The temperature was monitored during the laser treatment with an IPE 140 pyrometer. A detailed description of the temperature measurement is given in Chapter 5.

Section 8.2.1 describes the samples as well as their fabrication process. The results of preliminary experiments to determine a suitable parameter range and reasonable treatment parameters are presented in this section, too.

Section 8.2.2 analyzes the impact of the laser treatment on R_{sh} of p-type $\mu\text{-Si:H}$. Section 8.2.2 presents the influence of the laser treatment on the PL lifetime. In addition, the influence of the laser treatment on the wafer passivation quality is compared to furnace annealed samples. The most important findings of this part of the thesis are summarized and discussed in Section 8.2.3.

8.2.1 Experiments

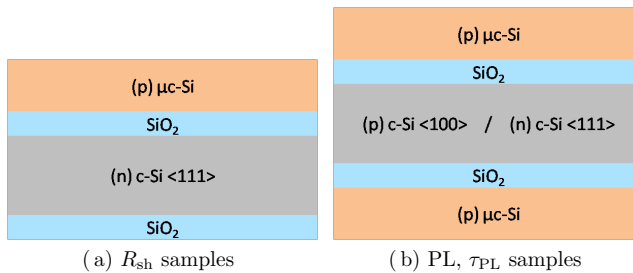


Figure 8.12: Sketch of the samples as used for a) the preliminary experiments to determine a parameter range and b) for the determination of the PL lifetime p-type c-Si, and to measure R_{sh} n-type c-Si was used.

Sample Fabrication

Fistly, the native oxide on the wafer surface was removed with a HF-dip. The tunnel oxide layer was wet-chemically grown in nitric acid (69.5 % HNO_3 , room temperature) for 10 minutes. This results in a 1.4 nm thin SiO_2 film [11]. Next, a p-type $\mu\text{c-Si:H}$ layer was deposited by PECVD. The same deposition parameters as for $\mu\text{c-Si:H}$ on glass substrates (Sec. 8.1) were applied for all depositions in this section. In a first step, a p-type $\mu\text{c-Si:H}$ layer was deposited on one side of a n-type wafer for the samples used to determine a process window (Fig. 8.12 a). For all subsequent experiments p-type $\mu\text{c-Si:H}$ was deposited by PECVD on both sides of n-type wafers for the determination of R_{sh} and on p-type wafers for the determination of τ_{PL} and I_{PL} (Fig. 8.12 b). The thickness of these p-type $\mu\text{c-Si:H}$ layers varies between 38 nm and 45 nm. Here, the thickness was determined with SE as described in Section 3.1. The fabrication process flow is presented in Table 8.5.

Table 8.5: Process flow of the fabrication process for p-type $\mu\text{c-Si:H}$ on c-Si samples

| step # | process | time [min] | comment |
|--------|-------------------------------|------------|------------------|
| 1 | HF, 1 % | 2 | room temperature |
| 2 | HNO_3 , 69.5 % | 10 | room temperature |
| 3 | $\mu\text{c-Si:H}$ deposition | | top side |
| 4 | $\mu\text{c-Si:H}$ deposition | | bottom side |

Temperature and Damage Threshold

In a first step, the damage threshold of c-Si wafers as well as the threshold for heating ($T \geq 100$ °C) was determined for the laser treatment. The reflectance R was determined corresponding to Section 3.3.3 for both c-Si and p-type $\mu\text{c-Si:H}$ on c-Si with $R_{\text{c-Si}} = 42$ % and 37 % $\leq R_{\mu\text{c-Si, c-Si}} \leq 38.4$ %. As the reflectance is similar for both, the threshold for heating and the destruction of c-Si wafers can be transferred to the samples with a p-type $\mu\text{c-Si:H}$ thin-film. Hereby, the scanning speed was varied between $v = 1$ mm/s and $v = 10$ mm/s while the laser diode current ranged from $I = 25$ A to $I = 52$ A. It was found that the local temperature increases steadily with the scanned distance for all applied parameters. Moreover, the temperature gradient of the individual scans increases with increasing scanning speed. This temperature gradient was more pronounced

towards the starting point of the scan and in proximity of the edge of the wafer. Beneficial to obtaining areas with more homogeneous treatment conditions, the laser treatment was performed at a scanning velocity of $v = 1$ mm/s.

Here, the damage threshold is defined as a visible modification of the c-Si wafer. The first visible modification at $v = 1$ mm/s was found for a laser diode current of $I = 44$ A. The heating threshold for a temperature above $T = 100$ °C lies between $I = 35$ A, where no heating was detected and $I = 38$ A, with a maximum temperature of $T = 204$ °C.

As a result of the experiments on bare c-Si wafers, the current range between $I = 35$ A and $I = 44$ A with a scanning velocity of $v = 1$ mm/s will be analyzed in detail in order to determine a suitable process window for detailed analysis. Therefore, samples with a p-type $\mu\text{-Si:H}$ thin-film on the irradiated side of the c-Si wafer will be used.

Process Window

As a result of the experiments on bare c-Si wafers, first laser treatments were performed at $v = 1$ mm/s with laser diode currents ranging from $I = 35$ A to $I = 44$ A in order to determine a suitable process window for detailed analysis. The threshold for the modification of the thin-film, as well as for the destruction of the p-type $\mu\text{-Si:H}$ layer are thereby of interest. The sheet resistance is used as an indicator for the modification of the p-type $\mu\text{-Si:H}$ layer, while steady state PL images are used to detect the destruction of the wafer passivation. Beneficial to more uniform treatment conditions, each treatment position was scanned in both directions, as illustrated in Figure 8.13. In a first step, the scan was performed from top to flat of the wafer and in a second step vice versa. The four individual treatments are marked with the numbers 1 to 4. They correspond to different applied laser diode currents. The scanning direction and position is indicated with the green arrow.

Sheet Resistance In order to measure the sheet resistance of a thin-film on a semiconductor, a different type of doping for the substrate is necessary. The combination of a p-type layer and a n-type substrate builds up a diode and the current flow (due to the measurement of the sheet resistance) is limited to the thin-film. Here, n-type $\langle 111 \rangle$ substrates were used. On the basis of the reduction of the resistivity of p-type $\mu\text{-Si:H}$ on glass substrates (see Section 8.1), the impact of the laser treatment on the sheet resistance is used as a qualifier.

The sheet resistance was measured four times subsequently using the setup described in Section 3.2.2. Hereby, the contacts were removed and recontacted between the subsequent measurements. A current of $I = 3.2$ mA was applied

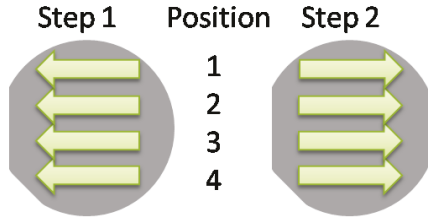


Figure 8.13: Scheme of the laser treatment for the preliminary experiments. In a first step, the scan was performed from top to the flat of the wafer and in a second step vice versa. Four individual treatments were made and are marked with the numbers 1 to 4. They correspond to the different laser diode currents applied. The green arrows indicate the scanning direction and position.

to the current-carrying contacts. The resulting sheet resistance and the corresponding process temperatures are listed in Table 8.6. Here, T_1 and T_2 are the maximum measured temperatures of the first and second scan, respectively. The average temperature T_{avg} is the mean value of T_1 and T_2 . Table 8.6 shows that the sheet resistance decreased with increasing treatment intensity and was reduced by up to 56 % for $I = 44$ A.

In addition, it was found that the temperature exhibits a strong dependence on both, the scanning direction and the position (1-4) on the wafer. As a consequence, the position of the laser treatment as well as the length of the treated surface were optimized for further experiments. The temperature depending on the treatment position after the optimization can be found in Appendix A (Fig. A.1 and Fig. A.2).

PL Measurements Steady state PL images were taken as a reference before the laser treatment of all samples as described in Section 3.4, to find whether the laser treatment influences the passivation quality. As only one side of these samples was coated with p-type $\mu\text{c-Si:H}$, the passivation of this bare side is too poor to extract a lifetime. Therefore the PL intensity was used to estimate the impact of the laser treatment on the passivation quality.

Figure 8.14 shows the PL intensity before and after the laser treatment. The passivation quality decreased considerably for $I \geq 40$ A (Fig. 8.14 b). An improvement of the PL intensity was not achieved here (Fig. 8.14 a). The average decrease of the PL intensity over the treated surface is listed in Table 8.6.

Table 8.6: Influence of the laser treatment with $v = 1$ mm/s on the sheet resistance. The reduction of the sheet resistance compared to as-deposited samples is shown depending on the applied laser diode current and the maximum process temperature.

| I [A] | T_1 [°C] | T_2 [°C] | T_{avg} [°C] | R_{sh} [%] | position | PL int. [%] |
|---------|------------|------------|-----------------------|---------------------|----------|-------------|
| 35 | 139 | 130 | 135 | -12 | 1 | 0 |
| 37 | 171 | n.a. | n.a. | -9 | 2 | 0 |
| 39 | 326 | 211 | 269 | -43 | 3 | 0 |
| 40 | 442 | 390 | 416 | -55 | 4 | -16 |
| 40 | 485 | 288 | 387 | -54 | 3 | -1 |
| 42 | 488 | 631 | 560 | -55 | 1 | -46 |
| 43 | 739 | 544 | 642 | -47 | 2 | -45 |
| 44 | 667 | 594 | 631 | -56 | 4 | -77 |

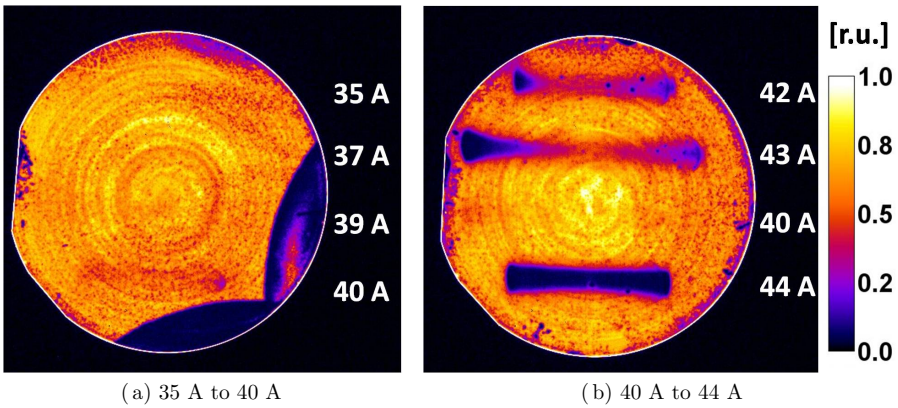


Figure 8.14: PL intensity image after the laser treatment with a) $35 \text{ A} \leq I \leq 40 \text{ A}$ and b) $40 \text{ A} \leq I \leq 44 \text{ A}$. The passivation is damaged for $I \geq 40 \text{ A}$.

Summary As a result of the PL images, the current was limited to 40 A for all subsequent experiments with symmetrical samples (see Fig. 8.12 b). Further experiments were operated at $I = 37$ A, $I = 38$ A, $I = 39$ A and $I = 40$ A. An improvement of the PL intensity was not achieved for these samples. However, the lowest lifetime limits the PL intensity. Taken into account that only one side of the wafer is passivated with SiO_2 and p-type $\mu\text{c-Si:H}$, the backside of the wafer limits the lifetime here. As a consequence, the reduction of the PL intensity proves, that the passivation quality was reduced at least on one side of the wafer. Though, the passivation quality of the p-type $\mu\text{c-Si:H}$ layer might be improved due to the laser treatment for a constant PL intensity. Experiments using symmetrical lifetime samples will give information about this.

Even though a positive impact on the lifetime due to the laser treatment could not be proved here, the sheet resistance was reduced by 12 % to more than 40 % without negative influence on I_{PL} for laser diode currents $35 \text{ A} \leq I \leq 40 \text{ A}$. A detailed analysis considering the impact of the laser treatment on the sheet resistance and the passivation quality is presented in the following (Sec. 8.2.2 and Sec. 8.2.2)

8.2.2 Laser Treatment of Symmetrical p-type $\mu\text{c-Si:H}$ on c-Si Substrates

Here and in the following, symmetrical samples as illustrated in Figure 8.12 b) were used. In order to analyze the passivation quality of selective contacts for rear contacts, symmetrical lifetime samples with p-type $\mu\text{c-Si:H}$ on p-type c-Si were used as described in [10–12]. However, $\mu\text{c-Si:H}$ was used instead of a-Si:H corresponding to Li [14].

Due to a more homogeneous temperature development after the position optimization and in favor of having a direct link between the temperature and the sheet resistance as well as the calibrated PL lifetime, the treatment of the symmetrical samples was performed only in one direction. The temperature evolution during the laser treatment of the symmetrical samples is presented in the Appendix.

Impact on the Sheet Resistance

The sheet resistance of the symmetrical samples was measured on both the irradiated and non-irradiated side before and after the laser treatment. In order to prevent heating of the thin-film during the measurement, a current as low as $I = 1.8 \text{ mA}$ ($I = 3.2 \text{ mA}$ for the experiments to determine a parameter range) was applied to the current contacts.

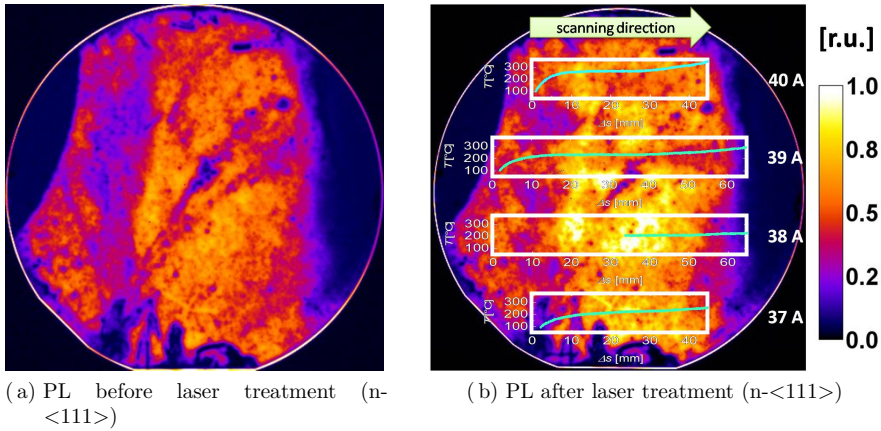


Figure 8.15: PL image (steady state) of p-type $\mu\text{c-Si:H}$ on a n- $\langle 111 \rangle$ c-Si wafer. a) before laser treatment and b) after laser treatment. The laser treated area is indicated with the white rectangles on the right hand side. The temperature depending on the position of the wafer is plotted in the rectangles.

The sheet resistance has been normalized to the average sheet resistance of all as-deposited samples. The results are presented in Figure 8.16. The measurement positions on the wafer are marked with black dots in the individual graphs and the black rectangles indicate the irradiated area on the wafer. The false color surface mapping was calculated with linear dependency out of the values retrieved from the measurements.

The graphs on the left hand side refer to the irradiated side of the wafer, while those on the right hand side refer to the non-irradiated side of the wafer. The first row shows R_{sh} of the as-deposited samples (Fig. 8.16 a, b) while the second row shows the corresponding R_{sh} after the laser treatment.

In order to obtain a similar quality of $\mu\text{c-Si:H}$ for each laser treated area, the wafer was turned by 90° for the laser treatment due to results of the PL measurements (see Fig. 8.15). Unfortunately, the treated areas do not coincide with the previously used measurement points, leading to a deviation of the treated surface and the reference measurement point before the laser treatment.

In the interest of gaining a better insight into the effect of the laser treatment on R_{sh} , the measurements after the laser treatment were performed on three different spots of each treated surface. The results are presented in the second row of Figure 8.16. For an easier reading, the irradiated areas are marked with rectangles (Fig.

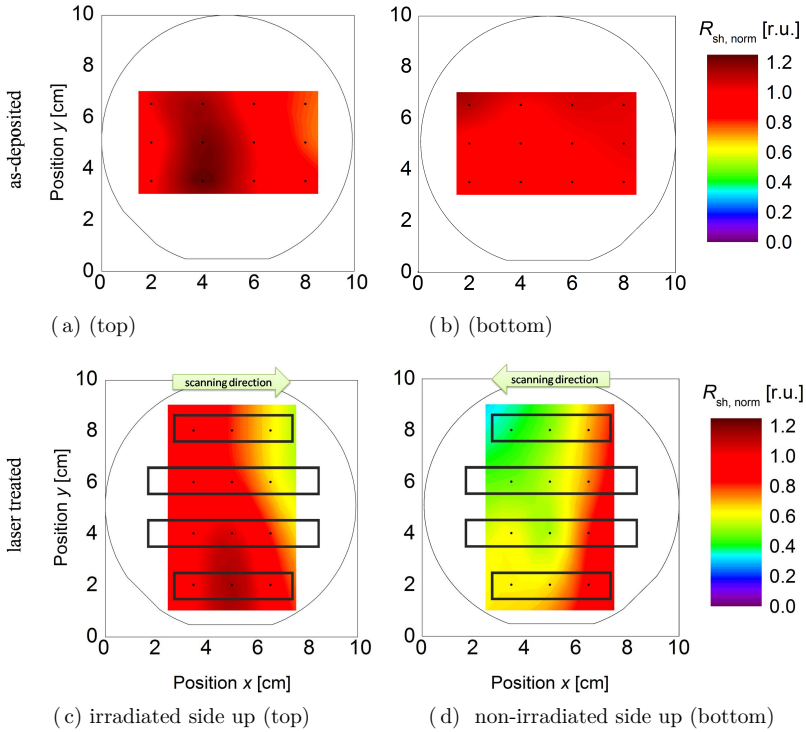


Figure 8.16: Sheet resistance of the $\mu\text{c-Si:H}$ thin film on a c-Si wafer before and after laser treatment. The rectangles indicate the irradiated area on the wafer, while the dots refer to the R_{sh} measurement points. The green arrows indicate the scanning direction for the laser treatment.

8.16 c, d). The false color mapping reveals that the sheet resistance is reduced due to the laser treatment. However, the effect is more pronounced for the non-irradiated side than for the irradiated side.

The analysis of the sheet resistance on the irradiated areas shows a decrease of the sheet resistance towards the ending point of the laser treatment. Therefore, the sheet resistance was set into relation with the local process temperature. As the outer probes used to measure the sheet resistance, have distance of 10 mm, the local process temperature was averaged over a distance of 10 mm.

The local normalized sheet resistance is plotted versus the average process temperature in Figure 8.17. In addition, the local pyrometer temperature depending

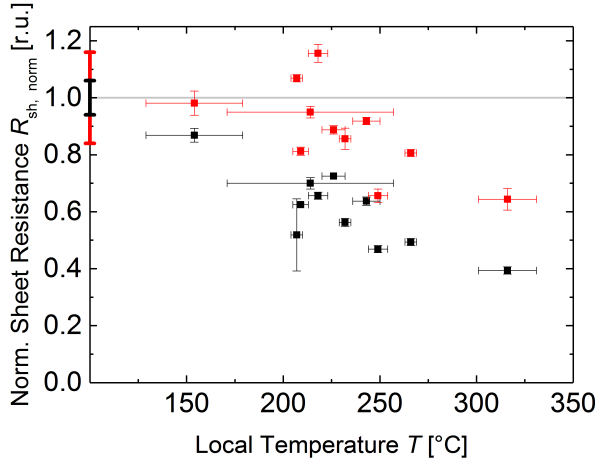


Figure 8.17: Sheet resistance depending on the local average temperature during the laser treatment. Red refers to the irradiated side, black to the non-irradiated side, respectively. The average R_{sh} for the as-deposited thin-film is indicated with the horizontal solid line. The standard deviation of the as deposited sample is shown on the left y-axis. The y-error bars show the standard deviation for R_{sh} while the x-error bars refer to the local temperature.

on the treatment position can be found in Appendix A. The y-error bars in Figure 8.17 correspond to the standard deviation of R_{sh} , while the x-error bars relate to the standard deviation of the local temperature over the distance of 10 mm, respectively. The mean R_{sh} of the as-deposited samples is equal within the measurement accuracy for both sides of the wafer. However, the assigned non-irradiated side is more homogeneous with $R_{sh} = 1.0 \pm 0.06$ (Fig. 8.17, black error bar) than the assigned irradiated side with $R_{sh} = 1.0 \pm 0.16$ (Fig. 8.17, red error bar).

A decrease of R_{sh} is indicated for $T > 200$ °C on the irradiated side. However, all measured values are still within the standard deviation of the as-deposited sample (Fig. 8.17, red) for $T < 250$ °C. The sheet resistance on the irradiated side could be reduced by as much as a factor of 1.6. Regarding the non-irradiated side, R_{sh} decreases with increasing treatment temperature (Fig. 8.17, black) for all measured points. The sheet resistance was reduced up to a factor of 2.5 on the non-irradiated side of the wafer. Thus, the reduction of the sheet resistance

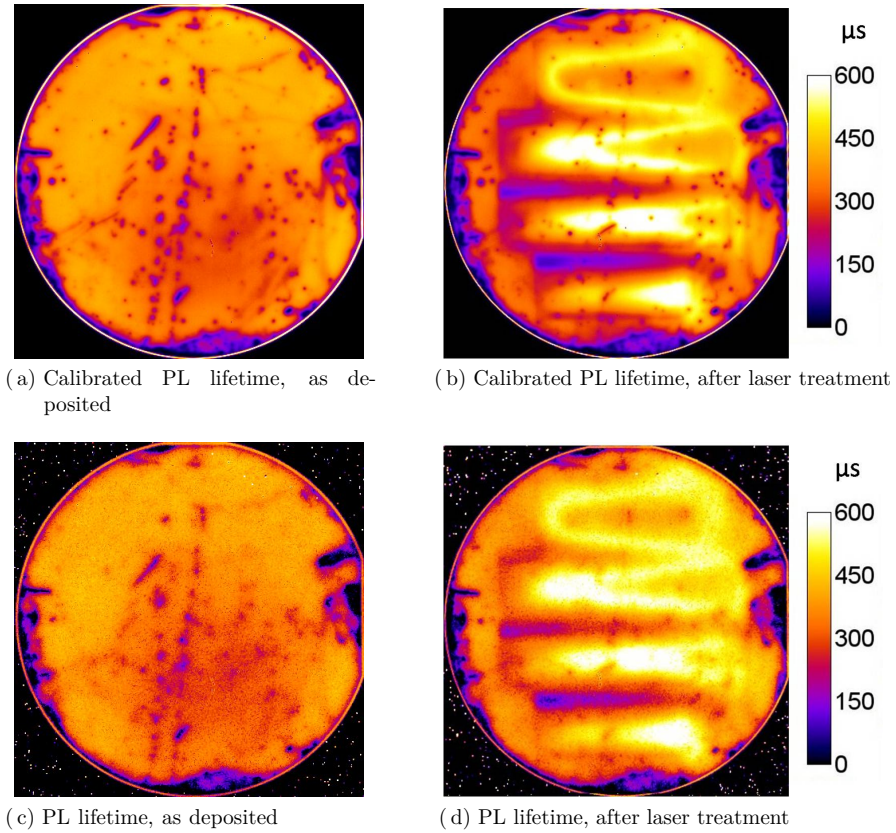


Figure 8.18: Calibrated PL lifetime (steady state) and lifetime (dynamic) images of p-type $\mu\text{c-Si:H}$ on a p-<100> c-Si wafer. The upper images (a, b) correspond to I_{PL} , while the imaged of the second row refer to τ_{PL} . The left hand side shows the images before laser treatment (a, c) and the right hand side (b, d) shows the images after the laser treatment, respectively.

turned out to be more efficient on the non-irradiated side, than on the irradiated side of the wafer for all treatment conditions.

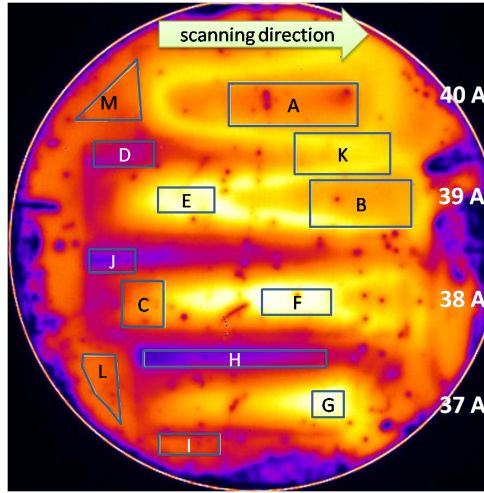


Figure 8.19: PL intensity image of p-type $\mu\text{c-Si:H}$ on a p-<100> c-Si wafer after laser treatment. The green arrow indicates the laser scanning direction. Here, the positions and the size of the analyzed areas are indicated and named (A-M). The corresponding average lifetime of these areas, before and after the laser treatment, are presented in Table 8.7.

Impact on the Passivation Quality

In the interest of qualifying the impact of the laser treatment on the passivation, PL images were taken before and after the laser treatment for p-type $\mu\text{c-Si:H}$ on p-type wafers. The steady state PL images as well as the dynamic lifetime images before and after the laser treatment are presented in Figure 8.18. In this figure, a) and c) refer to the as-deposited sample while b) and d) refer to the laser treated sample, respectively. The steady state PL images (a, b) have been calibrated to the lifetime (c, d) corresponding to Ramspeck as described in Section 3.4 [112]. The maximum lifetime $\tau_{\text{PL, max}}$ before laser treatment was found in area D, while $\tau_{\text{PL, max}}$ was found in area F after the laser treatment (see Fig. 8.19), respectively. The resulting calibration factors ($X_{\text{as-dep}}$, X_{laser}) for I_{PL} are:

$$X_{\text{as-dep}} = 0.0158, \text{ for the as-deposited wafer and}$$

$$X_{\text{laser}} = 0.0135 \text{ for the treated samples.}$$

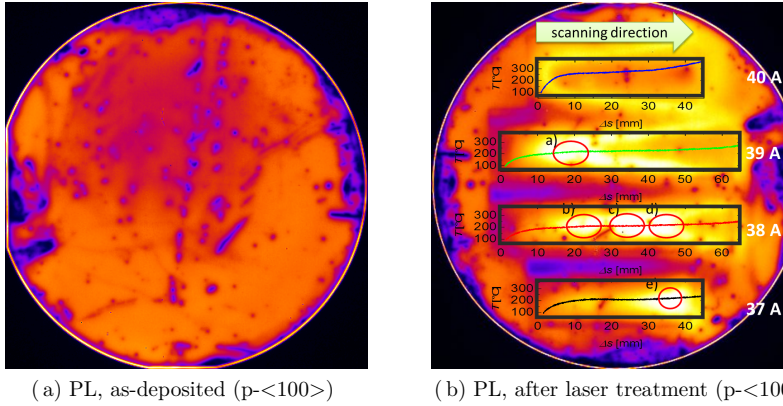


Figure 8.20: PL intensity image of p-type $\mu\text{c-Si:H}$ on a p-<100> c-Si wafer a) before and b) after laser treatment. The treated areas are indicated with the black rectangles, while the green arrow indicates the laser scanning direction b). In addition, the temperature depending on the position of the wafer is plotted inside these rectangles. The areas with the highest lifetimes achieved due to the laser treatment are indicated in b) with red circles.

The treatment direction as well as the applied laser diode current are indicated in Figure 8.20 b). The laser treated area is marked with rectangles. In addition, the temperature depending on the position of the wafer is plotted inside these rectangles. The influence of the laser treatment on the passivation is related to the local temperature. The results are presented in the following paragraphs, whereas it is distinguished between irradiated and non-irradiated areas.

Irradiated Areas Figure 8.20 and 8.19 show a strong variation of the PL intensity due to the laser treatment. The PL intensity was improved throughout the whole treated area. The relative change of the lifetime was calculated for 13 different areas on the wafer. In doing so, the lifetime has been averaged over the marked areas before and after laser treatment. These areas are indicated in Figure 8.19 and the resulting lifetime increase is listed in Table 8.7. The highest lifetimes are detected in regions where the local process temperature ranged from 200 °C to 220 °C. In this temperature range, the lifetime increased by 106 % to 135 %. The regions where these highest lifetimes are obtained are marked in Figure 8.20 b) (a-e).

Table 8.7: Relative increase [%] of the calibrated PL lifetime due to the laser treatment. The lifetime has been averaged over the marked areas for both measurements before and after laser treatment.

| position | PL lifetime [μs] as-deposited | PL lifetime [μs] laser treated | gain [%] |
|----------|---|--|----------|
| A | 388 | 374 | -4 |
| D | 409 | 227 | -45 |
| E | 329 | 581 | 77 |
| H | 304 | 164 | -46 |
| F | 294 | 591 | 101 |
| G | 316 | 593 | 88 |
| C | 331 | 360 | 9 |
| B | 377 | 453 | 20 |
| I | 338 | 293 | -13 |
| J | 400 | 169 | -58 |
| K | 400 | 502 | 25 |
| L | 393 | 324 | -18 |
| M | 406 | 328 | -19 |

Non-Irradiated Areas The lifetime decreased between irradiated areas that were treated at lower intensities (Figure 8.19 H, D). This effect is most pronounced between the treatment with $I = 37$ A and $I = 38$ A at position H. The lifetime decreased for 46 % in area H. The decrease of the lifetime between the treated areas is less distinct for the treatment with higher laser power and the corresponding increased temperature. However the lifetime decreases only slightly parallel to the area treated with $I = 37$ A without neighboring treatment, while the lifetime increases for the corresponding position treated with $I = 40$ A. Another observation is that the lifetime decreases towards the starting point of the laser treatment.

Furnace Treatment

In order to compare the quality of the laser passivation with other methods, additional samples were treated in a furnace process. This furnace process is performed under N_2 atmosphere using small heating and cooling rates. The highest

lifetimes after the laser treatment are obtained for temperatures $200\text{ }^{\circ}\text{C} \leq T \leq 220\text{ }^{\circ}\text{C}$ (Fig. 8.22). Therefore, the temperature used for the furnace annealing was adapted to this temperature range. The dedicated temperature was hold for $t = 120\text{ min}$. Due to the small temperature ramps for heating and cooling down as well as the necessity to evacuate the furnace, the process time for furnace annealing is in the order of one day.

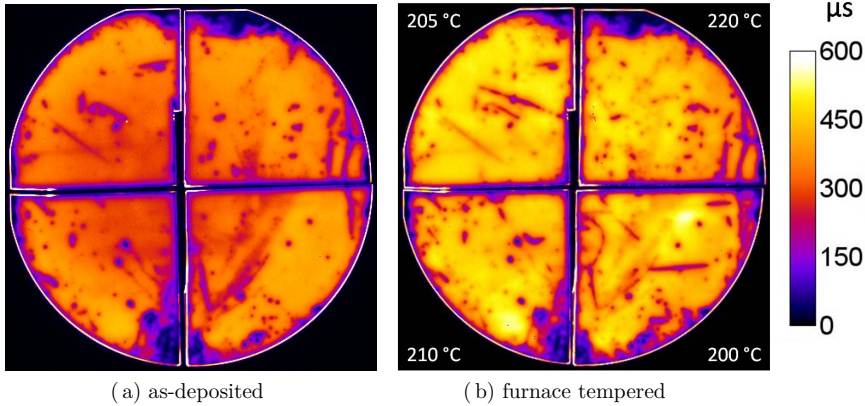


Figure 8.21: Calibrated PL lifetime images of furnace treated samples. The as-deposited samples are presented on the left-hand side a), while the annealed samples are presented on the right-hand side b). The annealing temperature of latter is indicated in the corresponding quadrant.

Calibrated PL images are presented in Figure 8.21. Please note, that the correction factors are the mean value of all four samples. The resulting calibration factors ($X_{\text{as-dep}}$, X_{annealed}) for I_{PL} are:

$$X_{\text{as-dep}} = 0.0157 \pm 0.0003 \text{ for the as-deposited samples and}$$

$$X_{\text{annealed}} = 0.0147 \pm 0.0007 \text{ for the annealed samples.}$$

The as-deposited samples are presented on the left-hand side (Fig. 8.21 a), while the annealed samples are presented on the right-hand side (Fig. 8.21 b). In addition, the annealing temperature of latter is indicated in the corresponding quadrant. The comparison of the lifetime images before and after annealing

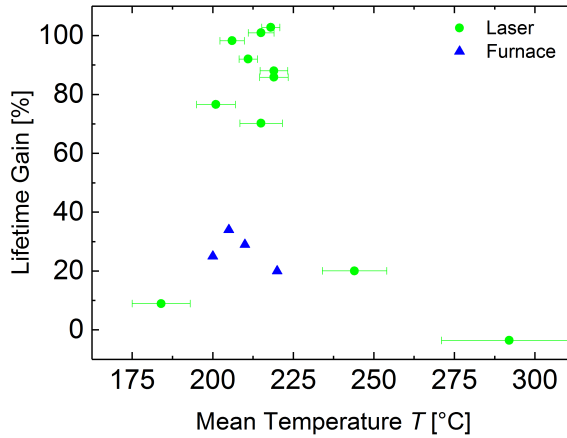


Figure 8.22: Lifetime gain depending on the process temperature. The green dots refer to the lifetime gain due to the laser treatment. The x-error bars denote the standard deviation of the mean temperature over the measurement area. The blue triangles present the results of the furnace treatment.

indicates an increase of the lifetime for all samples due to annealing. Hereby the maximum lifetime gain was achieved for the sample annealed at $T = 205$ °C with 34 %.

Figure 8.22 shows the lifetime gain depending on the local temperature for the furnace experiments (blue triangles) and selected positions from the laser experiments (green dots). The local temperature and the local lifetime are obtained corresponding to Figure 8.19 (A, B, C, E, F, G) and five additional positions with the highest lifetimes. The error bar for the temperature due to the laser treatment comes along with the variation of the temperature in the analyzed area.

The lifetime gain due to the furnace annealing is shown with blue triangles in Figure 8.22. The highest lifetime gain of 34 % is found for $T = 205$ °C. The sample that was first annealed at $T = 200$ °C was annealed a second time at $T = 205$ °C. This second heat treatment lead to a decrease of the lifetime compared to the treatment at $T = 200$ °C.

8.2.3 Discussion

Sheet Resistance The sheet resistance decreases with increasing local process temperature due to the laser treatment. Considering R_{sh} , no upper limit for the laser power and with it the temperature, was found within the parameter range analyzed in this work. A negative impact on R_{sh} due to repetitive treatment is not observed. The results indicate that the sheet resistance decreases with a higher laser power and with the process temperature. However, the laser irradiation seems to have a negative influence on the sheet resistance here, as the relative change of R_{sh} is more elevated on the bottom side of the wafer than on the irradiated side (see Fig. 8.16, 8.17). Further experiments should be performed to proof this effect and to evaluate whether the laser wavelength has an influence.

Passivation The parameter range for an improved passivation is more delicate. The results indicate, that a treatment with a too low temperature will lead to a degradation of the passivation. This effect is most pronounced in non-irradiated areas and a repeated heating cycle (H, I, and J as presented in Table 8.7 and Figure 8.19). However, these areas were not directly exposed to the laser radiation. In contrast, the repetitive temperature increase in non-irradiated areas at a more elevated temperatures leads to an improved lifetime (e.g. K in Table 8.7 and Figure 8.19). Considering exclusively the irradiated areas, the best passivation results from areas with process temperatures between $T = 200\text{ }^{\circ}\text{C}$ and $T = 225\text{ }^{\circ}\text{C}$ (Fig. 8.22, green dots). This effect is independent of the laser power as long as the resulting temperature does not exceed the ideal range. Within the accurateness of measurement, the best passivation was obtained at the same temperature for both laser and furnace treatment. Neither the laser parameters nor the parameters for the furnace treatment are optimized. Further experiments should be conducted in order to find whether the lifetime increases for shorter treatment times in a furnace and to what extend the scanning speed influences the passivation quality for laser treated samples.

Summary and Outlook The laser treatment of p-type $\mu\text{-Si:H}$ on c-Si wafers has a positive impact on both, the sheet resistance and the minority carrier lifetime. Both attributes are important for solar cell concepts with passivated contacts. The surface recombination is reduced due to a good wafer passivation. This and low ohmic contact layers increase the efficiency of solar cells as recombination losses in the contact layer and the series resistance of the solar cell are reduced. It was found that the reduction of R_{sh} is more elevated on the non-irradiated side of the wafer. Here, the sheet resistance was reduced by a factor of up to 2.5. However, in this case the temperature was too elevated considering the passivation quality. Considering the limited range of the process temperature

from $T = 200\text{ }^\circ\text{C}$ to $T = 225\text{ }^\circ\text{C}$ that leads to an increase of the lifetime by more than a factor of 2, the sheet resistance was reduced by $35\% \pm 8\%$ on the non-irradiated side and $7\% \pm 10\%$ on the irradiated side. In contrast, the maximum lifetime gain as a result of the furnace treatment was only 34%. However, it has to be noted that neither the laser process nor the furnace process are optimized.

The fact that the laser process is conducted in atmosphere is an obvious advantage compared to the furnace process with a controlled atmosphere. The processing time for the setups used for this thesis for one 4 inch wafer are in the order of ten minutes for the laser experiments, while the furnace treatment is in the order of one day. Latter is mainly so long due to the need to build up a vacuum before the treatment and the long cooling down time. On the contrary, the laser process has the potential for shorter process times, e.g. by using a more powerful laser source with a larger laser beam size.

The laser treatment, as performed in this work, exhibits the generation of a large temperature range on a very short time scale. The perspective of finding a suitable parameter range for long time furnace annealing or even to replace those processes is one of the major advantages of laser treatment. As a consequence, this laser process should be tested for the a-Si:H passivation of heterojunction solar cells in order to find whether the best passivation quality is obtained at the same temperature for both laser and furnace processes.

9 Conclusion and Outlook

Lasers are already used in solar cell production, however rarely as a means for material modification. In this work, a-Si:H and $\mu\text{c-Si:H}$ were treated with intense laser irradiation regarding the application for thin-film solar cells as well as for hybrid solar cells.

Firstly, Raman spectroscopy was evaluated as a method for the determination of the hydrogen concentration and the microstructure parameter of a-Si:H in Chapter 6. As demonstrated before, FTIR absorption modes that are used to determine the hydrogen concentration of a-Si:H are infrared as well as Raman active. Raman spectroscopy, operated in backscattering mode, is independent on the type of substrate. Using infrared transparent substrates Raman spectroscopy was compared with FTIR absorption. It could be proven that Raman spectroscopy can be used instead of FTIR for the determination of the hydrogen concentration and the microstructure parameter with certain constraints. For Raman spectroscopy, a reference sample with known hydrogen concentration is needed for a quantitative analysis with Raman spectroscopy. On the other hand, relative changes can be easily observed by comparing the signal intensity. In the case of Raman spectroscopy, the absorption of the excitation wavelength has to be taken into account. However, this comprises the possibility for a depth-dependent analysis. Considering the microstructure parameter depending on the annealing temperature, the evolution of both the Raman and FTIR microstructure parameter are comparable. However, the values deviate from each other. This is partially attributed to the limited penetration depth of Raman spectroscopy, depending on the excitation wavelength.

In conclusion, it was demonstrated that Raman spectroscopy can be used to determine the hydrogen concentration on any substrate in backscattering mode. Furthermore, the influence on the microstructure parameter can be analyzed. Therefore, this method can be used to characterize the influence of laser treatment of a-Si:H on glass substrates on the hydrogen concentration and the microstructure. Further, Raman spectroscopy can be used to help to understand and analyze the growth process of a-Si:H, as depth dependent changes and irregularities can be detected in a thin-film at any production stage.

In Chapter 7 amorphous silicon was treated at high intensities with a short-pulse laser source at a wavelength of $\lambda = 532$ nm. The laser radiation is com-

pletely absorbed in the a-Si:H layer, heating the sample. It is beneficial to compare the results with different treatment parameters, the temperature was monitored during the treatment and cooling down with a pyrometer. The hydrogen concentration was reduced on a timescale of several seconds from initial $c_{H,0} = 14$ at.% to less than 9 at.% without impact on the electrical properties and the density of deep defects. The hydrogen concentration was found to be already reduced for process temperatures below $T = 350$ °C, where no hydrogen out-diffusion would be expected. Indeed, taken the scattering of the measurement results into account, the hydrogen concentration decreased by 15 % to 20 % for process temperatures between $T = 400$ °C and $T = 450$ °C. A significant degradation, regarding the sub-bandgap absorption, the photoconductivity and the dark conductivity was not observed for maximum process temperatures below $T = 575$ °C. For a better understanding of the results, the experiments were accompanied with FEM heat transfer and diffusion simulations. Supported by FEM simulations, the hydrogen decrease in low temperature regions can be ascribed to a light-enhanced diffusion process. This light enhanced diffusion may be a result of the metastability of a-Si:H.

Both, the use of Raman spectroscopy to qualify structural properties of a-Si:H and the post deposition laser treatment can be used for a-Si:H thin-films made of liquid hydrosilane [151, 152]. The independence on the type of substrate of Raman spectroscopy allows the characterization of the silicon thin-film at any production stage. Iyer et al. demonstrated that solution based silicon thin-films can be crystallized after a thermal annealing with laser treatment [151]. Laser enhanced annealing, as presented in this thesis, has a high potential to replace this thermal annealing step. In addition, the same laser source could be used for the subsequent crystallization.

In Chapter 8, the influence of laser treatment on $\mu\text{c-Si:H}$ was investigated. First, p-type $\mu\text{c-Si:H}$ layers were deposited on glass substrates in order to qualify the influence of the laser treatment on the resistivity, Hall mobility and carrier concentration. As a result of the laser treatment, the resistivity was reduced by a factor of 20 from initial $\rho = 0.2$ Ωcm to $\rho = 0.01$ Ωcm . Furthermore, the Hall mobility increased by a factor of 6.1 and the carrier density by a factor of 3.2. Indeed, a Hall mobility of $\mu_H = 4.35$ cm^2/Vs and a carrier density of $p = 14.3 \times 10^{19}$ cm^{-3} were obtained. For these values, the crystallinity was slightly higher than for the reference sample. This should have no negative impact considering the use as contact layer for hybrid solar cell, though the increased crystallinity has to be taken into account for the analysis of the electrical properties.

Without increase of the crystallinity, a Hall mobility $\mu_H = 2.84$ cm^2/Vs and a carrier density of $p = 9.4 \times 10^{19}$ cm^{-3} was observed. This is proof of an

improvement of the electrical properties due to a de-passivation of defects at grain boundaries and changes within the amorphous tissue. Moreover this finding is consistent with the findings of Chapter 7, where the contribution of intense laser irradiation to structural changes within a-Si:H was demonstrated.

In a next step, this process was transferred to c-Si wafers for the application as passivated contacts. Here, the influence on the sheet resistance as well as on the wafer passivation was investigated. It was found that sheet resistance decreases with increasing treatment intensity. The sheet resistance was reduced by 56 %. Indeed, within the experiments of this work, no upper limit for the laser intensity was observed for the sheet resistance. On the contrary, the passivation quality suffered from this intense laser treatment. Nevertheless, the PL lifetime was increased by up to 135 % with optimized laser process parameters, while the sheet resistance was reduced at the same time. In addition, the Hall mobility and the carrier density of laser treated p-type $\mu\text{-Si:H}$ is considerably higher than for as-deposited material.

As mobility, conductivity, and carrier density of device grade p-type $\mu\text{-Si:H}$ for tandem solar cells increased, this post-deposition laser treatment should be transferred to tandem solar cells. In addition, the laser treatment of n-type $\mu\text{-Si:H}$ has not yet been investigated. This is of interest for both, tandem solar cells and for passivated contacts. Of course, further investigations are necessary to study the influence of the laser treatment on layers that have already been deposited and on the solar cell layer stack.

It was observed, that the ideal temperature for the treatment of p-type $\mu\text{-Si:H}$ on c-Si wafers was similar for both furnace treatment and laser treatment. Consequently, the temperature gradient that arises in the laser treatment can be used to determine an ideal annealing temperature over a large temperature range in a short time. Furthermore, it should be investigated if the ideal temperature can be determined in the same manner for other material system, as for example the a-Si passivation of heterojunction solar cells.

Laser treatment of selective contacts is also of interest for industrial applications. First, the treatment was performed under ambient atmosphere and with that the processing time is drastically reduced. Taken into account the results of Chapter 7 and of Chapter 8, short-pulse laser treatment has a high potential to improve the a-Si:H passivation of heterojunction solar cells and to reduce the processing time simultaneously.

A Appendix

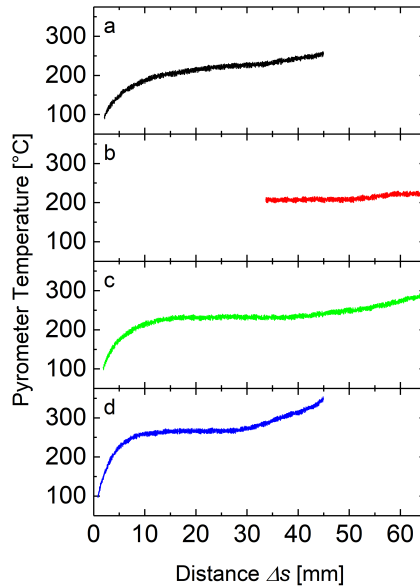


Figure A.1: Temperature evolution during the laser treatment of the n<111> $\mu\text{c-Si:H}$ on c-Si depending on the position. The treatment was performed at a scanning velocity of $v = 1$ mm/s with laser diode currents of a) $I = 37$ A (black line), b) $I = 38$ A (red line), c) $I = 39$ A (green line), and $I = 40$ A (blue line). The temperature measurement for $I = 38$ A (red) started with delay. However, it is similar to $I = 38$ A in Figure A.2. These samples were used for subsequent R_{sh} measurements. The results of the laser treatment are discussed and presented in Chapter 8, Section 8.2.

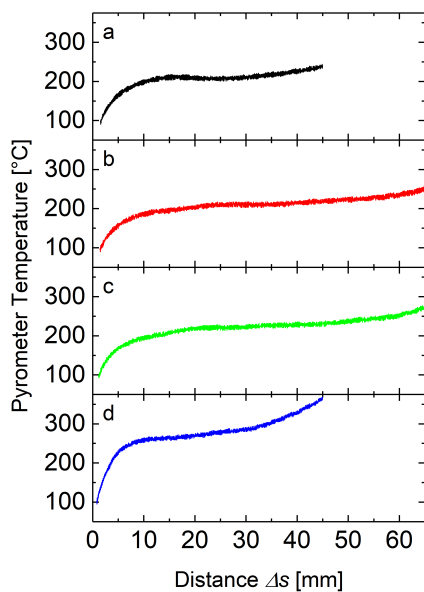


Figure A.2: Temperature evolution during the laser treatment of the p<100> μ c-Si:H on c-Si depending on the position. The treatment was performed at a scanning velocity of $v = 1$ mm/s with laser diode currents of a) $I = 37$ A (black line), b) $I = 38$ A (red line), c) $I = 39$ A (green line), and $I = 40$ A (blue line). These samples were used for subsequent PL and lifetime measurements. The results of the laser treatment are discussed and presented in Chapter 8, Section 8.2.

Bibliography

- [1] “Strom 2030.” www.bmwi.de, 2017.
- [2] “Energiewende.” Deutscher Bundestag, June 2011.
- [3] “Energiekonzept 2050,” in *Fachausschuss "Nachhaltiges Energiesystem 2050" des Forschungsverbundes Erneuerbare Energien*, June 2010.
- [4] S. Teske, O. Schäfer, A. Zervos, J. Beranek, S. Tunmore, and W. Krewitt, “energy [r]evolution. a sustainable global energy outlook.,” Greenpeace und European Renewable Energy Council, 2008.
- [5] “Current and future cost of photovoltaics. long-term scenarios for market development, system prices and lcoe of utility-scale pv systems,” *Fraunhofer ISE*, Feb. 2015. Study on behalf of Agora Energiewende.
- [6] G. Reid, “China understood solar, GE and Siemens never did and are now paying the price.” online, Nov. 2017.
- [7] S. De Wolf, A. Descoedres, C. Holman Zachary, and C. Ballif, “High-efficiency silicon heterojunction solar cells: A review,” *Green*, vol. 2, pp. 7–24, Jan. 2012.
- [8] C. Battaglia, A. Cuevas, and S. De Wolf, “High-efficiency crystalline silicon solar cells: status and perspectives,” *Energy and Environmental Science*, vol. 9, no. 5, pp. 1552–1576, 2016.
- [9] A. Richter, M. Hermle, and S. W. Glunz, “Reassessment of the limiting efficiency for crystalline silicon solar cells,” *IEEE Journal of Photovoltaics*, vol. 3, pp. 1184–1191, Oct 2013.
- [10] F. Feldmann, M. Simon, M. Bivour, C. Reichel, M. Hermle, and S. W. Glunz, “Efficient carrier-selective p- and n-contacts for si solar cells,” *Solar Energy Materials and Solar Cells*, vol. 131, pp. 100–104, 2014.
- [11] F. Feldmann, M. Simon, M. Bivour, C. Reichel, M. Hermle, and S. W. Glunz, “Carrier-selective contacts for si solar cells,” *Applied Physics Letters*, vol. 104, no. 18, 2014.

- [12] F. Feldmann, M. Bivour, C. Reichel, H. Steinkemper, M. Herm, and S. W. Glunz, "Tunnel oxide passivated contacts as an alternative to partial rear contacts," *Solar Energy Materials and Solar Cells*, vol. 131, pp. 46–50, 2014.
- [13] A. Moldovan, F. Feldmann, K. Kaufmann, S. Richter, M. Wemer, C. Hagedorf, M. Zimmer, L. Rentsch, and M. Hermle, "Tunnel oxide passivated carrier-selective contacts based on ultra-thin SiO_2 layers grown by photo-oxidation or wet-chemical oxidation in ozonized water," IEEE Photovoltaic Specialists Conference, (New Orleans, LA), IEEE, 2015.
- [14] Q. Li, K. Tao, Y. Sun, R. Jia, S.-M. Wang, Z. Jin, and X.-Y. Liu, "Replacing the amorphous silicon thin layer with microcrystalline silicon thin layer in topcon solar cells," *Solar Energy*, vol. 135, pp. 487–492, 2016.
- [15] J. Poortmans, *Thin film solar cells : fabrication, characterization and applications*, book section Preface, pp. xvii–xxix. Chichester, WS: Wiley, 2006.
- [16] C. Ballif and A. Shah, *Thin-film silicon solar cells*. Engineering sciences. Micro- and nanotechnology, Lausanne: EFPL Press, 2010.
- [17] A. Shah, *Basic Properties of Hydrogenated Amorphous Silicon (a-Si:H)*, book section 2, pp. 17–96. Engineering sciences. Micro- and nanotechnology, Lausanne: EFPL Press, 2010.
- [18] F. Köhler, *Zur Mikrostruktur siliziumbasierter Dünnschichten für die Photovoltaik*. Schriften des Forschungszentrums Jülich. Reihe Energie und Umwelt, Jülich: Forschungszentrum Jülich, 2013.
- [19] S. Muthmann, F. Köhler, R. Carius, and A. Gordijn, "Structural order on different length scales in amorphous silicon investigated by raman spectroscopy," *physica status solidi (a)*, vol. 207, no. 3, pp. 544–547, 2010.
- [20] E. Vallat-Sauvain, A. Shah, and J. Bailat, *Thin film solar cells : fabrication, characterization and applications*, book section Advances in Microcrystalline Silicon Solar Cell Technologies, pp. 133–171. Chichester, WS: Wiley, 2006.
- [21] M. Zeman and R. E. I. Schropp, *Amorphous and Microcrystalline Silicon Solar Cells: Modeling, Materials and Device Technology*. Boston, Mass.: Kluwer Academic Publ., 1998.
- [22] "Best research-cell efficiencies." National Renewable Energy Laboratory (NREL) <https://www.nrel.gov/pv/assets/images/efficiency-chart.png>, Apr. 2017.

-
- [23] Y. Kuo, *Thin Film Transistors: Amorphous silicon thin film transistors*. Kluwer Academic Publishers, 2004.
- [24] M. Zeman, *Thin film solar cells : fabrication, characterization and applications*, book section Advanced Amorphous Silicon Solar Cell Technologies, pp. 173–236. Chichester, WS: Wiley, 2006. editor Poortmans, Jef.
- [25] M. Zeman and R. E. I. Schropp, *Amorphous and Microcrystalline Silicon Solar Cells: Modeling, Materials and Device Technology [E-Book]*, vol. 5 of *Electronic Materials: Science & Technology* ;. Boston, MA: Springer, 1998.
- [26] T. Kirchartz, D. Abou-Ras, and U. Rau, *Introduction to Thin-Film Photovoltaics*, vol. 1, book section 1, pp. 3–40. Weinheim: Wiley-VCH Verlag, second, extended edition ed., 2016.
- [27] S. Q. Hussain, S. Kim, S. Ahn, H. Park, A. H. T. Le, S. Lee, Y. Lee, J. H. Lee, and J. Yi, “Rf magnetron sputtered ito:zr thin films for the high efficiency a-si:h/c-si heterojunction solar cells,” *Metals and Materials International*, vol. 20, no. 3, pp. 565–569, 2014.
- [28] Q. Wang, M. Page, Y. M. Ai, W. Nemeth, L. Roybal, H. C. Yuan, and Ieee, *Hydrogenated Amorphous Si Deposition for High Efficiency a-Si/c-Si Heterojunction Solar Cells*, pp. 188–190. IEEE Photovoltaic Specialists Conference, Photovoltaic Specialists Conference (PVSC), 2013 IEEE 39th, 2013.
- [29] D. Munoz, F. Ozanne, T. Salvetat, N. Enjalbert, G. Fortin, E. Pihan, F. Jay, A. Jouini, P. J. Ribeyron, and Ieee, *Strategies of cost reduction and high performance on a-Si:H/c-Si heterojunction solar cells: 21% efficiency on monolike substrate*, pp. 3071–3073. IEEE Photovoltaic Specialists Conference, Photovoltaic Specialists Conference (PVSC), 2013 IEEE 39th, 2013.
- [30] A. Danel, F. Souche, T. Nolan, Y. Le Tiec, and P. J. Ribeyron, “Hf last passivation for high efficiency a-si/c-si heterojunction solar cells,” in *Ultra Clean Processing of Semiconductor Surfaces X* (P. Mertens, M. Meuris, and M. Heyns, eds.), vol. 187 of *Solid State Phenomena*, pp. 345–348, Solid State Phenomena, 2012.
- [31] A. Chen and K. G. Zhu, “Computer simulation of a-si/c-si heterojunction solar cell with high conversion efficiency,” *Solar Energy*, vol. 86, no. 1, pp. 393–397, 2012.
- [32] T. Sawada, N. Terada, S. Tsuge, T. Baba, T. Takahama, K. Wakisaka, S. Tsuda, S. Nakano, and Ieee, “High-efficiency a-si/c-si heterojunction

- solar cell,” in *1994 IEEE First World Conference on Photovoltaic Energy Conversion/Conference Record of the Twenty Fourth IEEE Photovoltaic Specialists Conference-1994, Vols I and II*, Ieee Photovoltaic Specialists Conference, pp. 1219–1226, 1994.
- [33] D. Lachenal, D. Baetzner, W. Frammelsberger, B. Legradic, J. Meixenberger, P. Papet, B. Strahm, and G. Wahli, “Heterojunction and passivated contacts: A simple method to extract both n/tco and p/tco contacts resistivity,” *Energy Procedia*, vol. 92, pp. 932–938, 2016.
- [34] F. Feldmann, C. Reichel, R. Muller, and M. Hermle, “The application of poly-si/siox contacts as passivated top/rear contacts in si solar,” *Solar Energy Materials and Solar Cells*, vol. 159, pp. 265–271, 2017.
- [35] T. Matsushita, N. Oh-uchi, H. Hayashi, and H. Yamoto, “A silicon heterojunction transistor,” *Applied Physics Letters*, vol. 35, no. 7, pp. 549–550, 1979.
- [36] P. Mei, J. B. Boyce, M. Hack, R. A. Lujan, R. I. Johnson, G. B. Anderson, D. K. Fork, and S. E. Ready, “Laser dehydrogenation/crystallization of plasma-enhanced chemical vapor deposited amorphous silicon for hybrid thin film transistors,” *Applied Physics Letters*, vol. 64, no. 9, pp. 1132–1134, 1994.
- [37] T. Sameshima, “Status of si thin film transistors,” *Journal of Non-Crystalline Solids*, vol. 227-230, no. Part 2, pp. 1196–1201, 1998.
- [38] R. E. I. Schropp, B. Stannowski, and J. K. Rath, “New challenges in thin film transistor (tft) research,” *Journal of Non-Crystalline Solids*, vol. 299-302, no. Part 2, pp. 1304–1310, 2002.
- [39] K. Wilken, V. Smirnov, O. Astakhov, and F. Finger, “Thin-film silicon solar cells fabricated at low temperature: A versatile technology for application on transparent flexible plastic substrates and in integrated photoelectrochemical water splitting modules,” *2014 Ieee 40th Photovoltaic Specialist Conference (Pvsc)*, pp. 3051–3054, 2014.
- [40] F. Urbain, K. Wilken, V. Smirnov, O. Astakhov, A. Lambertz, J.-P. Becker, U. Rau, J. Ziegler, B. Kaiser, W. Jaegermann, and F. Finger, “Development of thin film amorphous silicon tandem junction based photocathodes providing high open-circuit voltages for hydrogen production,” *International Journal of Photoenergy*, vol. 2014, p. 10, 2014.

- [41] J. P. Becker, F. Urbain, V. Smirnov, U. Rau, J. Ziegler, B. Kaiser, W. Jaegermann, and F. Finger, "Modeling and practical realization of thin film silicon-based integrated solar water splitting devices," *Physica Status Solidi a-Applications and Materials Science*, vol. 213, no. 7, pp. 1738–1746, 2016.
- [42] B. Turan, J. P. Becker, F. Urbain, F. Finger, U. Rau, and S. Haas, "Upscaling of integrated photoelectrochemical water-splitting devices to large areas," *Nature Communications*, vol. 7, p. 9, 2016.
- [43] J. Haschke, D. Amkreutz, L. Korte, F. Ruske, and B. Rech, "Towards wafer quality crystalline silicon thin-film solar cells on glass," *Solar Energy Materials and Solar Cells*, vol. 128, pp. 190–197, 2014.
- [44] S. Varlamov, J. Dore, R. Evans, D. Ong, B. Eggleston, O. Kunz, U. Schubert, T. Young, J. Huang, T. Soderstrom, K. Omaki, K. Kim, A. Teal, M. Jung, J. Yun, Z. M. Pakhuruddin, R. Egan, and M. A. Green, "Polycrystalline silicon on glass thin-film solar cells: A transition from solid-phase to liquid-phase crystallization," *Solar Energy Materials and Solar Cells*, vol. 119, pp. 246–255, 2013.
- [45] D. Amkreutz, J. Haschke, S. Kuhnappel, P. Sonntag, and B. Rech, "Silicon thin-film solar cells on glass with open-circuit voltages above 620 mV formed by liquid-phase crystallization," *IEEE Journal of Photovoltaics*, vol. 4, no. 6, pp. 1496–1501, 2014.
- [46] J. Dore, D. Ong, S. Varlamov, R. Egan, and M. A. Green, "Progress in laser-crystallized thin-film polycrystalline silicon solar cells: Intermediate layers, light trapping, and metallization," *IEEE Journal of Photovoltaics*, vol. 4, no. 1, pp. 33–39, 2014.
- [47] O. Gabriel, T. Frijnts, S. Calnan, S. Ring, S. Kirner, A. Opitz, I. Rotherth, H. Rhein, M. Zelt, K. Bhatti, J. H. Zollondz, A. Heidelberg, J. Haschke, D. Amkreutz, S. Gall, F. Friedrich, B. Stannowski, B. Rech, and R. Schlattmann, "Pecvd intermediate and absorber layers applied in liquid-phase crystallized silicon solar cells on glass substrates," *Photovoltaics, IEEE Journal of*, vol. 4, no. 6, pp. 1343–1348, 2014.
- [48] S. Kuhnappel, S. Gall, B. Rech, and D. Amkreutz, "Towards monocrystalline silicon thin films grown on glass by liquid phase crystallization," *Solar Energy Materials and Solar Cells*, vol. 140, pp. 86–91, 2015.

- [49] B. E. Pieters, H. Stiebig, M. Zeman, and R. A. C. M. M. van Swaaij, "Determination of the mobility gap of intrinsic $\mu\text{-c-si:h}$ in p-i-n solar cells," *Journal of Applied Physics*, vol. 105, no. 4, p. 044502, 2009.
- [50] J. Kakalios, "Hydrogen diffusion in amorphous silicon," in *Hydrogen in Semiconductors*, vol. 34, pp. 381–425, Semiconductor and Semimetals, 1991.
- [51] D. L. Staebler and C. R. Wronski, "Reversible conductivity changes in discharge-produced amorphous si," *Applied Physics Letters*, vol. 31, no. 4, pp. 292–294, 1977.
- [52] R. A. Street, *Amorphous silicon device technology*, p. 363–403. Cambridge Solid State Science Series, Cambridge University Press, 1991.
- [53] M. H. Cohen, *Elements of the Theory of Amorphous Semiconductors*, vol. 136, book section 1, pp. 1–14. New-York, NY: Plenum Press, 1986.
- [54] R. Carius, F. Finger, U. Backhausen, M. Luysberg, P. Hapke, L. Houben, M. Otte, and H. Overhof, "Electronic properties of microcrystalline silicon," in *Amorphous and Microcrystalline Silicon Technology - 1997*, vol. 467 of *Materials Research Society Symposium Proceedings*, pp. 283–294, 1997. editors Wagner, S. and Hack, M. and Schiff, and Schropp, R.E.I. and Shimizu, I.
- [55] M. Zeman and R. E. I. Schropp, *Metastability*, book section 5, pp. 99–112. Boston, Mass.: Kluwer Academic Publ., 1998.
- [56] M. Stutzmann, W. B. Jackson, and C. C. Tsai, "Annealing of metastable defects in hydrogenated amorphous silicon," *Phys. Rev. B*, vol. 34, pp. 63–72, Jul 1986.
- [57] H. Wagner and W. Beyer, "Reinterpretation of the silicon-hydrogen stretch frequencies in amorphous silicon," *Solid State Communications*, vol. 48, no. 7, pp. 585–587, 1983.
- [58] S. Koc, M. Závětová, and J. Zemek, "Physical properties of amorphous si:h the role of annealing," *Czechoslovak Journal of Physics B*, vol. 25, no. 1, pp. 83–90, 1975.
- [59] N. Serin, "The determination of thermal annealing effect on a-si:h films coated on glass and on single crystalline of silicon," *Turk J Phys*, vol. 26, pp. 53–59, 2002.
- [60] N. A. Blum and C. Feldman, "The crystallization of amorphous silicon films," *Journal of Non-Crystalline Solids*, vol. 11, no. 3, pp. 242–246, 1972.

-
- [61] W. Beyer, "Diffusion and evolution of hydrogen in hydrogenated amorphous and microcrystalline silicon," *Solar Energy Materials and Solar Cells*, vol. 78, no. 1–4, pp. 235–267, 2003.
- [62] W. Beyer and H. Wagner, "The role of hydrogen in a-si:h - results of evolution and annealing studies," *Journal of Non-Crystalline Solids*, vol. 59-6, no. DEC, pp. 161–168, 1983.
- [63] M. Stutzmann, "The defect density in amorphous silicon," *Philosophical Magazine B*, vol. 60, no. 4, pp. 531–546, 1989.
- [64] D. Roy, C. Longeaud, and O. Saadane, "Influence of light-soaking and annealing on the microstructure of a-si:h deposited at 423 k," *Journal of Non-Crystalline Solids*, vol. 299-302, no. Part 1, pp. 511–515, 2002.
- [65] G. N. Parsons, C. Wang, M. J. Williams, and G. Lucovsky, "Post-deposition relaxation of electronic defects in hydrogenated amorphous silicon," *Applied Physics Letters*, vol. 56, no. 19, pp. 1895–1897, 1990.
- [66] T. Seth, P. N. Dixit, C. Mukherjee, C. Anandan, and R. Bhattacharyya, "Hydrogenated amorphous silicon films prepared at low substrate temperature on a cathode of an asymmetric r.f. plasma cvd system," *Thin Solid Films*, vol. 264, no. 1, pp. 11–17, 1995.
- [67] N. Hata and A. Matsuda, "Difference in light-induced annealing behavior of deposition- and light-induced defects in hydrogenated amorphous silicon," *Applied Physics Letters*, vol. 63, no. 14, pp. 1948–1950, 1993.
- [68] J. P. Conde, K. K. Chan, J. M. Blum, M. Arienzo, P. A. Monteiro, J. A. Ferreira, V. Chu, and N. Wyrsh, "Annealing kinetics of a-si:h deposited by concentric-electrode rf glow discharge at room temperature," *Journal of Applied Physics*, vol. 73, no. 4, pp. 1826–1831, 1993.
- [69] C. Koch, *Niedertemperaturabscheidung von Dünnschicht-Silicium für Solarzellen auf Kunststoffolien*. Thesis, Universität Stuttgart, 2003.
- [70] O. S. Panwar, C. Mukherjee, and R. Bhattacharyya, "Effect of annealing on the electrical, optical and structural properties of hydrogenated amorphous silicon films deposited in an asymmetric r.f. plasma cvd system at room temperature," *Solar Energy Materials and Solar Cells*, vol. 57, no. 4, pp. 373–391, 1999.
- [71] F. Finger, *Thin-film silicon solar cells*, pp. 97–143. Lausanne: EFPL Press, 2010. editors Shah, Arvind.

- [72] M. Kondo and A. Matsuda, *Low-Temperature Fabrication of Nanocrystalline-Silicon Solar Cells*, book section Thin-Film Solar Cells, pp. 139–149. Berlin, Heidelberg: Springer Berlin Heidelberg, 2004. editors Hamakawa, Yoshihiro.
- [73] C. Droz, E. Vallat-Sauvain, J. Bailat, L. Feitknecht, J. Meier, X. Niquille, and A. Shah, *Electrical and microstructural characterisation of microcrystalline silicon layers and solar cells*. Proceedings of 3rd World Conference on Photovoltaic Energy Conversion, Vols a-C, Proceedings of 3rd World Conference on Photovoltaic Energy Conversion, 2003.
- [74] O. Vetterl, F. Finger, R. Carius, P. Hapke, L. Houben, O. Kluth, A. Lambertz, A. Muck, B. Rech, and H. Wagner, “Intrinsic microcrystalline silicon: A new material for photovoltaics,” *Solar Energy Materials and Solar Cells*, vol. 62, no. 1-2, pp. 97–108, 2000.
- [75] W. Beyer, *Hydrogen in Semiconductors II*, vol. Volume 61, book section Chapter 5 - Hydrogen Phenomena in Hydrogenated Amorphous Silicon, pp. 165–239. Elsevier, 1999. editor Norbert, H. Nickel.
- [76] M. van den Donker, T. Kilper, D. Grunsky, B. Rech, L. Houben, W. Kessels, and M. van de Sanden, “Microcrystalline silicon deposition: Process stability and process control,” *Thin Solid Films*, vol. 515, no. 19, pp. 7455 – 7459, 2007. Proceedings of Symposium I on Thin Films for Large Area Electronics EMRS 2007 Conference.
- [77] O. Vetterl, A. Gross, T. Jana, S. Ray, A. Lambertz, R. Carius, and F. Finger, “Changes in electric and optical properties of intrinsic microcrystalline silicon upon variation of the structural composition,” *Journal of Non-Crystalline Solids*, vol. 299, pp. 772–777, 2002.
- [78] J. Müller, F. Finger, R. Carius, and H. Wagner, “Electron spin resonance investigation of electronic states in hydrogenated microcrystalline silicon,” *Phys. Rev. B*, vol. 60, pp. 11666–11677, Oct 1999.
- [79] Panasonic, “Panasonic HIT© solar cell achieves world’s highest energy conversion efficiency of 25.6% at research level.” <http://news.panasonic.com/global/press/data/2014/04/en140410-4/en140410-4.html>, 2014.
- [80] I. R. C. Post, P. Ashburn, and G. R. Wolstenholme, “Polysilicon emitters for bipolar transistors: a review and re-evaluation of theory and experiment,” *IEEE Transactions on Electron Devices*, vol. 39, no. 7, pp. 1717–1731, 1992.

-
- [81] S. Haas, G. Schöpe, C. Zahren, and H. Stiebig, “Analysis of the laser ablation processes for thin-film silicon solar cells,” *Applied Physics a-Materials Science & Processing*, vol. 92, no. 4, pp. 755–759, 2008.
- [82] S. Haas, S. Krumscheid, A. Bauer, A. Lambertz, and U. Rau, “Novel series connection concept for thin film solar modules,” *Progress in Photovoltaics*, vol. 21, no. 5, pp. 972–979, 2013.
- [83] S. Ku, S. Haas, B. E. Pieters, U. Zastrow, A. Besmehn, Q. Ye, and U. Rau, “Investigation of laser scribing of a-si:h from the film side for solar modules using a uv laser with ns pulses,” *Applied Physics a-Materials Science & Processing*, vol. 105, no. 2, pp. 355–362, 2011.
- [84] S. Haas, A. Gordijn, and H. Stiebig, “High speed laser processing for monolithic series connection of silicon thin-film modules,” *Progress in Photovoltaics*, vol. 16, no. 3, pp. 195–203, 2008.
- [85] B. Turan, A. Bauer, A. Lambertz, T. Merdzhanova, and S. Haas, “Novel interconnection scheme for thin-film silicon solar modules with conductive intermediate reflector,” *Physica Status Solidi-Rapid Research Letters*, vol. 9, no. 2, pp. 103–107, 2015.
- [86] B. Turan, S. Haas, and M. Steger, “Optimization of front-contact laser scribing for thin-film silicon solar modules,” *Solar Energy Materials and Solar Cells*, vol. 125, pp. 78–86, 2014.
- [87] EdgeWave. <http://www.edge-wave.de/web/>, 2017.
- [88] M. Gebhardt, T. Kießling, and M. Grimm, “Laser contact opening of high efficient solar cells,” *Laser Technik Journal*, vol. 11, no. 1, pp. 18–20, 2014.
- [89] S. Kühnappel, N. H. Nickel, S. Gall, M. Klaus, C. Genzel, B. Rech, and D. Amkreutz, “Preferential 100 grain orientation in 10 micrometer-thick laser crystallized multicrystalline silicon on glass,” *Thin Solid Films*, vol. 576, pp. 68–74, 2015.
- [90] S. Helfert, “Numerical methods in frequency domain: part I.” Fernuniversität Hagen, Nanooptics, 2011.
- [91] Comsol, “The finite element method (FEM).” Webpage, 2017.
- [92] J. Ruokolainen, M. Malinen, P. Råback, T. Zwinger, A. Pursula, and M. Byckling, “Elmersolver manual,” documentation, CSC – IT Center for Science, 2014. Ruokolainen, Juha Malinen, Mika Råback , Peter Zwinger, Thomas Pursula, Antti and Byckling, Mikko.

- [93] J.-F. R. Christophe Geuzaine, “Gmsh: a three-dimensional finite element mesh generator with built-in pre- and post-processing facilities,” *International Journal for Numerical Methods in Engineering*, vol. 79, pp. 1309–1331, May 2009.
- [94] Corning™, “Eagle XG™ slim glass product information sheet,” tech. rep., Corning™, 2013.
- [95] H. C. Webber, A. G. Cullis, and N. G. Chew, “Computer simulation of high speed melting of amorphous silicon,” *Applied Physics Letters*, vol. 43, no. 7, pp. 669–671, 1983.
- [96] S. Bédard and L. J. Lewis, “Diffusion of hydrogen in crystalline silicon,” *Physical Review B*, vol. 61, no. 15, pp. 9895–9898, 2000.
- [97] B. Tuttle, “Energetics and diffusion of hydrogen in SiO_2 ,” *Physical Review B*, vol. 61, pp. 4417–4420, Feb. 2000.
- [98] Abu-Ras, *Advanced characterization techniques for thin film solar cells*. Weinheim: Wiley-VCH Verlag, second, extended edition ed., 2016.
- [99] T. Itoh, K. Yamamoto, K. Ushikoshi, S. Nonomura, and S. Nitta, “Characterization and role of hydrogen in nc-si : H,” *Journal of Non-Crystalline Solids*, vol. 266, pp. 201–205, 2000.
- [100] L. B. und Clemens Schaefer, *Optik*, vol. Band 3 of *Lehrbuch der Experimentalphysik*. Berlin: DeGruyter, 9. auflage ed., 1993.
- [101] F. Einsele, T. Bronger, A. Gerber, T. Kirchartz, K. Ding, K. Bittkau, S. Lehnen, W. Beyer, V. Huhn, T. C. M. Müller, U. Rau, U. W. Paetzold, D. Abou-Ras, and B. E. Pieters, *Advanced characterization techniques for thin film solar cells*, vol. 2. Weinheim: Wiley-VCH Verlag, second, extended edition ed., 2016.
- [102] A. H. Mahan, P. Raboisson, D. L. Williamson, and R. Tsu, “Evidence for microstructure in glow-discharge hydrogenated amorphous SiC alloys,” *Solar Cells*, vol. 21, pp. 117–126, 1987.
- [103] A. Shih, S.-C. Lee, and C.-t. Chia, “Evidence for coupling of Si-Si lattice vibration and Si-D wagging vibration in deuterated amorphous silicon,” *Applied Physics Letters*, vol. 74, no. 22, pp. 3347–3349, 1999.
- [104] R. Wächter, *Ramanspektroskopie an hydrogenierten und deuterierten amorphen Siliziumschichten*. Berichte des Forschungszentrums Jülich, Forschungszentrum Jülich, 1994.

-
- [105] N. Budini, P. Rinaldi, J. Schmidt, R. Arce, and R. Buitrago, "Influence of microstructure and hydrogen concentration on amorphous silicon crystallization," *Thin Solid Films*, vol. 518, pp. 5349–5354, Apr. 2010.
- [106] V. P. Tolstoy, I. V. Chernyshova, and V. A. Skryshevsky, *Handbook of Infrared Spectroscopy of Ultrathin Films*. Wiley, 2003.
- [107] M. H. Brodsky, M. Cardona, and J. J. Cuomo, "Infrared and raman-spectra of silicon-hydrogen bonds in amorphous silicon prepared by glow-discharge and sputtering," *Physical Review B*, vol. 16, no. 8, pp. 3556–3571, 1977.
- [108] T. Trupke, R. A. Bardos, M. C. Schubert, and W. Warta, "Photoluminescence imaging of silicon wafers," *Applied Physics Letters*, vol. 89, no. 4, p. 044107, 2006.
- [109] H. C. Sio, S. P. Phang, T. Trupke, and D. Macdonald, "An accurate method for calibrating photoluminescence-based lifetime images on multi-crystalline silicon wafers," *Solar Energy Materials and Solar Cells*, vol. 131, pp. 77–84, 2014.
- [110] A. Cuevas and D. Macdonald, "Measuring and interpreting the lifetime of silicon wafers," *Solar Energy*, vol. 76, no. 1, pp. 255 – 262, 2004. Solar World Congress 2001.
- [111] K. Ramspeck, S. Reissenweber, J. Schmidt, K. Bothe, and R. Brendel, "Dynamic carrier lifetime imaging of silicon wafers using an infrared-camera-based approach," *Applied Physics Letters*, vol. 93, no. 10, p. 3, 2008.
- [112] K. Ramspeck, K. Bothe, J. Schmidt, and R. Brendel, "Combined dynamic and steady-state infrared camera based carrier lifetime imaging of silicon wafers," *Journal of Applied Physics*, vol. 106, no. 11, p. 10, 2009.
- [113] EdgeWave, "Laser power sheet." EdgeWave GmbH, 2014.
- [114] EdgeWave, "Laser beam profile datasheet SN0287." EdgeWave GmbH, 2013-11-29 2013.
- [115] K. Mertens, *Photovoltaik : Lehrbuch zu Grundlagen, Technologie und Praxis*. München: Fachbuchverl. Leipzig, 3., neu bearb. u. erw. Aufl. ed., 2015.
- [116] W. Beyer, W. Hilgers, D. Lennartz, F. Maier, N. Nickel, F. Pennartz, and P. Prunici, "Effect of annealing on microstructure in (doped and undoped) hydrogenated amorphous silicon films," *MRS Online Proceedings Library Archive*, vol. 1666, 2014.

- [117] V. P. Tolstoy, I. V. Chernyshova, and V. A. Skryshevsky, *Equipment and Techniques*, pp. 307–415. John Wiley and Sons, Inc., 2003.
- [118] V. A. Volodin and D. I. Koshelev, “Quantitative analysis of hydrogen in amorphous silicon using raman scattering spectroscopy,” *Journal of Raman Spectroscopy*, vol. 44, no. 12, pp. 1760–1764, 2013.
- [119] M. Ivanda, “Raman-scattering measurements and fraction interpretation of vibrational properties of amorphous silicon,” *Physical Review B*, vol. 46, no. 22, pp. 14893–14896, 1992.
- [120] M. Ivanda, O. Gamulin, K. Furić, and D. Gracin, “Raman study of light-induced changes in silicon-hydrogen bond stretching vibration in a-si:h,” *Journal of Molecular Structure*, vol. 267, pp. 275–280, 1992.
- [121] K. O. Bugaev, A. A. Zelenina, and V. A. Volodin, “Vibrational spectroscopy of chemical species in silicon and silicon-rich nitride thin films,” *International Journal of Spectroscopy*, vol. 2012, pp. 1–5, 2012.
- [122] P. V. Santos, N. M. Johnson, and R. A. Street, “Light-enhanced hydrogen motion in a-si:h,” *Physical Review Letters*, vol. 67, no. 19, pp. 2686–2689, 1991.
- [123] A. A. Langford, M. L. Fleet, B. P. Nelson, W. A. Lanford, and N. Mailey, “Infrared-absorption strength and hydrogen content of hydrogenated amorphous-silicon,” *Physical Review B*, vol. 45, no. 23, pp. 13367–13377, 1992.
- [124] S. Yamasaki, T. Umeda, J. Isoya, and K. Tanaka, “Existence of surface region with high dangling bond density during a-si : H film growth,” *Journal of Non-Crystalline Solids*, vol. 227, pp. 83–87, 1998.
- [125] T. F. Young, C. P. Chen, J. F. Liou, Y. L. Yang, and T. C. Chang, “Study on the si-si vibrational states of the near surface region of porous silicon,” *Journal of Porous Materials*, vol. 7, pp. 339–343, Jan. 2000.
- [126] S. Al Dallal, “Spectroscopic and optoelectronic properties of hydrogenated amorphous silicon-chalcogen alloys, superalloys,” *InTech*, 2015.
- [127] S.-Y. Lin, “Vibrational stretching modes of the si-h and si-d bonds in amorphous silicon nitride,” *MRS Proceedings*, vol. 664, 2011.
- [128] D. Tuschel, “Headspace raman spectroscopy,” *Spectroscopy*, vol. 29, Sep 01, 2014 2014.

-
- [129] N. Liao, W. Li, Y. Kuang, Y. Jiang, S. Li, Z. Wu, and K. Qi, "Raman and ellipsometric characterization of hydrogenated amorphous silicon thin films," *Science in China Series E: Technological Sciences*, vol. 52, no. 2, pp. 339–343, 2009.
- [130] W. Beyer, U. Breuer, R. Carius, W. Hilgers, D. Lennartz, F. C. Maier, N. H. Nickel, F. Pennartz, P. Prunici, and U. Zastrow, "Influence of hydrogen concentration on void-related microstructure in low hydrogen amorphous and crystalline silicon materials," *Canadian Journal of Physics*, vol. 92, no. 7-8, pp. 700–704, 2014.
- [131] W. Beyer and H. Wagner, "Determinataion of the hydrogen diffusion coefficient in hydrogenated amorphous silicon from hydrogen effusion experiments," *Journal of Applied Physics*, vol. 53, no. 12, pp. 8745–8750, 1982.
- [132] R. A. Street, C. C. Tsai, J. Kakalios, and W. B. Jackson, "Hydrogen diffusion in amorphous silicon," *Philosophical Magazine Part B*, vol. 56, no. 3, pp. 305–320, 1987.
- [133] M. Reinelt, S. Kalbitzer, and G. Moller, "Proceedings of the tenth international conference on amorphous and liquid semiconductors the diffusion of hydrogen in amorphous silicon," *Journal of Non-Crystalline Solids*, vol. 59, pp. 169–172, 1983.
- [134] T. C. M. Müller and T. Kirchartz, *Absorption and Photocurrent Spectroscopy with High Dynamic Range*, vol. 1, book section 8, pp. 191–214. Weinheim: Wiley-VCH Verlag, second, extended edition ed., 2016.
- [135] P. Mei, J. B. Boyce, M. Hack, R. A. Lujan, R. I. Johnson, G. B. Anderson, D. K. Fork, S. E. Ready, and D. L. Smith, "Laser dehydrogenation of pecvd amorphous silicon," *MRS Proceedings*, vol. 297, 1993.
- [136] W. Beyer, J. Bergmann, U. Breuer, F. Finger, A. Lambertz, T. Merdzhanova, N. Nickel, F. Pennartz, T. Schmidt, and U. Zastrow, "Comparison of laser and oven annealing effects on hydrogen and microstructure in thin film silicon," *MRS Online Proceedings Library Archive*, vol. 1770, pp. 1–6, 2015.
- [137] F. Gontad, J. C. Conde, S. Filonovich, M. F. Cerqueira, P. Alpuim, and S. Chiussi, "Study on excimer laser irradiation for controlled dehydrogenation and crystallization of boron doped hydrogenated amorphous/nanocrystalline silicon multilayers," *Thin Solid Films*, vol. 536, pp. 147–151, 2013.

- [138] N. H. Nickel, W. B. Jackson, and N. M. Johnson, "Light-induced creation of metastable paramagnetic defects in hydrogenated polycrystalline silicon," *Physical Review Letters*, vol. 71, no. 17, pp. 2733–2736, 1993.
- [139] M. Stutzmann, J. Nunnenkamp, M. S. Brandt, A. Asano, and M. C. Rossi, "Accelerated metastable defect creation in a-si-h by short light-pulses," *Journal of Non-Crystalline Solids*, vol. 137, pp. 231–234, 1991.
- [140] H. M. Branz, "Hydrogen collision model of the staebler-wronski effect: Microscopics and kinetics," *MRS Proceedings*, vol. 507, 2011.
- [141] F. Kail, S. Fellah, A. Abramov, A. Hadjadj, and P. Roca i Cabarrocas, "Experimental evidence for extended hydrogen diffusion in silicon thin films during light-soaking," *Journal of Non-Crystalline Solids*, vol. 352, no. 9, pp. 1083–1086, 2006.
- [142] M. Stutzmann, M. C. Rossi, and M. S. Brandt, "Pulsed-light soaking of hydrogenated amorphous silicon," *Physical Review B*, vol. 50, no. 16, pp. 11592–11605, 1994.
- [143] M. Yamaguchi and K. Morigaki, "Effect of hydrogen dilution on the optical properties of hydrogenated amorphous silicon prepared by plasma deposition," *Philosophical Magazine Part B*, vol. 79, no. 3, pp. 387–405, 1999.
- [144] R. Z. Bachrach, K. Winer, J. B. Boyce, S. E. Ready, R. I. Johnson, and G. B. Anderson, "Low temperature crystallization of amorphous silicon using an excimer laser," *Journal of Electronic Materials*, vol. 19, no. 3, pp. 241–248, 1990.
- [145] K. Winer, G. B. Anderson, S. E. Ready, R. Z. Bachrach, R. I. Johnson, F. A. Ponce, and J. B. Boyce, "Excimer-laser-induced crystallization of hydrogenated amorphous silicon," *Applied Physics Letters*, vol. 57, no. 21, pp. 2222–2224, 1990.
- [146] K. Prasad, F. Finger, S. Dubail, A. Shah, and M. Schubert, "Deposition of phosphorus doped microcrystalline silicon below 70 ° c at 70 mhz," *Journal of Non-Crystalline Solids*, vol. 137, pp. 681–684, 1991.
- [147] F. Finger, K. Prasad, S. Dubail, A. Shah, X. M. Tang, J. Weber, and W. Beyer, *Influence of Doping on the Structural Properties of Microcrystalline Silicon Prepared with the VHF-GD Technique at Low Deposition Temperatures*, vol. 219 of *Amorphous Silicon Technology - 1991*. Pittsburgh: Materials Research Soc, 1991.

- [148] F. Cristiano, M. Shayesteh, R. Duffy, K. Huet, F. Mazzamuto, Y. Qiu, M. Quillec, H. H. Henrichsen, P. F. Nielsen, D. H. Petersen, A. La Magna, G. Caruso, and S. Boninelli, "Defect evolution and dopant activation in laser annealed si and ge," *Materials Science in Semiconductor Processing*, vol. 42, Part 2, pp. 188–195, 2016.
- [149] E. S. Machlin, *Chapter I - Electrical Properties*, pp. 1–56. Oxford: Elsevier Science Ltd, 2006.
- [150] H. Matsumura, Y. Tashiro, K. Sasaki, and S. Furukawa, "Hall-mobility of low-temperature-deposited polysilicon films by catalytic chemical-vapor-deposition method," *Japanese Journal of Applied Physics Part 2-Letters & Express Letters*, vol. 33, no. 9A, pp. L1209–L1211, 1994.
- [151] G. R. S. Iyer, E. K. Hobbie, S. Guruvenket, J. M. Hoey, K. J. Anderson, J. Lovaasen, C. Gette, D. L. Schulz, O. F. Swenson, A. Elangovan, and P. Boudjouk, "Solution-based synthesis of crystalline silicon from liquid silane through laser and chemical annealing," *ACS Applied Materials & Interfaces*, vol. 4, no. 5, pp. 2680–2685, 2012. PMID: 22545711.
- [152] A. C. Bedini, S. Muthmann, J. Allgaier, K. Bittkau, F. Finger, and R. Carius, "Liquid hydridosilane precursor prepared from cyclopentasilane via sonication at low temperatures without the action of light," *Ultrasonics Sonochemistry*, vol. 34, pp. 289 – 293, 2017.

List of Symbols

| | |
|--------------------|--|
| A | absorptance |
| α | absorption coefficient |
| α | polarisability |
| B | magnetic force |
| c | constant |
| C_{cal} | calibration factor |
| c_{D} | deuterium concentration |
| c_{H} | hydrogen concentration |
| d | thickness |
| D | distance |
| D | diffusion coefficient |
| D_0 | diffusion coefficient prefactor |
| D_s | spot diameter |
| Δ | phase shift |
| Δs | line displacement |
| ΔT | temperature difference, temperature increase |
| E_{A} | activation energy |
| E_{bond} | bonding energy |
| E_{C} | conductivity band mobility edge |
| E_{g} | mobility gap, bandgap, optical gap |
| E_{ph} | photon energy |
| E_{V} | valence band mobility edge |
| F | correction factor |
| f_{boltz} | Boltzmann fit function |
| f_{corr} | pyrometer correction factor |
| G | generation rate per unit volume |

| | |
|-------------------------|---|
| I | electrical current |
| I_{PL} | PL signal intensity |
| $I_{\text{PL, max}}$ | mean PL intensity in the area with the maximum lifetime |
| κ | thermal conductivity |
| λ | wavelength |
| L_{diff} | diffusion length |
| μ_{H} | Hall mobility |
| μ_{n} | (drift) mobility (n-type) |
| μ_{p} | (drift) mobility (p-type) |
| n | refractive index |
| n | carrier concentration |
| $N_{\text{A/D}}$ | background doping |
| ν | repetition rate |
| ν | wavenumber |
| ν_0 | excitation frequency |
| ν_{M} | Raman eigenfrequency |
| p | hole carrier concentration |
| P | power |
| P_{rf} | rf-power |
| p | pressure |
| P | Power, Laser Power |
| q | unit charge |
| R | reflectance |
| R | resistance |
| r_{s} | complex amplitude reflection coefficients perpendicular |
| r_{p} | complex amplitude reflection coefficients parallel |
| ρ | resistivity |
| ρ_{sh} | sheet resistivity |
| $R(\lambda)$ | spectral reflectance |
| R_{H} | Hall coefficient |
| r_{H} | Hall factor |
| R_{sh} | sheet resistance |
| σ_{dark} | dark conductivity |
| σ_{photo} | photoconductivity |

List of Symbols

| | |
|-------------------------|--|
| t | time |
| t_{int} | image acquisition time |
| T | temperature |
| T | transmittance |
| T_{corr} | calculated pyrometer temperature |
| T_{max} | maximum process temperature |
| T_{pyro} | pyrometer temperature |
| $T_{\text{pyro, meas}}$ | measured pyrometer temperature |
| T_{TE} | thermoelement temperature |
| $T(\lambda)$ | spectral transmittance |
| $\tan \psi$ | amplitude change upon reflection |
| τ_{eff} | effective minority carrier lifetime |
| $\tau_{\text{PL, max}}$ | mean lifetime in the area with the maximum lifetime |
| τ_{pulse} | pulse duration |
| τ_{SS} | local lifetime derived from steady state images |
| U_{bi} | built-in-voltage |
| v | velocity, scanning velocity, drift velocity |
| V_{H} | Hall voltage |
| w | width |
| w_x | beam width x-direction |
| w_y | beam width y-direction |
| X | sample specific factor |
| $X_{\text{as-dep}}$ | lifetime correction factors for as deposited PL intensity |
| X_{laser} | lifetime correction factors for laser treated PL intensity |
| X_{C} | Raman crystallinity |

List of Abbreviations

| | |
|---------|--|
| a-Si | amorphous silicon |
| a-Si:H | hydrogenated amorphous Silicon |
| BC | boundary condition |
| BMWi | Bundesministerium für Wirtschaft und Energie |
| c-Si | crystalline silicon |
| db | dangling bonds |
| DLR | Deutsches Luft- und Raumfahrtzentrum |
| DoS | density of states |
| FTIR | fourier transform infrared spectroscopy |
| FVEE | ForschungsVerbund Erneuerbare Energien |
| HiT | heterojunction solar cell with intrinsic thin-film |
| LRO | long range order |
| MRO | medium range order |
| μc-Si:H | microcrystalline silicon |
| PDS | photothermal deflection spectroscopy |
| PECVD | plasma enhanced chemical vapour deposition |
| SHJ | silicon heterojunction |
| SIMS | secondary ion mass spectrometry |
| SRO | short range order |
| SWE | Saebler-Wronski effect |
| TMB | Trimethylboron ($B(CH_3)_3$) |
| TOPCon | Tunnel Oxide Passivated Contact |

Acknowledgment

I would like to kindly thank those who helped and supported me during this work.

Prof. Dr. Uwe Rau for the opportunity to work at his institution and of course for all the fruitful discussions about my work, especially for the simulation part, and for "teaching me something for life" ("da lernen Sie jetzt noch was fürs Leben") when he gave me the clues how to make a perfect presentation.

Prof. Dr. Joachim Knoch for his willingness to review this thesis.

Dr. Stefan Haas for supervising this work and for being an encouraged group leader.

The colleagues from the laser group that contributed all to this work in one way or another.

Petra Lorbach for the organization of the IEK-5. Without her support, it would take all Ph.D students longer to finish their thesis and the institute would lack the one person who makes everything work out.

Dr. Yael Augarten, and Dr. Christopher Ball for the review of this thesis.

Dr. Bart Pieters for the small program that reduced my simulation time considerably, as well as for the review of the simulation part.

Daniel Weigand for the time that we have spend in the lab, working on setting up a laser system optimizing and automatizing. It is hard to find someone who is always in such good mood and motivated, even on long working days.

Markus Hülsbeck for the endless hours that he spend in the dark lab, supporting my Raman measurements on countless samples.

Dr. Wolfhard Beyer for all the discussions and lectures about the movement of hydrogen in amorphous silicon.

Sandra Moll for the instructions in various instruments I needed to use during my thesis.

Sabine Kasper, Oliver Thimm, Vito Huhn, Dr. Yael Augarten and Andrew Wrigley for the support during the last part of my thesis, the PL measurements as well as the corresponding furnace experiments.

Dr. Florian Maier for his supervision at the beginning of my thesis.

I would also like to thank those who gave me emotional support but left the institute before I did; especially Dr. Marzella Görig, Dr. Yael Augarten, and Manuela Meyer. And thank you again, Marzella and Manuela for the great experience of finishing a half-distance Ironman as a team.

I do also thank all the colleagues with whom I played soccer, those who went for a run with me during lunchtime, those who I could talk to when my thesis was troubling me, those who made me laugh and created such a pleasant working atmosphere in Jülich for me, and all colleagues that are not named here but contributed to my thesis in one way or another.

I would also like to thank the "L^AT_EX Stammtisch" in Aachen, who invited me to join their meetings. They helped me in solving issues with L^AT_EX and gave me helpful hints how to pimp the design of my thesis, in addition to nice company and discussions.

Alexandra Vent for the graphic design of my cover and the scientific illustrations for the presentation of my Ph.D. thesis of which I can kindly use two for the publication of my thesis (Figure 4.2 and Figure 4.5; www.scientific-illustrations.de).

Finally my special thanks goes to my husband Oliver Radtke, who never stops believing in me. He is always a great support for me, especially in troublesome times. Without him, I might not have had the courage to start a Ph.D. thesis.

Band / Volume 419

Tomographic reconstruction of gravity wave parameters from satellite-borne airglow observations

R. Song (2018), 136 pp

ISBN: 978-3-95806-317-4

Band / Volume 420

Reduktion von Edelmetallen in der Wasserstoffelektrode bei der Polymerelektrolyt-Wasserelektrolyse

P. Paciok (2018), VII, 187 pp

ISBN: 978-3-95806-320-4

Band / Volume 421

Mechanismen des Hochtemperaturrischwachstums in einem ferritischen Stahl an Luft und in Wasserdampf

T. Fischer (2018), VIII, 216 pp

ISBN: 978-3-95806-326-6

Band / Volume 422

Selbsteilende plasmagespritzte $Mn_{1,0}Co_{1,9}Fe_{0,1}O_4$ -Schutzschichten in Festoxidbrennstoffzellen

N. Grünwald (2018), x, 140 pp

ISBN: 978-3-95806-327-3

Band / Volume 423

Sonochemical Synthesis of Silicon Hydride Polymers and Silicon Nanoparticles from Liquid Silanes

A. P. Cádiz Bedini (2018), viii, 132, XVIII pp

ISBN: 978-3-95806-329-7

Band / Volume 424

Synthesis and Stability Assessment of Uranium Microparticles: Providing Reference Materials for Nuclear Verification Purposes

R. Middendorp (2018), X, 145 pp

ISBN: 978-3-95806-330-3

Band / Volume 425

Herstellung und Charakterisierung von Lithiumlanthanzirkonat-Funktionsschichten für Lithium-Festkörperbatterien

T. Reppert (2018), vii, 187 pp

ISBN: 978-3-95806-331-0

Band / Volume 426

Proton Conduction and Gas Permeation through Polymer Electrolyte Membranes during Water Electrolysis

M. Schalenbach (2018), VI, 212 pp

ISBN: 978-3-95806-333-4

Band / Volume 427

Improved characterization of root zone soil moisture by assimilating groundwater level and surface soil moisture data in an integrated terrestrial system model

H. Zhang (2018), x, 125 pp
ISBN: 978-3-95806-335-8

Band / Volume 428

Manipulation of magnetism in iron oxide nanoparticle / BaTiO₃ composites and low-dimensional iron oxide nanoparticle arrays

L. Wang (2018), VI, 151 pp
ISBN: 978-3-95806-338-9

Band / Volume 429

Characterization of spatial-temporal varying riverbed hydraulic conductivity and its role on the estimation of river-aquifer exchange fluxes with data assimilation

Q. Tang (2018), xv, 117 pp
ISBN: 978-3-95806-339-6

Band / Volume 430

Der Einfluss von Wasserdampf auf den Sauerstofftransport in keramischen Hochtemperaturmembranen

F. Thaler (2018), ii, 93, XXXI pp
ISBN: 978-3-95806-340-2

Band / Volume 431

Analysis & modeling of metastable photovoltaic technologies: towards dynamic photovoltaic performance models

M. Görig (2018), 246 pp
ISBN: 978-3-95806-342-6

Band / Volume 432

Laser Treatment of Silicon Thin-Films for Photovoltaic Applications

C. Maurer (2018), vii, 165 pp
ISBN: 978-3-95806-347-1

Weitere *Schriften des Verlags im Forschungszentrum Jülich* unter
<http://wwwzb1.fz-juelich.de/verlagextern1/index.asp>

Energie & Umwelt / Energy & Environment
Band / Volume 432
ISBN 978-3-95806-347-1

Mitglied der Helmholtz-Gemeinschaft

